DISSERTATION

Systematic study for discrete symmetry violation in neutron optics

(中性子光学を用いた離散的対称性の破れに対する系統的研究)

Nagoya University
Graduate School of Science
Laboratory for Particle Properties

462101049

Rintaro Nakabe

March 25th, 2024

Supervisor of Dissertation: Prof. Hirohiko M. Shimizu

概要

荷電共役 (C)、空間反転 (P)、そして時間反転 (T) 操作で構成される離散的対称性は物理学における基本的な対称性の一つであり、素粒子標準模型は中性 K 中間子崩壊に代表される離散的対称性の破れをその枠組みの中で説明することができる。一方、素粒子標準模型では説明の付かない観測事実が存在し、その一つに現在の宇宙におけるバリオン、反バリオン数の非対称性が挙げられる。この観測結果は標準模型を超える CP 対称性の破れを示唆している。CPT 定理より、CP 対称性の破れは時間反転対称性の破れと同等であるとみなせる。そのため時間反転操作に敏感な永久電気双極子モーメントの探索がさまざまな基本粒子とその複合系に対して６０年以上に渡り遂行されている。我々の研究グループは、永久電気双極子モーメント探索と非常に相補的となり得る、中性子スピンと原子核スピン間の時間反転対称性を破る相互作用の探索を計画している。低エネルギー中性子が誘起する原子核反応では、核子核子間相互作用における非常に小さな空間反転対称性の破れが s 波と p 波の混合によって生じる複合核状態を経由することで極めて大きく観測されている。この実験事実に基づき、時間反転対称性の破れが高感度に探索可能であることが予測されている。時間反転対称性の破れは空間反転対称性の破れと複合核スピンに依存する因子の積に比例するため、そのスピン依存因子を実験的に決定することは高感度探索の設計に向け重要である。スピン依存因子は p 波共鳴における中性子部分幅の角運動量比で定義されている混合角の決定により求めることができる。核種として p 波共鳴エネルギーが 0.75 eV であり、大きな空間反転対称性の破れが観測されている ^{139}La を選んだ。中性子と ^{139}La 標的核に対する零角度散乱振幅において、中性子スピンと核スピンの内積に比例する相関項は p 波共鳴において混合角を含む。そのため、測定には偏極中性子ビーム及び偏極核標的が必須である。大強度陽子加速器施設 J-PARC/BL22 において、中性子吸収断面積のスピン選択性を利用した ^{3}He スピンフィルターと、希釈冷凍機及び 7T 超伝導磁石による静的核偏極を同時にビームラインへと導入した。偏極中性子ビームを偏極核標的に照射し、中性子スピン正偏極、負偏極に対応する透過中性子数の非対称度を測定した。得られた非対称度に対して s 波共鳴由来の構造を差し引くことにより p 波共鳴の断面積を取得した。実験によって得られた断面積と理論式を比較することにより、混合角の解が４つ得られた。この解に対し、中性子吸収反応におけるガンマ線放出角度相関項測定による先行研究の結果が与える解の制限によって物理的な混合角の解を一意に決定し、スピン依存因子を求めた。孤立系複合核における零角度散乱振幅に得られた混合角を含め、中性子光学へ拡張して得られた中性子スピン観測量を計算することで、現実的な統計量において到達可能な時間反転対称性の破れに対する探索感度を見積もった。

Contents

List of Figures

List of Tables

Chapter 1

Introduction

Discrete symmetries, comprising of Charge conjugation (C), Parity (P), and Time-reversal (T) symmetries, have long been presumed to exist in the field of physics. However, in 1956, Lee and Yang theoretically proposed P violation (PV) in the weak interaction, and the following year, Wu et al. experimentally confirmed PV in the electron longitudinal polarization of β decay using $^{60}\mathrm{Co}$ [4, 5]. Subsequently, in 1964, CP violation through the decay of neutral K meson was first observed [6]. The exploration of the discrete symmetries violation has since become a widely researched field. All these phenomena and observed symmetry violations have been systematically explained by the Standard Model, which is considered a robust theoretical framework, exemplified by the discovery of the Higgs boson at the LHC [7]. However, there exist multiple observed results that remain unexplained by the Standard Model, suggesting phenomena beyond the Standard Model (BSM). One such instance is the baryon asymmetry in today's universe. Results from cosmological observations show a baryon-to-antibaryon asymmetry on the order of 10^9, which the Standard Model has not yet accounted for [8]. As proposed by Sakharov, the conditions for the universe to exhibit baryon asymmetry include baryon number violation, C and CP violation, and interactions out of thermal equilibrium [9]. There is a suggestion that the source of CP violation might be attributed to BSM physics.

1.1 Discrete symmetry violation in the standard model

The Standard Model provides explanations for two possible sources of CP violation. The first source is CP violation due to the complex phase associated with quark generation mixing in the Kobayashi-Maskawa matrix, which is described by the electroweak Lagrangian density for the quark field, denoted as

$$\mathcal{L}_{\mathrm{W}} = -\frac{e}{\sqrt{2}\sin\theta_{\mathrm{W}}}(u_L^{\dagger}, c_L\dagger, t_L^{\dagger})V_{\mathrm{KM}}\begin{pmatrix}\tilde{\sigma}^{\mu}d_L\\ \tilde{\sigma}^{\mu}s_L\\ \tilde{\sigma}^{\mu}b_L\end{pmatrix}W_{\mu}^{+} + \mathrm{h.c.} \tag{1.1}$$

where θ_{W} represents the Weinberg angle, while u_L, c_L, and t_L represent their respective eigenstates, and W_{μ}^{+} denotes the vector field propagated by the W^{+} boson. The matrix V_{KM} is the Kobayashi-Maskawa matrix, representing the mixing between quark generations, and is a 3×3 unitary matrix [10]. Additionally, the following

parameter notations are provided by the Particle Data Group (PDG) [11].

$$
\begin{aligned}
V_{\mathrm{KM}} &= \begin{pmatrix} V_{ud} & V_{us} & V_{ub} \\ V_{cd} & V_{cs} & V_{cb} \\ V_{td} & V_{ts} & V_{tb} \end{pmatrix} \\
&= \begin{pmatrix} 1 & 0 & 0 \\ 0 & c_{23} & s_{23} \\ 0 & -s_{23} & c_{23} \end{pmatrix} \begin{pmatrix} e^{-i\delta/2} & 0 & 0 \\ 0 & 1 & 0 \\ 0 & 0 & e^{i\delta/2} \end{pmatrix} \begin{pmatrix} c_{13} & 0 & s_{13} \\ 0 & 1 & 0 \\ -s_{13} & 0 & c_{13} \end{pmatrix} \begin{pmatrix} e^{i\delta/2} & 0 & 0 \\ 0 & 1 & 0 \\ 0 & 0 & e^{-i\delta/2} \end{pmatrix} \begin{pmatrix} c_{12} & s_{12} & 0 \\ -s_{12} & c_{12} & 0 \\ 0 & 0 & 1 \end{pmatrix} \\
&= \begin{pmatrix} c_{12}c_{13} & s_{12}c_{13} & s_{13}e^{-i\delta} \\ -s_{12}c_{23} - c_{12}s_{23}s_{13}e^{i\delta} & c_{12}c_{23} - s_{12}s_{23}s_{13}e^{i\delta} & s_{23}c_{13} \\ s_{12}s_{23} - c_{12}c_{23}s_{13}e^{i\delta} & -c_{12}s_{23} - s_{12}c_{23}s_{13}e^{i\delta} & c_{23}c_{13} \end{pmatrix}
\end{aligned}
\tag{1.2}
$$

Here, θ_{ij} is interpreted as the mixing angle between different quark flavors, with $s_{ij} = \sin\theta_{ij}$ and $c_{ij} = \cos\theta_{ij}$ representing the couplings between quark fields of distinct flavors. The parameter δ represents a complex phase angle, and a non-zero δ leads to the CP violation. Another possible source of CP violation arises from the θ term in Quantum Chromodynamics (QCD), which describes the strong interaction between quark colors and gluons. The CP violating term in the QCD Lagrangian ($\Delta\mathcal{L}_\theta$) is described as follows [12, 13].

$$\Delta\mathcal{L}_\theta = \frac{\theta^2}{32\pi^2} G^a_{\mu\nu}\tilde{G}^a_{\mu\nu} \tag{1.3}$$

The superscript a corresponds to the different types of gluons, ranging from 1 to 8, and G^a_μ represents the 3×3 matrix of gluon gauge fields. It is defined as $\tilde{G^a_{\mu\nu}} = (1/2)\varepsilon_{\mu\nu\alpha\beta}G^a_{\alpha\beta}$, where $\varepsilon_{\mu\nu\alpha\beta}$ is a 4-dimensional antisymmetric tensor. The parameter θ quantifies the extent of CP violation, and experiments aimed at measuring the neutron electric dipole moment have established an upper limit of $|\theta| < \mathcal{O}(10^{-10})$. This value signifies that the CP violation in the strong interactions is significantly smaller than what theoretical predictions would suggest, a phenomenon commonly known as the strong CP problem [14].

1.2 Time-reversal invariance violation

In the study of the measurement of permanent electric dipole moments (EDMs) and the CP violation through neutron scattering, the measurements are carried out with sensitivity to time reversal, rather than measurements corresponding to CP transformations. This approach is grounded in the CPT theorem, which is based on the principle that Lorentz-invariant fields always remain invariant under operations involving charge conjugation, parity reversal, and time reversal.

1.2.1 TRIV search with permanent EDMs

The possession of permanent EDMs by fundamental particles such as neutrons, protons, and electrons, as well as their composite systems, atoms, is equivalent to the time-reversal invariance violation (TRIV). Fundamental CP violation can potentially lead to the emergence of EDMs at low-energy scales through various composite systems. Over the past six decades, extensive searches for permanent EDMs have been conducted by research institutions worldwide. The Hamiltonian that describes the interaction for a particle placed in an electromagnetic field denoted as $(\boldsymbol{E}, \boldsymbol{B})$ is expressed as follows,

$$\mathcal{H} = -\boldsymbol{\mu}\cdot\boldsymbol{B} - \boldsymbol{d}\cdot\boldsymbol{E} \tag{1.4}$$

where $\boldsymbol{\mu}$ represents the magnetic moment, and $\boldsymbol{d}$ represents the EDM. Under a time-reversal operation, only the sign of the term $\boldsymbol{d}\cdot\boldsymbol{E}$ is reversed. In other words, by applying radio waves to a particle in an electromagnetic

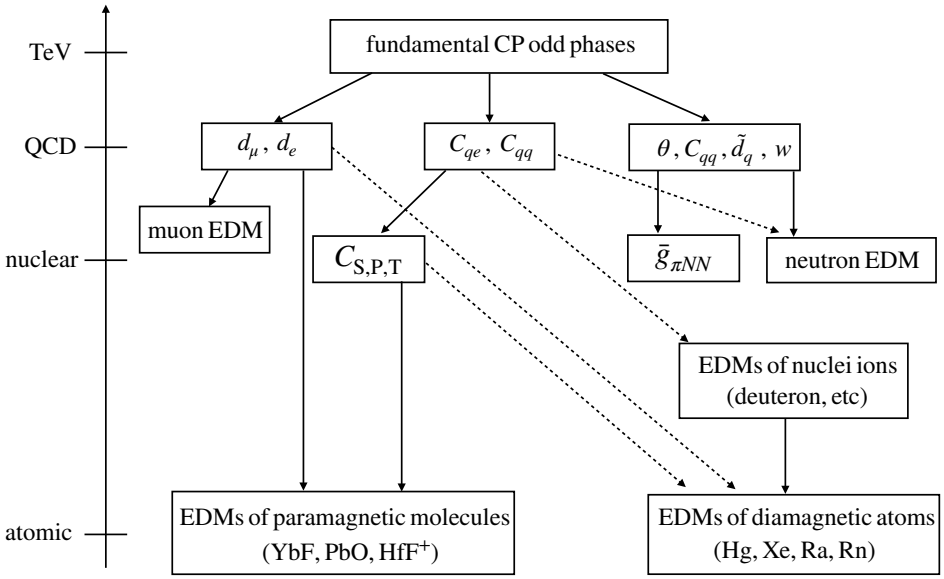

Fig. 1.1 A scheme of hierarchy in which CP-odd phase sources propagate to each energy region corresponding to generic classes of EDMs[19]. The dashed lines correspond to weaker dependencies. Each EDM search is complementary, indicating the importance of searching by experiments sensitive to each sector.

field, the Larmor precession frequency is given as $\omega = -2(\mu B \pm dE)/\hbar$, and the EDM d can be evaluated by measuring the electric field in the opposite direction as $d = \hbar\Delta\omega/4E$. Among the various EDM measurements, the neutron EDM (nEDM) provides the most stringent constraint on θ_{QCD} associated with QCD. The most recent nEDM results indicate [15]

$$|d_n| < 1.8 \times 10^{-26}\, e \cdot \mathrm{cm} \ \ (90\%\mathrm{C.L.}). \tag{1.5}$$

On the other hand, the Standard Model predicts $|d_n| \sim \mathcal{O}(10^{-32})\, e \cdot \mathrm{cm}$, a level of precision not yet achieved by current experiments. However, since the accuracy of nEDM measurements is primarily constrained by statistical uncertainties, there is potential for increased sensitivity with improvements in neutron sources. Additionally, the most recent results for the electron EDM [16] and the ^{199}Hg atom EDM [17] have been measured as follows

$$|d_e| < 4.1 \times 10^{-30}\, e \cdot \mathrm{cm} \ \ (90\%\mathrm{C.L.}) \tag{1.6}$$

$$|d_{\mathrm{Hg}}| < 7.4 \times 10^{-30}\, e \cdot \mathrm{cm} \ \ (95\%\mathrm{C.L.}). \tag{1.7}$$

These measurements have imposed constraints on many theoretical models based on BSM physics [18]. Figure 1.1 illustrates how the fundamental CP violation can propagate into different energy regions and sectors. Since EDMs for various systems exhibit varying sensitivities to CP-violating coupling constants, conducting experiments with sensitivity in multiple sectors is of utmost importance. Our research group is aiming to explore the TRIV using a novel approach through low-energy nuclear reactions, complementing EDMs measurements.

1.2.2 TRIV search with nuclear reaction

In cases where enhancement mechanisms involving compound nuclei, such as nucleon-nucleon reactions, are not present, the observed asymmetry due to PV is extremely small, on the order of 10^{-8} [20]. However, in low-energy neutron scattering with medium-heavy nuclei, PV in the vicinity of the p-wave has been enhanced to approximately 10^6, as confirmed by both theory and experiments over nearly five decades. This enhancement is understood to be induced by compound nucleus reactions, as elaborated in the next chapter, and it is expected that, along with the

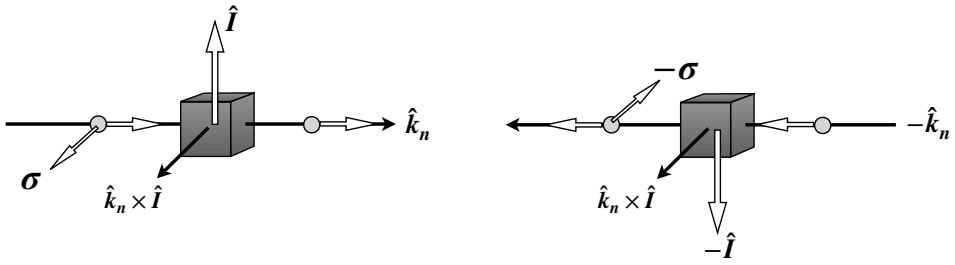

Fig. 1.2 A concept of the TRIV search with neutron transmission propagating through a polarized media. The left and right pictures indicate a corresponding time-reversed system.

enhancement of PV, the TRIV is similarly enhanced through the same mechanism. Our research group aims to explore TRIV through measurements of the transmitted neutrons in the process where low-energy neutrons with wavevector $\hat{\boldsymbol{k}}_n$ propagate through an atomic nuclei target polarized along $\hat{\boldsymbol{I}}$, as depicted in Fig.1.2. The scattering amplitude, proportional to the coefficient $\boldsymbol{\sigma} \cdot (\hat{\boldsymbol{k}}_n \times \hat{\boldsymbol{I}})$ that violates time-reversal symmetry, is obtained through this measurement. A noteworthy advantage of this measurement is that it does not exhibit false TRIV effects mediated by final-state interactions. This is because the first Born approximation is applicable for the forward scattering amplitude at zero-angle for low-energy neutrons (typically below a few eV) on nuclei, preserving the unitarity of the scattering matrix. In the context of TRIV in the nucleon system, it is essential to consider what observables appear concerning the coupling constants illustrated in Fig.1.1. Due to a lack of quantitative understanding related to the strong interaction, it is not entirely clear what coupling constants theoretically emerge. Therefore, it is valuable to compare the calculation results for PV and TRIV in neutron-proton scattering with those for composite nuclei [21, 22]. Denoting the total cross section in neutron-deuteron scattering as $\sigma_{\rm tot}$ and the cross-section for PV and TRIV as $\Delta\sigma_{\not P\not T}$, their ratio may be described as follows

$$\begin{aligned} P_{\not P\not T} &= \frac{\Delta\sigma_{\not P\not T}}{\sigma_{\rm tot}} \\ &= \frac{(-0.185\,\mathrm{bn})}{2\sigma_{\rm tot}}[\bar{g}_\pi^{(0)} + 0.26\bar{g}_\pi^{(1)} - 0.0012\bar{g}_\eta^{(0)} \\ &\quad + 0.0034\bar{g}_\eta^{(1)} - 0.0071\bar{g}_\rho^{(0)} + 0.0035\bar{g}_\rho^{(1)} + 0.0019\bar{g}_\omega^{(0)} - 0.00063\bar{g}_\omega^{(1)}]. \end{aligned} \tag{1.8}$$

The P-violating ratio may be described as follows [23]

$$\begin{aligned} P_{\not P} &= \frac{\Delta\sigma_{\not P}}{\sigma_{\rm tot}} \\ &= \frac{(0.395\,\mathrm{bn})}{2\sigma_{\rm tot}}[h_\pi^1 + h_\rho^0(0.021) + h_\rho^1(0.0027) + h_\omega^0(0.022) + h_\omega^1(-0.043) + h_\rho'^1(-0.012)]. \end{aligned} \tag{1.9}$$

Here, $\bar{g}_{\pi,\eta,\rho}^{(T)}$ and $h_{\pi,\omega,\rho}^{(T)}$ represent the coupling constants of the π, η, ρ, ω mesons characterized by P- and T-odd interactions between mesons and nucleons with isospin T. A single-meson exchange model proposed by Desplanques, Donoghue, and Holstein (DDH model) [24] is applied to Eq. 1.8 and 1.9. Due to the dominance of the coupling constants associated with π meson exchange in each equation, they may be described as [25]

$$\bar{\lambda} = \frac{\Delta\sigma_{\not P\not T}}{\Delta\sigma_{\not P}} \simeq (-0.47)\left[\frac{\bar{g}_\pi^{(0)}}{h_\pi^1} + (0.26)\frac{\bar{g}_\pi^{(1)}}{h_\pi^1}\right]. \tag{1.10}$$

This represents the unexplored parameter in low-energy neutron and nuclear reactions. The nEDM is associated with $\bar{g}_\pi^{(0)}$, and the HgEDM is associated with $\bar{g}_\pi^{(1)}$, and their upper limit may be described as [26]

$$\bar{g}_\pi^{(0)} < 1.6 \times 10^{-10}, \;\; \bar{g}_\pi^{(1)} < 0.5 \times 10^{-11}. \tag{1.11}$$

The parameter h_π^1 is determined by the γ-ray asymmetry measurement in $\vec{n}p$ scattering and the DDH model as [27]

$$h_\pi^1 = (2.6 \pm 1.2(\mathrm{stat}) \pm 0.2(\mathrm{syst})) \times 10^{-7}. \tag{1.12}$$

Therefore, the following relationship is derived from Eq.1.10.

$$|\bar{\lambda}| = \left| \frac{\Delta\sigma_{\not P \not T}}{\Delta\sigma_{\not P}} \right| < 2.9 \times 10^{-4} \tag{1.13}$$

Measurements with the potential to exceed this value indicate the possibility of improving the current EDMs experimental limits and are referred to as "discovery potential." It is important to note that these limits strongly depend on theoretical models like quark-chromo EDMs and Axion-like particles, as highlighted by Fadeev et al. [28]. The search for TRIV through neutron transmission experiments has a significant advantage in being complementary to EDMs searches. Assuming that $\bar{g}_\pi^{(T)}, \bar{g}_\eta^{(T)}, \bar{g}_\rho^{(T)}$ are of the same order, the neutron EDM d_n and deuteron EDM d_D can be expressed as follows [29]

$$\begin{aligned} d_n &\simeq 0.14(\bar{g}_\pi^{(0)} - \bar{g}_\pi^{(2)}) \ \ (\mathrm{e\,fm}) \\ d_\mathrm{D} &\simeq 0.22\bar{g}_\pi^{(1)} \ \ (\mathrm{e\,fm}). \end{aligned} \tag{1.14}$$

In other words, each of these observables has different sensitivities to models of TRIV. Therefore, Equation 1.8 corresponds to exploring a parameter space that is distinct from each EDMs search.

1.3 Overview and organization of the dissertation

The purpose of this dissertation is to identify the factors that contribute to the formulation of neutron spin observables and to provide systematic estimations for TRIV in neutron optics. The mixing angle, characterized by the compound nucleus spin J and the neutron partial width of the p-wave resonance was experimentally obtained and determined including the restriction of the previous studies. Chapter 2 presents calculations concerning the enhancement mechanisms of PV and TRIV in the compound nucleus model, along with explicit forward scattering amplitudes for the most promising target. In Chapter 3, the theoretical framework of neutron transmission experiments, the observables, and the interactions that introduce systematic uncertainties are elucidated. Chapters 4 and 5 detail the method and results of neutron transmission experiments for determining the essential p-wave mixing angle ϕ_F required for evaluating TRIV. The value of ϕ_F obtained here is independent of the final states, unlike measurements performed in previous studies using (n, γ) reactions. In Chapter 6, the causes of systematic uncertainties are summarized, and the measurement procedures necessary to achieve the sensitivity required for exploring new physics and constraining it are discussed.

Chapter 2

Theory of compound nucleus

PV in neutron reactions has been reported from both theoretical and experimental perspectives for six decades. Experimentally, PV was observed in (n,γ) reactions and (n,f) reactions in nuclear fission [30, 31]. In 1980, the helicity dependence of neutron spin rotation in unpolarized media was first reported using $^{117}\mathrm{Sn}$ [32]. Subsequently, as neutron transmission experiments, the absorption cross section depending on neutron helicity were measured for medium-heavy nuclei such as $^{117}\mathrm{Sn}$, $^{139}\mathrm{La}$, and $^{81}\mathrm{Br}$, revealing PV in the vicinity of p-wave resonances with the observed P-violating cross section being on the order of $10^{-1}-10^{-2}$ with respect to the total cross section [33]. These experimental findings were accompanied by attempts to construct theoretical models for P-violating nuclear reactions. Between 1964 and 1980, theoretical frameworks explaining P-violating nuclear reactions were reported by Michel, Stodolsky, among others. These models included treating nuclear potentials as P-odd, neglecting the intrinsic degrees of freedom of nuclei resulting from neutron interactions, or discussing exotic phenomena and the presence of new weak interaction due to nuclear reactions [34, 35, 36]. However, these theoretical models did not reconcile the significant disparities between the experimental results of P-violating spin rotations and absorption cross section and the theoretical predictions. The discrepancies were due to the consideration of idealized models such as single-particle potential resonances while overlooking the more complex internal degrees of freedom of actual nuclei. In response, Sushkov and Flambaum proposed a model to explain the substantial enhancement of PV by introducing compound nuclear states as highly excited intermediate states in nuclear reactions [37, 38]. In this compound nuclear model, they predicted two main reasons for the substantial enhancement of PV. Firstly, they attributed it to the dynamic enhancement due to the narrow level spacing between excited states in compound nuclear states, typically on the order of eV. Secondly, they suggested a structural enhancement caused by the ratio of P-invariant and varying transition matrix elements originating from s and p-wave states and nuclear structure, which scales as $\sim (k_n R)^{-1}$ (k_n represents the neutron wave number, and R denotes the nuclear radius). While Flambaum's proposal considered only PV in the vicinity of p-wave resonances in compound nuclear states, Bunakov and Gudkov developed a theory that also considered s-wave resonances, which dominate most of neutron scattering [39]. This microscopic nuclear reaction theory framework achieved consistency with the aforementioned experimental results [40]. In this chapter, we discuss the theoretical interpretation of the enhancement mechanism of symmetry violation in compound nuclear processes, along with a focus on promising target nuclei for exploring TRIV. We provide an explicit expression for the forward scattering amplitude, including tensor polarization, for the most promising nuclei $^{139}\mathrm{La}$. Furthermore, we present specific computational results for the correlation terms constituted by neutron spin, neutron momentum, and nuclear spin.

2.1 The enhancement mechanism of P-odd effects

2.1.1 Description for the P-odd amplitudes and dynamical enhancement

For the P-odd neutron elastic scattering amplitude, the reaction T and R matrices are described in association with the scattering matrix S[39, 40]. Their relationship can be expressed as

$$\hat{R} = 2\pi i\hat{T} = \mathbb{1} - \hat{S}. \tag{2.1}$$

The neutron spin, neutron orbital angular moment, neutron total angular moment, and channel spin are defined as s, l, $j = l + s$, $S = s + I$, respectively. The matrix elements of the P-odd neutron elastic scattering amplitude can be written as $R_{l'l} \equiv \langle S'l'|R^J|Sl\rangle$ from [41]. $J = l + S$, S', and l' represent the total angular moment, the channel spin, and the orbital angular moment in a final state, respectively. In the following discussion, only $l = 0, 1$ orbital angular momentum, i.e. s or p wave resonances, are considered for the interaction with low energy neutrons. To avoid complicated calculations such as spin factors, the target nuclear spin is defined as $I = 0$ and $J = j = S = S' = 1/2$. Then, the matrix elements can be expressed as

$$R_{l'l} = \langle 1/2\, l'|R^{\frac{1}{2}}|1/2\, l\rangle\,. \tag{2.2}$$

Letting $H_0, V_{\not P}$ denote the P-conserving or non-conserving potentials as the Hamiltonian H, respectively, leads to $H = H_0 + V_{\not P}$. In this case, for a normal (P-conserving) scattering process, the eigenfunction $\Psi^{\pm}$ follows as $H_0\Psi^{\pm} = E\Psi^{\pm}$, then by using the distorted wave Born approximation for the weak interaction, Eq.2.2 can be transformed as

$$R_{l'l} = 2\pi i\,\langle \Psi^-_{l'}|V_{\not P}|\Psi^+_l\rangle\,. \tag{2.3}$$

According to the shell model approach in nuclear reactions [42], the scattered wave function has the following energy dependence

$$\Psi^{\pm}_E = \sum_i a^{\pm}_i(E)\varphi^{\pm}_i + \int b^{\pm}(E, E')\chi^{\pm}_{E'}dE' \tag{2.4}$$

where φ_i is the compound nuclear wave function due to the ith resonance and $\chi_{E'}$ is the wave function due to mean field potential scattering in the nucleus. The other coefficients in Eq.2.4 is as follows

$$a^{\pm}_i(E) = \frac{\exp(\pm i\delta)}{\sqrt{2\pi}}\frac{\sqrt{\Gamma^n_i}}{E - E_i \pm i\Gamma_i/2}. \tag{2.5}$$

The neutron partial width included in this is obtained by adding the residual interaction V, which cannot be represented by the nuclear model, as a perturbation

$$\Gamma^n_i(E) = 2\pi\,|\langle\chi_{E'}|V|\varphi_i\rangle|^2 \tag{2.6}$$

Then, $b^{\pm}(E, E')$ at the outer $|E - E - E_i| > \Gamma_i$ of the compound nuclear resonance is

$$b^{\pm}(E, E') \simeq \exp(\pm i\delta)\delta(E - E') \tag{2.7}$$

which leads to the interaction between the nuclear mean field and the compound nuclear wave function. In this case, E_i, Γ_i, Γ^n_i denote the resonance energy, full width, and neutron width for the ith resonance and δ is the phase shift due to potential scattering. In Eq. 2.4, the potential scattering $\chi^{\pm}_{E'}$ can be regarded as an energy-independent constant in the neighborhood of a compound nuclear resonance, which gives the following

$$\int b^{\pm}(E, E')\chi^{\pm}_{E'}dE' \simeq \exp(\pm i\delta)\chi^{\pm}_{E'}. \tag{2.8}$$

Therefore, Eq.2.4 is then restricted to i as s, p-wave resonances to obtain

$$\Psi^{\pm}_{s,p} = a^{\pm}_{s,p}\varphi^{\pm}_{s,p} + \exp(\pm i\delta_{s,p})\chi^{\pm}_{s,p} \tag{2.9}$$

By substituting Eq.2.9 into Eq.2.3 to obtain

$$R_{01} = 2\pi i\left[a^+_s a^+_p\int\varphi_s V_{\not P}\varphi_p d\tau + a^+_s e^{i\delta_p}\int\varphi_s V_{\not P}\chi^+_p d\tau + e^{i(\delta_s+\delta_p)}\int\chi^+_s V_{\not P}\chi^+_p d\tau\right] \tag{2.10}$$

where τ represents the time of the compound nuclear state. In this equation, the first term represents the mixing of s, p-wave compound nuclear states via the weak interaction, and the second term represents the decay of compound nuclei via potential resonant scattering due to the weak interaction. The third term corresponds to the mixing of the continuous state wavefunction, with all mixing in the absence of compound nuclear resonance coming from this

term [43]. For low-energy neutrons and heavy nuclei, the first term becomes dominant due to the high resonance level density, this decreases the denominator of $a_s^+ a_p^+$. This mechanism is the dynamical enhancement described at the beginning of the chapter. Since the mixing of the continuous state wavefunction and decay of the compound nucleus contribute only when the level spacing of the s, p-wave resonances exceeds $100\,\mathrm{eV}$, when considering scattering phenomena in heavy nuclei, Eq.2.10 can be approximated as follows

$$R_{01} \simeq 2\pi i a_s^+ a_p^+ \int \varphi_s V_{\not P} \varphi_p d\tau = -R_{10} \tag{2.11}$$

where the matrix element $\int \varphi_s V_{\not P} \varphi_p d\tau$ follows the phase convention of the compound nuclear wave function [44] to obtain

$$\int \varphi_s V_{\not P} \varphi_p d\tau = -v \tag{2.12}$$

Therefore, Eq.2.11 can be described in the simple two resonance approximation from [45] as

$$R_{01} = -2i\pi a_s^+ a_p^+ v = -i \frac{\sqrt{\Gamma_s^n} v \sqrt{\Gamma_{p,j=1/2}^n}}{(E - E_s + i\Gamma_s/2)(E - E_p + i\Gamma_p/2)} = -R_{10} \tag{2.13}$$

Next, a calculation of the specific value of the matrix element V due to the mixing of parity due to dynamical enhancement is performed[40]. Let the compound nuclear wave function simply be φ and the single particle wave function Ψ_i, the mixing of compound nucleus resonances due to the strong interactions can be represented as

$$\varphi = \sum_{i=1}^{N} c_i \Psi_i. \tag{2.14}$$

With the normalization $\sum_i^N c_i^2 = 1$, where N is the number of levels in the compound nucleus. Applying the random phase approximation [46] to the matrix element $\langle \Psi_i | V_{\not P} | \Psi_k \rangle$, Eq.2.12 leads to

$$|v| = \langle \varphi_s | V_{\not P} | \varphi_p \rangle \sim \langle \Psi_i | \bar{V_{\not P}} | \Psi_k \rangle N^{-1/2} \tag{2.15}$$

where $\langle \Psi_i | \bar{V_{\not P}} | \Psi_k \rangle$ is a average matirix elements between single particles. The number of compound nucleus levels, N, can be expressed using averaged level spacing of single particle resonances, $\bar{D_0}$, and level spacing of the compound nucleus, $\bar{D}$ as

$$N \simeq \bar{D_0}/\bar{D} \tag{2.16}$$

Therefore, by substituting Eq.2.15 and Eq.2.16 for the dynamic enhancement factor, v/D, we obtain

$$\frac{|v|}{D} \simeq \frac{\langle \Psi_i | \bar{V_{\not P}} | \Psi_k \rangle N^{-\frac{1}{2}}}{N^{-1} \bar{D_0}} = \left(\frac{\langle \Psi_i | \bar{V_{\not P}} | \Psi_k \rangle}{\bar{D_0}} \right) \sqrt{N} \tag{2.17}$$

Since $N \sim 10^6$ is obtained from the value of the neutron strength function [47] in heavy nuclei, $\frac{|v|}{\bar{D}} \sim \langle \Psi_i | \bar{V_{\not P}} | \Psi_k \rangle / \bar{D_0} \times 10^3$, it is clear that PV is enhanced about $10^2 - 10^3$ compared with the inter-nucleon interaction.

2.1.2 P-odd longitudinal asymmetry

In the 1980s, measurements of neutron helicity-dependent absorption cross sections were performed by Alfimenkov [33] and confirmed that PV was greatly enhanced in the vicinity of p-wave resonances. The number of transmitted neutrons after longitudinally polarized neutrons propagated through an unpolarized medium was counted, and helicity-dependent transmission rates were measured by flipping the incident neutron spin. The longitudinal asymmetry can be defined as

$$P_L = \frac{\sigma_- - \sigma_+}{\sigma_- + \sigma_+} \tag{2.18}$$

where σ_+, σ_- are the total cross sections for incident neutrons of positive and negative helicity, respectively. In this section, the enhancement mechanism of PV in more detail by interpreting the longitudinal asymmetry from the theoretical expression for the scattering amplitude in p-wave resonance will be discussed. Equation 2.18 can be expressed using the matrix elements of the P-violating scattering amplitudes as follows

$$P_L = \frac{\mathrm{Re}(R_{10} - R_{01})}{\mathrm{Re}R_{11}} \tag{2.19}$$

where $\mathrm{Re}R_{11}$ represents the P-conserving matrix element of the scattering amplitude in p-wave resonances. This can be calculated by considering only p-wave resonances from Eq.2.2, this leads to

$$R_{11} = ie^{2i\delta_p}\frac{\Gamma_p^n}{E - E_p + i\Gamma_p/2} - 2ie^{i\delta_p}\sin\delta_p. \tag{2.20}$$

For a nuclear radius of $R_0 \sim 1.2A^{1.3}\,\mathrm{fm}$ and neutron energy $E \sim 1\,\mathrm{eV}$, the phase shift is $\delta_p \sim (k_n R_0)^3 \simeq 10^{-9}$. In this case, the potential scattering in the p-wave can be neglected. Therefore, Eq.2.20 can be described as

$$R_{11} \simeq i\frac{\Gamma_p^n}{E - E_p + i\Gamma_p/2} \tag{2.21}$$

Taking the real part as $E = E_p$, one leads to

$$\mathrm{Re}R_{11}(E = E_p) = \frac{2\Gamma_p^n}{\Gamma_p} \tag{2.22}$$

And, Eq.2.13 leads to

$$\begin{aligned}\mathrm{Re}(R_{10}(E_p) - R_{01}(E_p)) &= -\frac{4\sqrt{\Gamma_s^n}v\sqrt{\Gamma_{p,j=1/2}^n}}{(E_p - E_s)^2 + (\Gamma_s/2)^2}\frac{1}{\Gamma_p} \\ &\simeq -\frac{4\sqrt{\Gamma_s^n}v\sqrt{\Gamma_{p,j=1/2}^n}}{(E_p - E_s)\Gamma_p}\end{aligned} \tag{2.23}$$

Therefore, by substituting Eq.2.22 and Eq.2.23 into Eq.2.19, we obtain

$$P_L \simeq -\frac{2v}{E_p - E_s}\sqrt{\frac{\Gamma_{p,j=1/2}^n}{\Gamma_p^n}}\sqrt{\frac{\Gamma_s^n}{\Gamma_p^n}} \tag{2.24}$$

In this equation, $v/(E_p - E_s)$ is the aforementioned dynamic enhancement factor and $\sqrt{\Gamma_s^n/\Gamma_p^n}$ denotes the structural enhancement factor. Here, the difference in the centrifugal potentials of the s and p waves leads to

$$\Gamma_{s,p}^n \propto (k_n R_0)^{2l+1} \tag{2.25}$$

Then, one can write

$$\sqrt{\frac{\Gamma_s^n}{\Gamma_p^n}} \sim \frac{1}{k_n R_0} \tag{2.26}$$

The value of the structure factor is approximately $(k_n R_0)^{-1} \sim 10^2 - 10^3$ for a typical heavy nucleus. In other words, the P-odd effect is amplified by about $10^4 - 10^6$ due to s, p mixing in the compound nuclear process. Here, $\sqrt{\Gamma_{p,j=1/2}^n/\Gamma_p^n}$ represents the ratio of $j = 1/2$ in the p-wave neutron partial width, which can have a choice of $j = 1/2, 3/2$ in p-wave resonance, then $\Gamma_{p,j=1/2}^n/\Gamma_p^n + \Gamma_{p,j=3/2}^n/\Gamma_p^n = 1$.

$$x_F^2 \equiv \frac{\Gamma_{p,j=1/2}^n}{\Gamma_p^n},\;\; y_F^2 \equiv \frac{\Gamma_{p,j=3/2}^n}{\Gamma_p^n} \tag{2.27}$$

They satisfy the following

$$x_F^2 + y_F^2 = 1,\;\; \cos^2\phi_F + \sin^2\phi_F = 1 \tag{2.28}$$

Thus, the ratio of p-wave neutron partial widths for $j = 1/2, 3/2$ can be expressed using the mixing angle ϕ_F according to Flambaum's convention for the momentum summation [48].

2.2 The enhancement mechanism of CP-odd effects

The possibility of TRIV interactions occurring when polarized neutrons propagate through a polarized medium was almost simultaneously pointed out by Kabir and Stodolsky[49, 50]. The time evolution of polarized neutrons in polarized media will be discussed in detail in the following chapter. Here, we focus on the microscopic perspective of TRIV in nuclear reactions with nonzero spin nuclei as a target[51, 40]. The effects of TRIV can be expressed in terms of the scattering amplitude proportional to the correlation term $\boldsymbol{\sigma}_n \cdot (\hat{\boldsymbol{k}}_n \times \hat{\boldsymbol{I}})$ involving the neutron spin $\boldsymbol{\sigma}_n$, the neutron wavevector $\hat{\boldsymbol{k}}_n$, and the nuclear target spin $\hat{\boldsymbol{I}}$. Similar to P-odd effects, this effect can be obtained by measuring the precession rate $\frac{d\chi_T}{dz}$ around the $\hat{\boldsymbol{k}}_n \times \hat{\boldsymbol{I}}$ axis or by measuring the neutron absorption cross section $\Delta\sigma_T$ in the cases where the neutron spin is parallel or antiparallel and is calculated by the optical theorem as

$$\begin{aligned} \frac{d\chi_T}{dz} &= \frac{4\pi\rho}{k_n}\mathrm{Re}(f_\uparrow - f_\downarrow) \\ \Delta\sigma_T &= \frac{4\pi}{k_n}\mathrm{Im}(f_\uparrow - f_\downarrow) \end{aligned} \tag{2.29}$$

where z is the thickness of the polarized media and $f_\uparrow$, $f_\downarrow$ are the zero-angle forward scattering amplitudes to neutron spins parallel and antiparallel to the $\hat{\boldsymbol{k}}_n \times \hat{\boldsymbol{I}}$ axis, respectively. Adding a P- and T-odd matrix element w to Eq.2.12, to obtain

$$\int \varphi_s(V_{\not P} + V_{\not P\not T})\varphi_p = -v - iw \tag{2.30}$$

The potential $V_{\not P}$ and $V_{\not P\not T}$ are expressed as follows [52]

$$V_{\not P} = \begin{pmatrix} 0 & v_{01} & \dots & v_{ik} & \dots \\ v_{10} & 0 & \dots & \dots & \dots \\ \vdots & \vdots & \ddots & \dots & \dots \\ \vdots & v_{ki} & \vdots & 0 & \dots \\ \vdots & \vdots & \vdots & \vdots & \ddots \end{pmatrix}, \quad V_{\not P\not T} = \begin{pmatrix} 0 & +iw_{01} & \dots & +iw_{ik} & \dots \\ -iw_{10} & 0 & \dots & \dots & \dots \\ \vdots & \vdots & \ddots & \dots & \dots \\ \vdots & -iw_{ki} & \vdots & 0 & \dots \\ \vdots & \vdots & \vdots & \vdots & \ddots \end{pmatrix} \tag{2.31}$$

As these matrices show, $v_{ik} = 0$ and $w_{ik} = 0$ when the angular momenta i and k are of the same parity, and the P- and T-odd matrix elements are antisymmetric. Therefore, by s, p-mixing with a two-resonance approximation as in the P-odd argument, Eq.2.29 can be transformed as

$$\begin{aligned} \frac{d\chi_T}{dz} &= \frac{4\pi\rho G_J}{k_n^2}\frac{\sqrt{\Gamma_s^n}w\sqrt{\Gamma_p^n}[(E-E_s)(E-E_p) - \Gamma_s\Gamma_p/4]}{((E-E_s)^2 + i\Gamma_s/2)\,((E-E_p)^2 + i\Gamma_p/2)} \\ \Delta\sigma_T &= -\frac{2\pi G_J}{k_n^2}\frac{\sqrt{\Gamma_s^n}w\sqrt{\Gamma_p^n}[(E-E_p)\Gamma_s + (E-E_s)\Gamma_p]}{((E-E_s)^2 + i\Gamma_s/2)\,((E-E_p)^2 + i\Gamma_p/2)} \end{aligned} \tag{2.32}$$

One shows the form is similar except for G_J in Eq.2.13. Here, G_J represents a spin factor as [40]

$$G_J = -\sqrt{\frac{3}{2(2I+1)}}\frac{1}{4\pi}\left\{\sqrt{\frac{2I+1}{2I+3}}\delta_{j,I+1/2}\delta_{S,I-1/2} + \sqrt{\frac{I}{I+1}}\delta_{j,I-1/2}\delta_{S,I+1/2}\right\} \tag{2.33}$$

where δ is Kronecker's delta. Let $\Delta\sigma_P$ be the P-odd and T-even cross section of non-zero nuclear spins, and since the P- and T-odd cross section are also expected to be enhanced about 10^6, the following equation is introduced based on their analogy [53].

$$\Delta\sigma_T = \kappa(J)\frac{w}{v}\Delta\sigma_P \tag{2.34}$$

Here, $\kappa(J)$ is the ratio of the spin-dependent factor of P- and T-odd effects. Its specific formulae can be described as

$$\begin{aligned}\kappa(J=I+1/2) &= -\frac{3}{2^{3/2}}\left(\frac{2I+1}{2I+3}\right)^{3/2}\left(\frac{3}{\sqrt{2I+3}}\gamma-\sqrt{I}\right)^{-1}\\ \kappa(J=I-1/2) &= -\frac{3}{2^{3/2}}\left(\frac{2I+1}{2I-1}\right)\left(\frac{I}{I+1}\right)^{1/2}\left(-\frac{I-1}{\sqrt{2I-1}}\frac{1}{\gamma}+\sqrt{I+1}\right)^{-1}\end{aligned} \tag{2.35}$$

where γ is the ratio of neutron partial widths for different channel spins $I+1/2$, $I-1/2$, then $\gamma = [\Gamma_p^n(I+1/2)/\Gamma_p^n(I-1/2)]^{1/2}$. The value of $\kappa(J)$ here can be obtained mainly from angular correlation experiments in (n,γ) reactions [48]. In other words, the larger the value of $\kappa(J)$, the more the TRIV search is also enhanced with respect to the P-odd cross section, thus it is important to select such nuclides. Their ratio can be also defined as

$$x_S^2 \equiv \frac{\Gamma_p^n(S=I-\frac{1}{2})}{\Gamma_p^n},\ \ y_S^2 \equiv \frac{\Gamma_p^n(S=I+\frac{1}{2})}{\Gamma_p^n}. \tag{2.36}$$

The relation of the spin-coupling transformation from the Gudkov notation (x_S, y_S), $\boldsymbol{J}=\boldsymbol{l}+(\boldsymbol{s}+\boldsymbol{I})$, according to the Eq.2.27 to the Flambaum notation (x_F, y_F), $\boldsymbol{J}=\boldsymbol{I}+(\boldsymbol{l}+\boldsymbol{s})$, the relation of the spin-coupling can be transformed by the order of angular momentum composition as follows

$$\begin{aligned}|[l,(sI)S]J\rangle &= \sum_j (-1)^{l+s+I+J}\sqrt{(2j+1)(2S+1)}\begin{Bmatrix}1 & \frac{1}{2} & j\\ I & J & S\end{Bmatrix}|[I,(ls)j]J\rangle\\ &= \sum_j (-1)^{l+s+I+J}\sqrt{(2j+1)(2S+1)}\begin{Bmatrix}1 & \frac{1}{2} & j\\ I & J & S\end{Bmatrix}(-1)^{j+I-J}\,|[(ls)j,I]J\rangle\,.\end{aligned} \tag{2.37}$$

Here, the transformation in the first and second lines uses $|[I,(ls)j]J\rangle = (-1)^{j+I-J}\,|[(ls)j,I]J\rangle$ according to the definition of the $6j$ symbol and Condon-Shortley's phase convention. This transformation yields the expression (2.35) in (x_F, y_F) as follows

$$\begin{aligned}\kappa(J=I-1/2) &= \left(1-\frac{1}{2}\sqrt{\frac{2I-1}{I+1}}\frac{y_F}{x_F}\right)\\ \kappa(J=I+1/2) &= \frac{I}{I+1}\left(1+\frac{1}{2}\sqrt{\frac{2I+3}{I}}\frac{y_F}{x_F}\right).\end{aligned} \tag{2.38}$$

Thus, the spin-dependent factor $\kappa(J)$ can be interpreted by measuring the mixing angle ϕ_F. The p-wave neutron partial width ratios x_F, y_F (or x_S, y_S) for obtaining the mixing angle ϕ_F have not been established due to the complex structure of the compound nuclear process. Therefore, they are determined only by experiments sensitive to the p-wave neutron partial width ratio and its sign.

2.3 Final state interactions

In general, the measurement of T-odd angular correlation terms in scattering or particle decay does not necessarily directly relate to TRIV. As an example, the P-conserving operator in the scattering of polarized particles, $\boldsymbol{\sigma}\cdot(\boldsymbol{k}_i\times\boldsymbol{k}_f)$, is T-odd and can formally mimic time-reversal. However, the avoidance of mimicking final-state interactions by T-odd correlation terms can be achieved by treating low-energy neutrons optically. This is only valid when the zero-angle forward elastic scattering amplitude of low-energy neutrons can be described within the framework of the first Born approximation [54, 23]. Here, the condition of independence from final-state interactions in zero-angle elastic scattering is imposed by the unitarity condition of the scattering matrix as described as

$$\hat{T}^\dagger - \hat{T} = i\hat{T}\hat{T}^\dagger \tag{2.39}$$

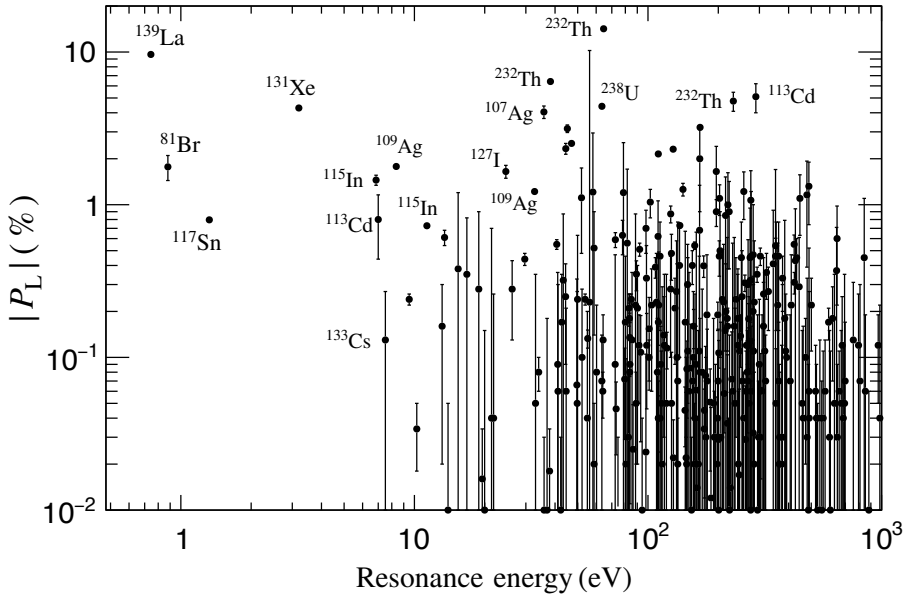

Fig. 2.1 Longitudinal asymmetry P_L for various nuclei ([55] and references therein)

When the first Born approximation is valid, the right-hand side of Eq.2.39 is extremely small and can be approximated as zero. In this case, $\hat{T}$ can be a Hermitian matrix, satisfying $\hat{T} = \hat{T}^\dagger$, then

$$\langle i|\hat{T}|f\rangle = \langle f|\hat{T}^*|i\rangle \tag{2.40}$$

The subscripts i and f represent the quantum numbers of the initial and final states, respectively. From the condition of invariance under time reversal

$$\langle f|\hat{T}|i\rangle = \langle -i|\hat{T}|-f\rangle^* \tag{2.41}$$

The negative sign implies that the particle spin and momentum have opposite signs in the corresponding states. Additionally, due to the properties of the reaction matrix,

$$\langle f|\hat{T}|i\rangle = \langle -f|\hat{T}|-i\rangle^* . \tag{2.42}$$

This condition prohibits P-odd correlations from being T-odd angular correlations. In other words, the zero-angle scattering amplitude allows it possible to obtain Eq.2.42 without violating unitarity from Eq.2.41. Consequently, the final-state interactions in neutron transmission cannot mimic TRIV T-odd correlations.

2.4 The candidate of nuclei for TRIV search

The selection of an optimal nuclide as a polarized target is crucial for exploring TRIV. As mentioned in Eq.2.34, nuclei with large longitudinal asymmetry and $\kappa(J)$ lead to enhanced TRIV. Therefore, it is essential to measure the longitudinal asymmetry and $\kappa(J)$ for multiple nuclei to evaluate the magnitude of $\Delta\sigma_T$ in advance. Moreover, as shown in Fig.2.1, previous studies have measured the longitudinal asymmetry and the corresponding resonance energies for many nuclides (see [55] and references therein). However, selecting a nuclide with large longitudinal asymmetry does not necessarily translate into more sensitive measurements. This is because it is necessary to consider both the limitations of the first Born approximation and the experimental constraints. As discussed in the previous section, applying the first Born approximation is essential for low-energy neutrons ($E_n < \mathrm{eV}$) interacting with a polarized target, to eliminate the T-odd effects associated with the final-state interactions. Furthermore, from a statistical perspective, a smaller p-wave resonance energy is advantageous, given that thermal neutrons near the peak of the Maxwellian distribution are considered as the neutron source [56].

Another experimental constraint to consider is the nuclear polarization method. The magnitude of the TRIV is proportional to the vector nuclear polarization. Therefore, increasing the nuclear polarization enhances the measurement sensitivity. The brute-force method (BF method) can be employed to forcibly polarize nuclei by utilizing a strong magnetic field and cryogenic conditions, taking advantage of nuclear spins following the Boltzmann distribution. However, in practical settings, the polarization achieved using the BF method is relatively low. For example, for nuclei with spin 7/2, such as $^{139}\mathrm{La}$, even under the conditions of sample temperature at 0.1 K and an applied magnetic field of 1 T, only about 0.4% polarization can be obtained. Therefore, in terms of achieving high polarization, nuclides for which dynamic nuclear polarization (DNP) techniques are established are preferred [57]. The DNP involves exciting unpaired electron spins using high-frequency microwave radiation and transferring polarization to nuclear spins, resulting in high nuclear polarization. For instance, a nuclear polarization of 47.5% has been reported for $\mathrm{LaAlO_3}$, which contains $^{139}\mathrm{La}$ nuclei [58]. Additionally, another polarization technique is the spin-exchange optical pumping (SEOP) method. The SEOP method polarizes alkali metal atoms by exciting them with circularly polarized infrared laser beams and subsequently transfers the polarization to nuclear spins through hyperfine interactions with the target nuclei [59]. This method yields relatively high polarization, but it is limited to gaseous targets and must be used with non-reactive target nuclei, typically noble gases.

Table 2.1 Candidate nuclei for the TRIV search.

Nuclide	E_p (eV)	P_L (%)	I	Natural abundance (%)	Typical polarization method
$^{139}\mathrm{La}$	0.75 [1]	9.55 ± 0.35 [60]	$7/2$	99.91	DNP・BF
$^{81}\mathrm{Br}$	0.88 [3]	1.77 ± 0.33 [61]	$3/2$	49.3	SEOP
$^{117}\mathrm{Sn}$	1.33 [3]	0.79 ± 0.04 [62]	$1/2$	8.6	DNP
$^{131}\mathrm{Xe}$	3.2 [3]	4.3 ± 0.2 [63]	$3/2$	21.2	SEOP
$^{115}\mathrm{In}$	6.85 [3]	-1.45 ± 0.11 [64]	$9/2$	95.72	DNP

From the above technical constraints, the candidate nuclides, nuclear resonance parameters, and nuclear polarization method are shown in Fig.2.1. Based on the above, we consider $^{139}\mathrm{La}$ to be the most promising nuclide, because it satisfies both the p-wave resonance energy and the longitudinal asymmetry conditions, and has a track record of nuclear polarization by the DNP method with $\mathrm{LaAlO_3}$. On the other hand, due to the $7/2$ of nuclear spin, not only the simplest vector polarization but also the 2nd- and 3rd-rank tensor polarization must be considered at the same time for the scattering amplitude.

2.5 The mixing angle of previous experiments in (n, γ) reactions

The angular correlations in the (n, γ) reactions for $^{139}\mathrm{La}$ have been measured using two different experiments, which are caused by the neutron-induced p-wave resonances associated with the s- and p-wave resonances. Therefore, the specifical values of x_F and y_F can be extracted from the correlation terms depending on neutron spin σ_n, neutron momentum k_n, γ-ray spin σ_γ, and γ-ray momentum k_γ [48]. The differential cross-section in the (n, γ) reactions describing up to the first four terms can be written as [48]

$$\frac{d\sigma_{n\gamma'}}{d\Omega_\gamma} = \frac{1}{2}\left(a_0 + a_1 \hat{\boldsymbol{k}}_n \cdot \hat{\boldsymbol{k}}_\gamma + a_2 \boldsymbol{\sigma}_n \cdot (\hat{\boldsymbol{k}}_n \times \hat{\boldsymbol{k}}_\gamma) + a_3 \left((\hat{\boldsymbol{k}}_n \cdot \hat{\boldsymbol{k}}_\gamma)^2 - \frac{1}{3}\right)\right), \tag{2.43}$$

where a_0 represents the angular independent term and is composed as the sum of both the s- and p-wave differential cross sections, denoted as $a_{0\mathrm{s}}$ and $a_{0\mathrm{p}}$. The specific expressions for a_0, a_1, a_2, and a_3 can be described as

$$\begin{aligned}
a_0 &= \sum_s |V_1|^2 + \sum_p |V_2|^2, \\
a_1 &= 2\mathrm{Re} \sum_{s,p,j} V_1 V_2^* P(J_s J_p \frac{1}{2} j 1 I F) z_{p,j}, \\
a_2 &= -2\mathrm{Im} \sum_{s,p,j} V_1 V_2^* P(J_s J_p \frac{1}{2} j 1 I F) z_{p,j}, \\
a_3 &= 3\sqrt{10}\mathrm{Re} \sum_{s,K_p',j'} V_2 V_2^* P(J_s J_{K_p'} j j' 2 I F) \begin{Bmatrix} 2 & 1 & 1 \\ 0 & \frac{1}{2} & \frac{1}{2} \\ 2 & j & j' \end{Bmatrix} z_{p,j} z_{p,j'},
\end{aligned} \tag{2.44}$$

where F is a spin of the final state, the primed subscriptions are the final state, and $z_{p,j}$ corresponds to $x_F(j=1/2)$ or $y_F(j=3/2)$. V_1 and V_2 are the amplitude in s- or p-wave states as an entrance channel corresponding to the neutron absorption process and exit channels via γ-rays emission. In case of the interference between the s- and p-wave amplitude is taken into account, V_1 and V_2 are described as [48]

$$\begin{aligned}
V_1 &= -\frac{1}{2k_n} \frac{\sqrt{g_s \Gamma_s^n \Gamma_{s,f}^\gamma}(1+\alpha)}{E - E_s + i\Gamma_s/2}, \\
V_2 &= -\frac{1}{2k_n} \frac{\sqrt{g_p \Gamma_p^n \Gamma_{p,f}^\gamma}}{E - E_p + i\Gamma_p/2},
\end{aligned} \tag{2.45}$$

where Γ_f^γ is the partial γ width to f-th final state, α is the contribution of the other far s-wave resonances. The angular correlation terms, which correspond to a_1, a_2, and a_3, for the γ-rays emission derived from the transition to the ground state of ^{140}La have been reported in Ref.[65, 66]. The ratios of the partial γ width to the ground state have been determined as [65]

$$\frac{\Gamma_{s0,\mathrm{gnd}}^\gamma}{\Gamma_{s0}^\gamma} : \frac{\Gamma_{s1,\mathrm{gnd}}^\gamma}{\Gamma_{s1}^\gamma} : \frac{\Gamma_{p,\mathrm{gnd}}^\gamma}{\Gamma_p^\gamma} = 1 : 0.009 \pm 0.006 : 0.796 \pm 0.020. \tag{2.46}$$

The correlation term measurements in (n,γ) reactions with unpolarized and polarized neutron beam for the 0.75 eV p-wave resonance using a germanium detector assembly and a neutron polarizer with ^{3}He gas spin filter have been performed at the ANNRI instrument [67], the beam port 04 shown in Fig4.1, in J-PARC. The analyzed γ-ray possesses an energy of 5161 keV, signifying the transition from the compound state involving ^{139}La + n to the ground state of ^{140}La.

The angular distribution of γ-rays measured with an unpolarized neutron beam, as reported in Ref.[65], corresponds to the a_1 term in Eq.2.43. This term represents the correlation between the incident neutron momentum and the γ-ray emission angle θ_γ. The resonance shape of the angular dependence was assessed by examining the difference in γ-ray counts between the lower and higher energy regions of neutrons at the 0.75 eV p-wave resonance. The experimentally obtained correlation terms were

$$\frac{a_1}{a_0} = -0.409 \pm 0.024, \quad \frac{a_3}{a_0} = -0.191 \pm 0.028. \tag{2.47}$$

The angular distribution is compared with the theoretical expression described as a function of x_F and y_F as follows

$$\frac{a_1}{a_0} = 0.30 x_F - 0.35 y_F, \tag{2.48}$$

$$\frac{a_3}{a_0} = -0.20 x_F y_F + 0.033 y_F^2. \tag{2.49}$$

The solutions of x_F and y_F of Eq.2.48 on the unit circle in Eq.2.28 are obtained as,

$$(x_F, y_F) = (-0.23^{+0.12}_{-0.12}, 0.97^{+0.02}_{-0.04}), (-0.93^{+0.06}_{-0.04}, 0.37^{+0.12}_{-0.12}). \tag{2.50}$$

Here, equation 2.49 does not intersect with the unit circle.

The angular distribution of γ-rays obtained with a polarized neutron beam, as reported in Ref.[66, 68], is associated with the a_2 term. This term represents the correlation among the incident neutron momentum, γ-ray emission angle, and neutron polarization orientation, as indicated in Eq.2.43. The transverse asymmetry, denoted as $A_{\rm LR}$, was obtained as follows

$$A_{\rm LR} = -0.60 \pm 0.19 \tag{2.51}$$

The transverse asymmetry should be multiplied by

$$1 - \frac{a_3}{a_{0\rm p}} \left(\cos^2 \theta_\gamma - \frac{1}{3} \right) \tag{2.52}$$

to compare with the theoretical expression due to the contribution from a_3 in the denominator. In the measurement, the experimental coordinate of $\theta_\gamma = \pi/2$ was satisfied. Consequently, Eq.2.52 is described as $1 - a_3/3a_{0\rm p}$. The theoretical expression, expressed as a function of x_F and y_F, gives

$$A_{\rm LR} \left(1 - \frac{a_3}{3a_{0p}} \right) = 0.72 x_F + 0.42 y_F. \tag{2.53}$$

As the transverse asymmetry was derived by subtracting the s-wave component, a_3/a_0 is corrected by multiplying a_0/a_{0p}, where the value $a_0/a_{0p} = 2.2$ is calculated based on Eq.2.46 and the resonance parameters in Ref[65]. Therefore, the experimental value of Eq.2.53 is obtained as -0.52 ± 0.17. Therefore, the solutions of x_F and y_F on the unit circle are obtained as,

$$(x_F, y_F) = (-0.93^{+0.13}_{-0.06}, 0.37^{+0.24}_{-0.26}), \ \ (-0.14^{+0.26}_{-0.27}, -0.99^{+0.07}_{-0.01}). \tag{2.54}$$

Equation 2.48, 2.49, and 2.53 are illustrated in Fig.2.2 with the unit circle in Eq.2.28. Since each result can be interpreted as a probability density function (PDF) on the unit circle, we define the PDFs for Eq.2.48, 2.49, and 2.53 as P_{a1}, P_{a_3}, and P_{a_2}, respectively. These are functions whose integral over the unit circle satisfies one. As depicted in Fig.2.3, the product of $P_{a_1} P_{a_3} P_{a_2}$ gives a plausible ϕ_F distribution as

$$\phi_F = (149 \pm 6)^\circ. \tag{2.55}$$

Here, the error indicates the region of 68% C.L. from the central value. As can be seen from Eq.2.44, the amplitudes in the (n, γ) reactions depend not only on the entrance channel but also on the exit channel. Therefore, the value of the value of the mixing angle involves more ambiguity since the spectroscopic parameters for γ-ray emission must be determined by experiment, as indicated by the fact that Eq.2.49 does not intersect with the unit circle.

2.6 Analysis of the forward scattering amplitude for ^{139}La

2.6.1 Scattering amplitude with irreducible spherical tensor

In sections 2.1.1 and 2.2, the spin factor in the $\hat{R}$ matrix was discussed in a simplified manner. On the other hand, in the TRIV search, all possible systematic effects should be taken into account. It is necessary to give detailed neutron spin dynamics for a target with arbitrary nuclear polarization. Thus, the zero-angle forward scattering amplitude for nuclear spins $I > 1/2$ will be calculated based on [69, 70], taking into account not only vector polarization but also higher-order tensor polarization [71, 72]. Let $\rho_{MM'}$ be the density matrix of the polarized target, the scattering amplitude is calculated as follows

$$f = {\rm Tr}(f_{MM'} \rho_{MM'}) \tag{2.56}$$

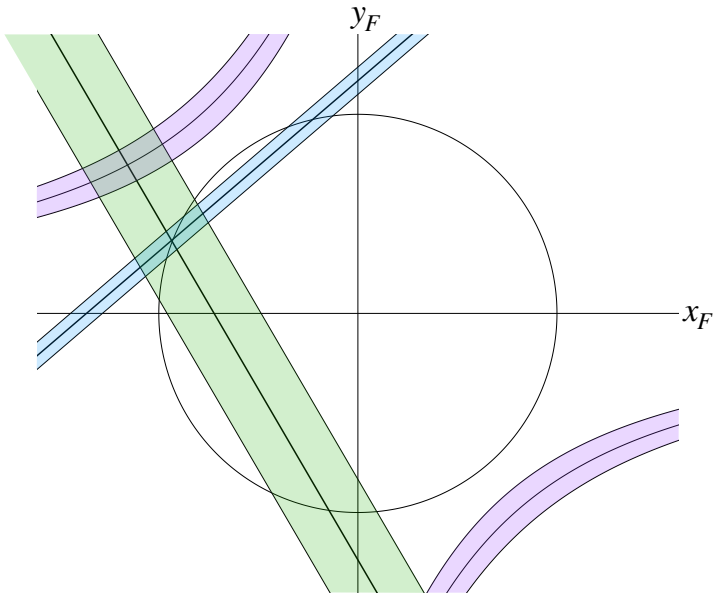

Fig. 2.2 Visualization of the value ϕ_F in the reaction of $^{139}\mathrm{La} + \mathrm{n}$ on (x_F, y_F) plane. The blue, purple, and green filled areas represent Eqs.2.48, 2.49, and 2.53, respectively. The corresponding filled areas correspond to 1σ region. The solid lines are the central values.

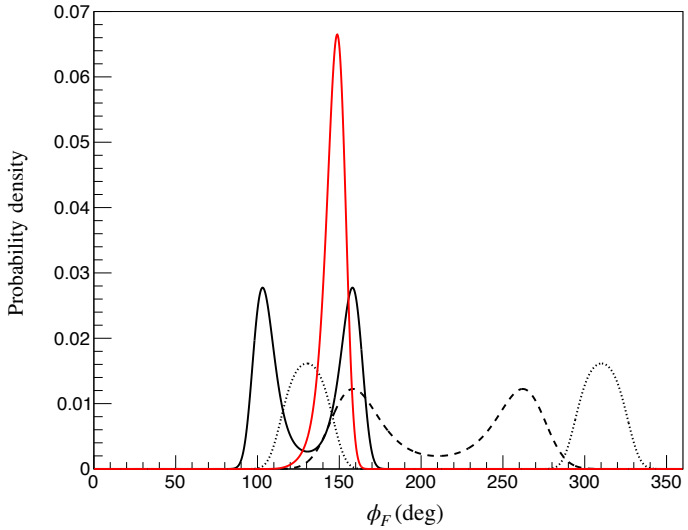

Fig. 2.3 PDFs for ϕ_F on the unit circle. The solid, dashed, and dotted lines represent P_{a_1}, P_{a_2} and P_{a_3}, respectively. The red line represents the product of $P_{a_1} P_{a_3} P_{a_2}$.

where the primed parameter corresponds to the exit channel. Using the neutron spin projection μ and the nuclear spin projection M with the z axis as the quantization axis, the following is expressed as

$$\begin{aligned} f_{MM'} =& \frac{i\pi}{2k} \sum_{Jll'Sm_sS'm'_s} Y_{Lm_L}(\theta,\phi) \left\langle s\mu' IM' \mid S'm'_s \right\rangle \left\langle Sm_s \mid s\mu IM \right\rangle \\ & \times \left\langle S'l'\alpha'_K \left| R^J \right| Sl\alpha_K \right\rangle (-1)^{J+S'+l'+l}(2J+1) \\ & \times \sqrt{\frac{(2l+1)\,(2l'+1)}{4\pi(2S+1)}} \\ & \times \langle l0l'0 \mid L0\rangle \left\langle Lm_L S'm'_s \mid Sm_s \right\rangle \begin{Bmatrix} l' & l & L \\ S & S' & J \end{Bmatrix} \end{aligned} \tag{2.57}$$

where $f_{MM'}$ is the forward scattering amplitude, θ and ϕ describe the neutron momentum direction, and α_K is the internal quantum number in the compound nucleus. Let the target spin direction coincide with the quantization axis, then the target density matrix $\rho_{MM'}$ is determined by the q-order tensor t_{q0} by [71]

$$\rho_{MM'} = \sum_{qk} \sqrt{\frac{2q+1}{2I+1}} \left\langle IMq0 | IM' \right\rangle t_{q0}. \tag{2.58}$$

To represent the neutron spin $\boldsymbol{\sigma}$ with arbitrary orientation, let the neutron spinor component $\begin{pmatrix} \tilde{x} \\ \tilde{y} \end{pmatrix}$ in a spherical coordinate system with polar angle β_n and azimuthal angle α_n as follows

$$\tilde{x} = \cos(\beta_n/2)e^{-i\alpha_n/2}, \quad \tilde{y} = \sin(\beta_n/2)e^{i\alpha_n/2}. \tag{2.59}$$

Therefore, the forward scattering amplitude for polarized neutrons can be calculated by using the spherical tensor polarization P_q^I of the polarized target as

$$\begin{aligned} f(\tilde{x},\tilde{y}) =& \frac{i\pi}{2k} \sum_{q=0}^{2I} \frac{P_q^I}{c_q^I} \tilde{\tau}_{q0} \sqrt{2q+1} \Bigg[\sum_{JMll'SS'} Y_{Lm_L}(\theta,\phi) N\left(\tilde{x},\tilde{y},S,S',M,M\right) \\ & \times \langle IMq0 \mid IM\rangle \left\langle S'l'\alpha'_K \left| R^J \right| Sl\alpha_K \right\rangle (-1)^{J+S'+l'+l}(2J+1) \sqrt{\frac{(2l+1)\,(2l'+1)}{4\pi(2S+1)}} \\ & \times \langle l0l'0 \mid L0\rangle \begin{Bmatrix} l' & l & L \\ S & S' & J \end{Bmatrix} \Bigg] = \sum_{q=0}^{2I} P_q^I f_q. \end{aligned} \tag{2.60}$$

Here, the statistical tensor $\tilde{\tau_{0q}}$ is defined as the expectation of the convention tensor spin operator and $\tilde{\tau_{0q}} = \langle \tau_{0q} \rangle$. Where P_q^I denotes the tensor polarization of the q-order to the nuclear spin I and

$$P_q^I = \frac{\bar{\tau}_q^I}{(\tau_{q,0})_{II}}. \tag{2.61}$$

Let m be the magnetic substate of the nuclear spin I, respectively, as follows

$$\begin{aligned} \frac{1}{(\tau_{q,0}^I)_{II}} &= \frac{1}{\sqrt{(2I+1)(2q+1)}} \sqrt{\frac{(2I-q)!}{(2I)!}} \sqrt{\frac{(2I+q+1)!}{(2I)!}} \\ (\tau_{q,k}^j)_{m'm} &= \langle jm'|\tau_{qk}^j|jm\rangle = \sqrt{2q+1}\,\langle jmqk|jm'\rangle \\ \bar{\tau}_q^I &= \sum_{m=-I}^{I} \langle Ik|\tau_{q0}^I|Ik\rangle\,, \quad c_q^I = \frac{1}{(\tau_{q,0}^I)_{II}} \end{aligned} \tag{2.62}$$

The following equation is also introduced to express neutron polarization.

$$\begin{aligned} N(\tilde{x},\tilde{y},S,S',M,M') =& \frac{1}{|\tilde{x}|^2+|\tilde{y}|^2}\left(|\tilde{x}|^2\left\langle\frac{1}{2}\frac{1}{2}IM \mid SM+\frac{1}{2}\right\rangle\left\langle\frac{1}{2}\frac{1}{2}IM' \mid S'M+\frac{1}{2}\right\rangle\left\langle LOS'M'+\frac{1}{2} \mid SM+\frac{1}{2}\right\rangle\delta_{m_L,0}\right. \\ &+\tilde{x}\tilde{y}^*\left(\frac{1}{2}-\frac{1}{2}IM\left|SM-\frac{1}{2}\right\rangle\left\langle\frac{1}{2}\frac{1}{2}IM' \mid S'M'+\frac{1}{2}\right\rangle\left\langle L1S'M'-\frac{1}{2} \mid SM+\frac{1}{2}\right\rangle\delta_{m_L,1}\right. \\ &+\tilde{x}^*\tilde{y}\left(\frac{1}{2}-\frac{1}{2}IM\left|SM-\frac{1}{2}\right\rangle\left\langle\frac{1}{2}\frac{1}{2}IM' \mid S'M+\frac{1}{2}\right\rangle\left\langle L-1S'M'+\frac{1}{2} \mid SM-\frac{1}{2}\right\rangle\delta_{m_L,-1}\right. \\ &\left.\left.+|\tilde{y}|^2\left(\frac{1}{2}-\frac{1}{2}IM\left|SM-\frac{1}{2}\right\rangle\left(\frac{1}{2}-\frac{1}{2}IM'\left|S'M-\frac{1}{2}\right\rangle\right\langle L0S'M'-\frac{1}{2}\right|SM-\frac{1}{2}\right)\delta_{m_L,0}\right)\right. \end{aligned} \tag{2.63}$$

Here, put the neutron momentum direction vector to the $y-z$ plane, $\phi=\pi/2$, which can be described by θ. Then, by using the unit vectors of neutron spins $\boldsymbol{\sigma}$, $\hat{\boldsymbol{I}}$, and $\hat{\boldsymbol{k}}_n$, the correlation term can be expressed by the angle parameter as follows

$$\begin{aligned} &(\hat{\boldsymbol{k}}_n\cdot\hat{\boldsymbol{I}})=\cos\theta,\ \ (\boldsymbol{\sigma}\cdot\hat{\boldsymbol{I}})=\cos\beta_n,\ \ (\boldsymbol{\sigma}\cdot\hat{\boldsymbol{k}}_n)=\cos\theta\cos\beta_n+\sin\theta\sin\beta_n\sin\alpha_n \\ &[\hat{\boldsymbol{k}}_n\times\hat{\boldsymbol{I}}]=\sin\theta,\ \ (\boldsymbol{\sigma}\cdot[\hat{\boldsymbol{k}}_n\times\hat{\boldsymbol{I}}])=\cos\alpha_n\sin\theta\sin\beta_n \end{aligned} \tag{2.64}$$

Using the above equation and expanding Eq.2.60 as the coefficients of the correlation terms of neutron spin, neutron momentum, and nuclear spin vector, the following equation is finally obtained as

$$\begin{aligned} f =& A'+B'(\boldsymbol{\sigma}\cdot\hat{\boldsymbol{I}})+C'(\boldsymbol{\sigma}\cdot\hat{\boldsymbol{k}}_n)+D'(\boldsymbol{\sigma}\cdot[\hat{\boldsymbol{k}}_n\times\hat{\boldsymbol{I}}])+H'(\hat{\boldsymbol{k}}_n\cdot\hat{\boldsymbol{I}})+K'(\boldsymbol{\sigma}\cdot\hat{\boldsymbol{k}}_n)(\hat{\boldsymbol{k}}_n\cdot\hat{\boldsymbol{I}}) \\ &+E'\left[(\hat{\boldsymbol{k}}_n\cdot\hat{\boldsymbol{I}})(\hat{\boldsymbol{k}}_n\cdot\hat{\boldsymbol{I}})-\frac{1}{3}(\hat{\boldsymbol{k}}_n\cdot\hat{\boldsymbol{k}}_n)(\hat{\boldsymbol{I}}\cdot\hat{\boldsymbol{I}})\right]+F'\left[(\boldsymbol{\sigma}\cdot\hat{\boldsymbol{I}})(\hat{\boldsymbol{k}}_n\cdot\hat{\boldsymbol{I}})-\frac{1}{3}(\boldsymbol{\sigma}\cdot\hat{\boldsymbol{k}}_n)(\hat{\boldsymbol{I}}\cdot\hat{\boldsymbol{I}})\right] \\ &+G'(\boldsymbol{\sigma}\cdot[\hat{\boldsymbol{k}}_n\times\hat{\boldsymbol{I}}])(\hat{\boldsymbol{k}}_n\cdot\hat{\boldsymbol{I}})+B'_3(\boldsymbol{\sigma}\cdot\hat{\boldsymbol{I}})\left[(\hat{\boldsymbol{k}}_n\cdot\hat{\boldsymbol{I}})(\hat{\boldsymbol{k}}_n\cdot\hat{\boldsymbol{I}})-\frac{1}{3}(\hat{\boldsymbol{k}}_n\cdot\hat{\boldsymbol{k}}_n)(\hat{\boldsymbol{I}}\cdot\hat{\boldsymbol{I}})\right]+\cdots, \end{aligned} \tag{2.65}$$

The properties of each coefficient obtained in this equation are summarized in a Table.2.2.

Table 2.2 Properties of the coefficients of the forward scattering amplitude with nuclear spin I

	A'	C'	B'	D'	H'	K'	E'	F'	G'	B'_3
q	0	0	1	1	1	1	2	2	2	3
$P-$	even	odd	even	odd	odd	even	even	odd	even	even
$T-$	even	even	even	odd	even	even	even	even	odd	even

2.6.2 Complete expression

We will discuss an explicit forward scattering amplitude for ^{139}La, which is the most promising candidate as a polarized target. Since ^{139}La has nuclear spin $I=7/2$, the spherical tensor can take the maximum $q=2I=7$. However, for low-energy neutrons corresponding to about p-wave resonance energy (0.75 eV), the higher-order orbital angular momentum ($l>1$) contribution is negligible, then it is sufficient to treat up to $q=3$ tensor polarization [70]. Therefore, for Eq.2.60, expanding to $q\leq 3$ for $I=7/2$, Eq.2.65 is calculated as follows

$$\begin{aligned} f_{7/2} =& A'+P_1H'(\hat{\boldsymbol{k}}_n\cdot\hat{\boldsymbol{I}})+P_2E'\left((\hat{\boldsymbol{k}}\cdot\hat{\boldsymbol{I}})^2-\frac{1}{3}\right)+(\boldsymbol{\sigma}\cdot\hat{\boldsymbol{I}})\left(P_1B'+P_2F'(\hat{\boldsymbol{k}}\cdot\hat{\boldsymbol{I}})+P_3\frac{B'_3}{3}\left((\hat{\boldsymbol{k}}\cdot\hat{\boldsymbol{I}})-1\right)\right) \\ &+(\boldsymbol{\sigma}\cdot\hat{\boldsymbol{k}}_n)\left(C'+P_1K'(\hat{\boldsymbol{k}}_n\cdot\hat{\boldsymbol{I}})-P_2\frac{F'}{3}+P_3\frac{2B'_3}{3}(\hat{\boldsymbol{k}}\cdot\hat{\boldsymbol{I}})\right)+\boldsymbol{\sigma}\cdot(\hat{\boldsymbol{k}}\times\hat{\boldsymbol{I}})\left(P_1D'+P_2G'(\hat{\boldsymbol{k}}_n\cdot\hat{\boldsymbol{I}}).\right) \end{aligned} \tag{2.66}$$

In this equation, the expression is transformed as the coefficients of the neutron spin correlation term to simplify the expression, and each primed coefficient can correspond as follows (typographical error corrected of [70]).

$$
\begin{aligned}
A' =& \frac{i}{32k}\left(7\left\langle 3,0\left|R^3\right|3,0\right\rangle + 9\left\langle 4,0\left|R^4\right|4,0\right\rangle + 7\left\langle 3,1\left|R^3\right|3,1\right\rangle + 9\left\langle 3,1\left|R^4\right|3,1\right\rangle + 7\left\langle 4,1\left|R^3\right|4,1\right\rangle + 9\left\langle 4,1\left|R^4\right|4,1\right\rangle\right)\\
B' =& -\frac{i}{32k}\left(7\left\langle 3,0\left|R^3\right|3,0\right\rangle - 7\left\langle 4,0\left|R^4\right|4,0\right\rangle + \frac{21}{4}\left\langle 3,1\left|R^3\right|3,1\right\rangle + \frac{21}{4\sqrt{3}}\left(\left\langle 3,1\left|R^3\right|4,1\right\rangle + \left\langle 4,1\left|R^3\right|3,1\right\rangle\right)\right.\\
&\left. -\frac{9}{20}\sqrt{35}\left(\left\langle 3,1\left|R^4\right|4,1\right\rangle + \left\langle 4,1\left|R^4\right|3,1\right\rangle\right) - \frac{91}{12}\left\langle 4,1\left|R^3\right|4,1\right\rangle + \frac{39}{4}\left\langle 3,1\left|R^4\right|3,1\right\rangle - \frac{63}{20}\left\langle 4,1\left|R^4\right|4,1\right\rangle\right)\\
C' =& \frac{i}{64k}\left(7\left(\left\langle 3,0\left|R^3\right|3,1\right\rangle + \left\langle 3,1\left|R^3\right|3,0\right\rangle\right) - 7\sqrt{3}\left(\left\langle 3,0\left|R^3\right|4,1\right\rangle + \left\langle 4,1\left|R^3\right|3,0\right\rangle\right)\right.\\
&\left. +3\sqrt{21}\left(\left\langle 4,0\left|R^4\right|3,1\right\rangle + \left\langle 3,1\left|R^4\right|4,0\right\rangle\right) - 3\sqrt{15}\left(\left\langle 4,0\left|R^4\right|4,1\right\rangle + \left\langle 4,1\left|R^4\right|4,0\right\rangle\right)\right)\\
D' =& \frac{1}{16k}\left(\frac{7}{\sqrt{3}}\left(\left\langle 3,0\left|R^3\right|4,1\right\rangle - \left\langle 4,1\left|R^3\right|3,0\right\rangle\right) + \sqrt{21}\left(\left\langle 4,0\left|R^4\right|3,1\right\rangle - \left\langle 3,1\left|R^4\right|4,0\right\rangle\right)\right)\\
H' =& -\frac{i}{64k}\left(21\left(\left\langle 3,0\left|R^3\right|3,1\right\rangle + \left\langle 3,1\left|R^3\right|3,0\right\rangle\right) - \frac{7}{\sqrt{3}}\left(\left\langle 3,0\left|R^3\right|4,1\right\rangle + \left\langle 4,1\left|R^3\right|3,0\right\rangle\right)\right.\\
&\left. +\sqrt{21}\left(\left\langle 4,0\left|R^4\right|3,1\right\rangle + \left\langle 3,1\left|R^4\right|4,0\right\rangle\right) + 7\sqrt{15}\left(\left\langle 4,0\left|R^4\right|4,1\right\rangle + \left\langle 4,1\left|R^4\right|4,0\right\rangle\right)\right)\\
K' =& -\frac{3i}{128k}\left(7\left\langle 3,1\left|R^3\right|3,1\right\rangle - 7\sqrt{3}\left(\left\langle 3,1\left|R^3\right|4,1\right\rangle + \left\langle 4,1\left|R^3\right|3,1\right\rangle\right)\right.\\
&\left. +\frac{77}{9\sqrt{3}}\left\langle 4,1\left|R^3\right|4,1\right\rangle - 3\left\langle 3,1\left|R^4\right|3,1\right\rangle + \frac{9}{5}\sqrt{35}\left(\left\langle 3,1\left|R^4\right|4,1\right\rangle + \left\langle 4,1\left|R^4\right|3,1\right\rangle\right) - \frac{77}{5}\left\langle 4,1\left|R^4\right|4,1\right\rangle\right)\\
E' =& \frac{9i}{256k}\left(\frac{35}{3}\left\langle 3,1\left|R^3\right|3,1\right\rangle - \frac{7}{\sqrt{3}}\left(\left\langle 3,1\left|R^3\right|4,1\right\rangle + \left\langle 4,1\left|R^3\right|3,1\right\rangle\right) - \frac{77}{9}\left\langle 4,1\left|R^3\right|4,1\right\rangle + \frac{3}{5}\sqrt{35}\left(\left\langle 3,1\left|R^4\right|4,1\right\rangle\right.\right.\\
&\left.\left. + \left\langle 4,1\left|R^4\right|3,1\right\rangle\right) - 5\left\langle 3,1\left|R^4\right|3,1\right\rangle + \frac{77}{5}\left\langle 4,1\left|R^4\right|4,1\right\rangle\right)\\
F' =& \frac{3i}{320k}\left(35\left(\left\langle 3,0\left|R^3\right|3,1\right\rangle + \left\langle 3,1\left|R^3\right|3,0\right\rangle\right) + \frac{35}{\sqrt{3}}\left(\left\langle 3,0\left|R^3\right|4,1\right\rangle + \left\langle 4,1\left|R^3\right|3,0\right\rangle\right)\right.\\
&\left. -5\sqrt{21}\left(\left\langle 4,0\left|R^4\right|3,1\right\rangle + \left\langle 3,1\left|R^4\right|4,0\right\rangle\right) - 7\sqrt{15}\left(\left\langle 4,0\left|R^4\right|4,1\right\rangle + \left\langle 4,1\left|R^4\right|4,0\right\rangle\right)\right)\\
G' =& -\frac{3}{32\sqrt{5}k}\left(7\sqrt{\frac{5}{3}}\left(\left\langle 3,1\left|R^3\right|4,1\right\rangle - \left\langle 4,1\left|R^3\right|3,1\right\rangle\right) - 3\sqrt{7}\left(\left\langle 3,1\left|R^4\right|4,1\right\rangle - \left\langle 4,1\left|R^4\right|3,1\right\rangle\right)\right)\\
B_3' =& \frac{9i}{256k}\left(7\left\langle 3,1\left|R^3\right|3,1\right\rangle + \left(\left\langle 3,1\left|R^3\right|4,1\right\rangle + \frac{7}{\sqrt{3}}\left\langle 4,1\left|R^3\right|3,1\right\rangle\right) + \frac{7}{3}\left\langle 4,1\left|R^3\right|4,1\right\rangle\right.\\
&\left. -3\sqrt{\frac{7}{5}}\left(\left\langle 3,1\left|R^4\right|4,1\right\rangle + \left\langle 4,1\left|R^4\right|3,1\right\rangle\right) - 3\left\langle 3,1\left|R^4\right|3,1\right\rangle - \frac{21}{5}\left\langle 4,1\left|R^4\right|4,1\right\rangle\right)
\end{aligned}
\tag{2.67}
$$

Here, each matrix element in the above equation can be calculated in the same way as in Eq.2.2. The P-conserving matrix elements are

$$
\langle S'lK|R^J|SlK\rangle = \sum_K i\frac{\sqrt{\Gamma^n_{l_K}(S'_K)}\sqrt{\Gamma^n_{l_K}(S_K)}}{E-E_K+i\Gamma_K/2}\exp(i[\delta_{l_K}(S'_K)+\delta_{l_K}(S_K)])-2i\exp(i\delta_{l_K}(S_KS'_K))\sin\delta_{\delta_{l_K}}(S_KS'_K).
\tag{2.68}
$$

where K corresponds to the Kth compound nuclear resonance. For p-wave resonances ($l=1$), potential scattering can be neglected from Eq.2.25. The P- and T-odd matrix elements can similarly be represented by the two-resonance approximation of s and p-waves, and from $V_{\not P}$, $V_{\not P\not T}$ by the Eq.2.30 the following can be obtained as

$$
\langle S'l'|R^J|Sl\rangle = i\frac{\sqrt{\Gamma^n_{l'}(S')}(-v-iw)\sqrt{\Gamma^n_l(S)}}{E-E_l+i\Gamma_l/2}\exp(i[\delta_{l'}(S')+\delta_l(S)]).
\tag{2.69}
$$

The above equation is then used to introduce the specific form of Eq.2.67. Since the p-wave resonance is $J = 4$, all matrix elements with total angular momentum $J = 3$ in Eq.2.69 can be ignored, due to that it only mixes with the $S_0\,(J = 4)$ resonance, not the $S_1\,(J = 3)$ resonance. Therefore, Eq.2.67 can be calculated as follows using equation (2.36), which is the p-wave neutron partial width ratio (recalculated based on [70]).

$$
\begin{aligned}
A' =& -\frac{1}{32k}\left(9\frac{\Gamma^n_{s0}}{E-E_{s0}+i\Gamma_{s0}/2}+7\frac{\Gamma^n_{s1}}{E-E_{s1}+i\Gamma_{s1}/2}+9\frac{\Gamma^n_{p}}{E-E_{p}+i\Gamma_{p}/2}\right)\\
&+\frac{i}{16}\left(9\frac{\Gamma^n_{s0}}{E-E_{s0}+i\Gamma_{s0}/2}R_{s0}+7\frac{\Gamma^n_{s1}}{E-E_{s1}+i\Gamma_{s1}/2}R_{s1}\right)-\frac{1}{16}\left(9R_{s0}+7R_{s1}\right)+\frac{ik}{16}\left(9R^2_{s0}+7R^2_{s1}\right)\\
B' =& -\frac{1}{32k}\left(7\frac{\Gamma^n_{s0}}{E-E_{s0}+i\Gamma_{s0}/2}-7\frac{\Gamma^n_{s1}}{E-E_{s1}+i\Gamma_{s1}/2}+\frac{\Gamma^n_{p}}{E-E_{p}+i\Gamma_{p}/2}\left(-\frac{39}{4}x_S^2+\frac{9}{2}\sqrt{\frac{7}{5}}x_Sy_S+\frac{63}{20}y_S^2\right)\right)\\
&+\frac{i}{16}\left(7\frac{\Gamma^n_{s0}}{E-E_{s0}+i\Gamma_{s0}/2}R_{s0}-7\frac{\Gamma^n_{s1}}{E-E_{s1}+i\Gamma_{s1}/2}R_{s1}\right)-\frac{7}{16}\left(R_{s0}-R_{s1}\right)+\frac{7ik}{16}\left(R^2_{s0}-R^2_{s1}\right)\\
C' =& \frac{3\sqrt{3}}{32k}\frac{\sqrt{\Gamma^n_{s0}}v\sqrt{\Gamma^n_{p}}}{(E-E_{p}+i\Gamma_{p}/2)(E-E_{s0}+i\Gamma_{s0}/2)}(\sqrt{7}x_S-\sqrt{5}y_S)\\
D' =& \frac{\sqrt{21}}{8k}\frac{x_S\sqrt{\Gamma^n_{s0}}w\sqrt{\Gamma^n_{p}}}{(E-E_{p}+i\Gamma_{p}/2)(E-E_{s0}+i\Gamma_{s0}/2)}\\
H' =& -\frac{3\sqrt{7}}{32k}\frac{\sqrt{\Gamma^n_{s0}}v\sqrt{\Gamma^n_{p}}}{(E-E_{p}+i\Gamma_{p}/2)\,(E-E_{s0}+i\Gamma_{s0}/2)}\left(x_S+\sqrt{35}y_S\right)\\
K' =& -\frac{\sqrt{21}}{128k}\frac{\Gamma^n_{p}}{E-E_{p}+i\Gamma_{p}/2}\left(3\sqrt{\frac{3}{7}}x_S^2-18\sqrt{\frac{3}{5}}x_Sy_S+\frac{11}{5}\sqrt{21}y_S^2\right)\\
E' =& \frac{3\sqrt{21}}{256k}\frac{\Gamma^n_{p}}{E-E_{p}+i\Gamma_{p}/2}\left(5\sqrt{\frac{3}{7}}x_S^2-6\sqrt{\frac{3}{5}}x_Sy_S-\frac{11}{5}\sqrt{21}y_S^2\right)\\
F' =& -\frac{3\sqrt{21}}{32k}\frac{\sqrt{\Gamma^n_{s0}}v\sqrt{\Gamma^n_{p}}}{(E-E_{p}+i\Gamma_{p}/2)\,(E-E_{s0}+i\Gamma_{s0}/2)}\left(x_S+\sqrt{\frac{7}{5}}y_S\right),\\
G' =& \frac{9\sqrt{7}i}{32\sqrt{5}k}\frac{\sqrt{\Gamma^n_{p1}}v^{pp}_T\sqrt{\Gamma^n_{p}}}{(E-E_{p}+i\Gamma_{p}/2)\,(E-E_{p1}+i\Gamma_{p1}/2)}\left(x_Sy_{S1}-x_{S1}y_S\right)\\
B'_3 =& \frac{189}{256k}\frac{\Gamma^n_{p}}{E-E_{p}+i\Gamma_{p}/2}\left(\frac{1}{7}x_S^2+\frac{2}{\sqrt{35}}x_Sy_S+\frac{1}{5}y_S^2\right)
\end{aligned}
\tag{2.70}
$$

Here, the phase shift due to potential scattering is treated in a low-energy limit, and the potential radii of the s_0 and s_1-waves were calculated as R_{s0} and R_{s1} respectively, as follows

$$
\begin{aligned}
&\lim_{k\to0}\frac{\cos2\delta_{s0}}{k}=\lim_{k_n\to0}\frac{\cos\delta_{s0}}{k}=1,\quad \lim_{k\to0}\frac{\sin2\delta_{s0}}{k}=-2R_{s0},\quad \lim_{k\to0}\frac{\sin\delta_{s0}}{k}=-R_{s0}\\
&\lim_{k\to0}\frac{\cos2\delta_{s1}}{k}=\lim_{k_n\to0}\frac{\cos\delta_{s1}}{k}=1,\quad \lim_{k\to0}\frac{\sin2\delta_{s1}}{k}=-2R_{s1},\quad \lim_{k\to0}\frac{\sin\delta_{s1}}{k}=-R_{s1}.
\end{aligned}
\tag{2.71}
$$

where v^{pp}_T in G' represents P-even and T-odd phenomenological interaction, where mixing by p_0 and p_1 waves is the main contribution [73]. Since the phenomenological interaction v^{pp}_T is predicted to be very small and is proportional to the 2nd-rank tensor polarization [74], this argument will henceforth be discussed without mentioning G'. All coefficients are shown in Eq.2.70 but have varying weights and therefore varying importance. We are interested in D', which is P- and T-odd, while the other coefficients are background and suppression factors in the TRIV search. The coefficient of A', corresponding to the spin-independent scattering cross section, however, it affects the target transmission and does not directly affect the TRIV search. The term that introduces the most systematic uncertainty that we should care about is the B' term, which depends on neutron and nuclear spins and causes significant suppression of the search sensitivity due to pseudomagnetism, which will be discussed following section. It is also important to quantitatively evaluate the values of H', K', which are proportional to $(\hat{\boldsymbol{k}}_n \cdot \hat{\boldsymbol{I}})$ due

Table 2.3 Resonance parameters of ^{139}La [1]

K	E_K (eV)	J_K	l_K	Γ_K^γ (meV)	$g_K\Gamma_K^n$ (meV)	R_K (fm)	
0	-38.8 ± 0.4	4	0	60.3 ± 0.5	346 ± 10	6.13 ± 0.10	s_0
1	0.750 ± 0.001	4	1	41.6 ± 0.9	$(3.67 \pm 0.05) \times 10^{-5}$		p
2	72.30 ± 0.01	3	0	64.1 ± 3.0	13.1 ± 0.7	5.54 ± 0.18	s_1

to neutron beam divergence or misalignment, and E', F', and B_3', which are proportional to 2nd or 3rd rank tensor polarization, which is generally considered sufficiently small.

2.6.3 Estimation for the coefficients

In this subsection, we substitute the values of resonance parameters for Eq.2.70 and discuss the magnitude of each coefficient. The calculations were performed by substituting the resonance parameters of ^{139}La shown in Table2.3 and the mixing angles by Eq.2.55 obtained by (n,γ) measurements. The mixing angle was calculated according to Eq.2.37 and substituted as follows

$$\begin{aligned} x_S &= (-1)^9\sqrt{14}\begin{Bmatrix} 1 & \frac{1}{2} & \frac{1}{2} \\ \frac{7}{2} & 4 & 3 \end{Bmatrix} x_F + (-1)^{10}2\sqrt{7}\begin{Bmatrix} 1 & \frac{1}{2} & \frac{3}{2} \\ \frac{7}{2} & 4 & 3 \end{Bmatrix} y_F \\ &= -\frac{1}{2\sqrt{3}}(\sqrt{7}x_F + \sqrt{5}y_F) \\ y_S &= (-1)^9 3\sqrt{2}\begin{Bmatrix} 1 & \frac{1}{2} & \frac{1}{2} \\ \frac{7}{2} & 4 & 4 \end{Bmatrix} x_F + (-1)^{10}6\begin{Bmatrix} 1 & \frac{1}{2} & \frac{3}{2} \\ \frac{7}{2} & 4 & 4 \end{Bmatrix} y_F \\ &= \frac{1}{2\sqrt{3}}(\sqrt{5}x_F - \sqrt{7}y_F). \end{aligned} \tag{2.72}$$

In order to compare only the magnitude of the coefficients, the tensor polarization $P_1 = P_2 = P_3 = 1$ and the unknown parameter $w/v = 1$ in Eq.1.10 were assumed for the calculation. The real part (fm) representing the rotation in the polarized medium and the total cross section (bn) derived from the optical theorem behave around the p-wave resonance as shown in Fig.2.4 and 2.5 respectively. Excluding $\mathrm{Re}A'$, which is included in the measured quantities only as a phase factor, the most influential is $\mathrm{Re}B'$ with a magnitude of about $-2.8\,\mathrm{fm}$, and its contribution is about $\sim 10^3$ larger than the other real parts. Next, we mention Fig.2.5, which is the theoretical curve of the cross section. B', K', and H', which correspond to cross section proportional to vector polarization, we find that B' and K' are comparable in p-wave resonance, and H' is about one-tenth of them. The absorption cross section C' corresponding to the longitudinal asymmetry P_L is $0.3\,\mathrm{bn}$, and D' corresponding to the P- and T-odd cross section is $\kappa(J)$ based on Eq.2.55 and yields $\mathrm{Im}D' = 0.51\mathrm{Im}C'$.

2.6.4 Tensor polarization with BF method

From Eq.2.70, all coefficients except A' and C' are proportional to the tensor polarization of the 1st to 3rd rank. Here are the values of each tensor quantity when the BF method is applied. With the nuclear magnetic moment of ^{139}La as μ_{La}, the Hamiltonian with H_{ext} applied as an external magnetic field can be written as $\mathcal{H} = -\mu_{\mathrm{La}}H_{\mathrm{ext}}$. Let m be the magnetic substate for the nuclear spin I, the corresponding population N_m follows a Boltzmann distribution and can be described as follows

$$\begin{aligned} N_m &= A_{\mathrm{norm}}\exp(m\mathcal{H}/Ik_BT) \\ A_{\mathrm{norm}} &= \frac{1}{\sum_{-I}^{I}\exp(m\mathcal{H}/Ik_BT)} \end{aligned} \tag{2.73}$$

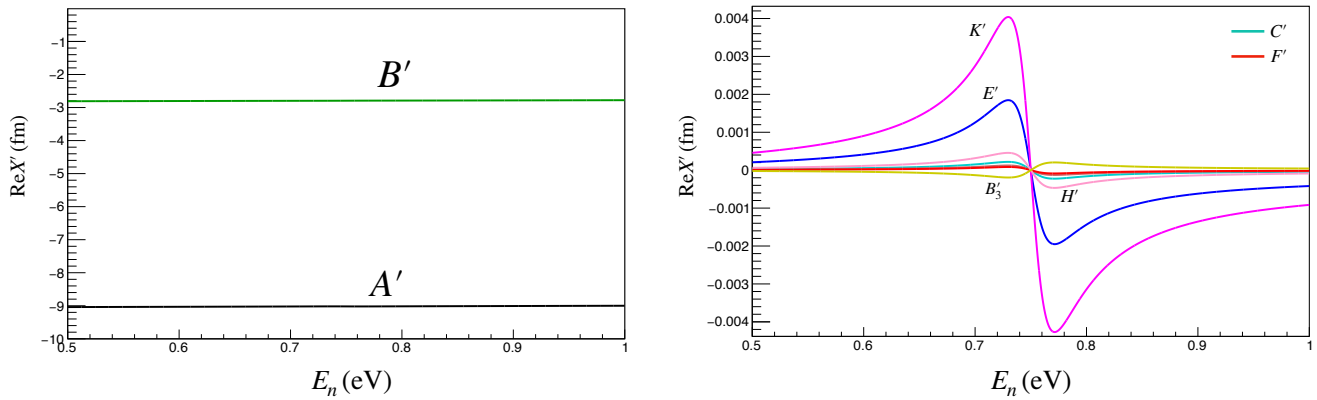

Fig. 2.4 Real part of the coefficients. The left figure shows the dominant coefficients, A' and B', while the right figure shows the other coefficients. The D' is almost the same magnitude as C'.

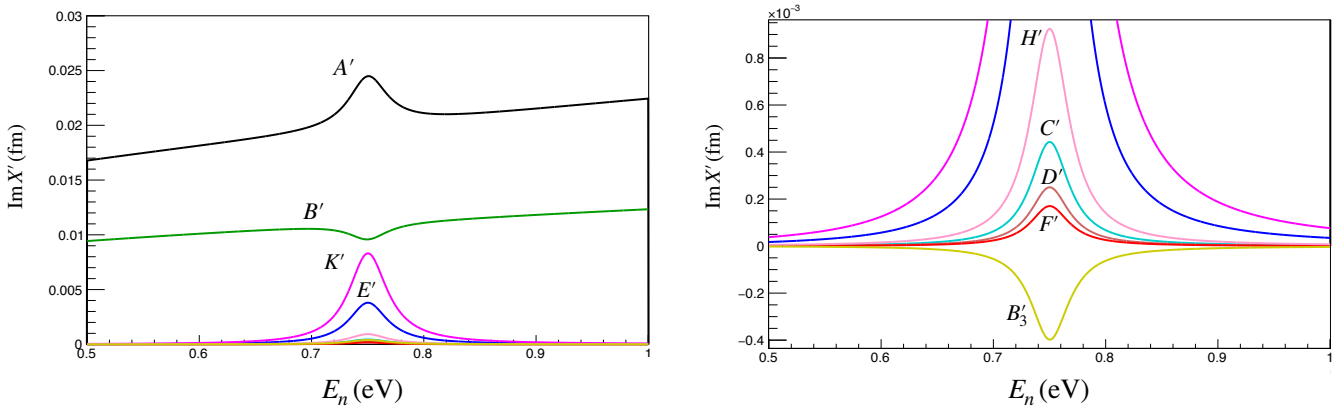

Fig. 2.5 Imaginary part of the coefficients. The left figure shows A', B', K', and E', while the right figure shows the other smaller coefficients.

where $A_{\rm norm}$ is the normalization factor, k_B is Boltzmann's constant, and T is the temperature. In Eq.2.61 and 2.62) based on [70], the expression for $P_q^{7/2}$ was calculated from the spin population for each m as follows

$$
\begin{aligned}
P_1^{\frac{7}{2}} &= N_{\frac{7}{2}} + \frac{5}{7}N_{\frac{5}{2}} + \frac{3}{7}N_{\frac{3}{2}} + \frac{1}{7}N_{\frac{1}{2}} - \frac{1}{7}N_{-\frac{1}{2}} - \frac{3}{7}N_{-\frac{3}{2}} - \frac{5}{7}N_{-\frac{5}{2}} - N_{-\frac{7}{2}} \\
P_2^{\frac{7}{2}} &= N_{\frac{7}{2}} + \frac{1}{7}N_{\frac{5}{2}} - \frac{3}{7}N_{\frac{3}{2}} - \frac{5}{7}N_{\frac{1}{2}} - \frac{5}{7}N_{-\frac{1}{2}} - \frac{3}{7}N_{-\frac{3}{2}} + \frac{1}{7}N_{-\frac{5}{2}} + N_{-\frac{7}{2}} \\
P_3^{\frac{7}{2}} &= N_{\frac{7}{2}} - \frac{5}{7}N_{\frac{5}{2}} - N_{\frac{3}{2}} - \frac{3}{7}N_{\frac{1}{2}} + \frac{3}{7}N_{-\frac{1}{2}} + \frac{3}{7}N_{-\frac{3}{2}} + \frac{5}{7}N_{-\frac{5}{2}} - N_{-\frac{7}{2}}.
\end{aligned}
\tag{2.74}
$$

Based on Eq.2.73, the result of Eq.2.74 is shown in Fig.2.6 with the ratio of external magnetic field and temperature $H_{\rm ext}/T$ on the horizontal axis. $\mu_{\rm La}/\mu_N = +2.7830455(9)$[2] was employed as the nuclear magnetic moment considering the dipole and quadrupole of ^{139}La. For instance, when $H_{\rm ext}/T = 100$, we can calculate $P_1 = 4.4 \times 10^{-2}$, $P_2 = 1.3 \times 10^{-3}$, $P_3 = 2.9 \times 10^{-5}$, especially the tensor polarization of the 3rd-rank is extremely small.

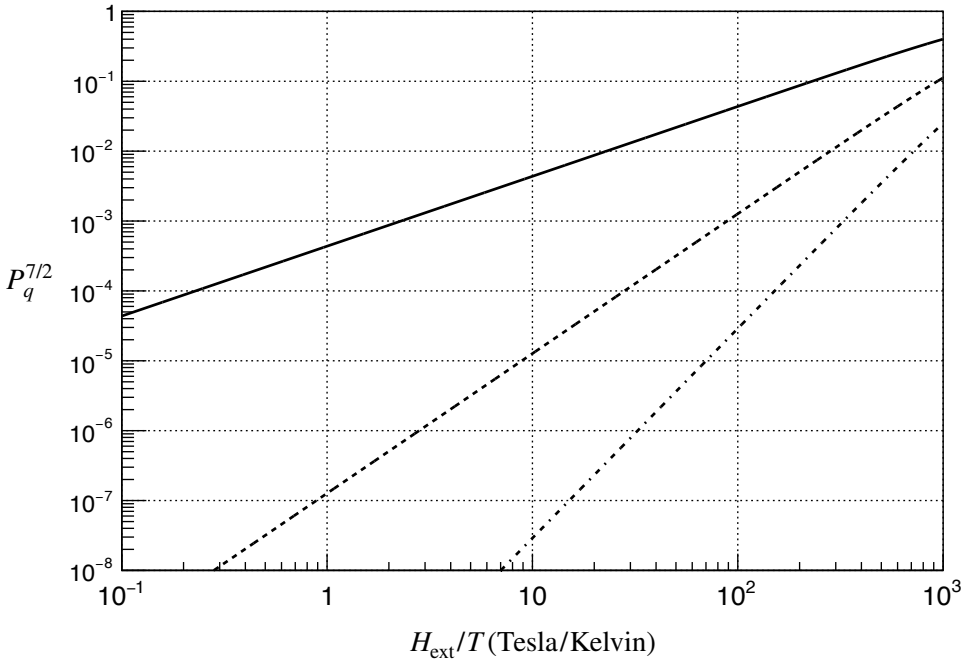

Fig. 2.6 Tensor polarization $P_q^{7/2}$.

The solid, dashed, and dashed-dotted lines correspond to $q = 1, 2, 3$ respectively.

Chapter 3

TRIV in neutron optics

The search for TRIV using neutron optics was first proposed by Kabir in 1982 [49]. Subsequently, Stodolsky, Bunakov, Gudkov, and Kabir discussed the formalism of spin observables, experimental configurations, and systematic uncertainties [50, 75, 76, 77, 78, 79, 80]. Furthermore, Lamoreaux developed detailed evaluation methods for spin observables based on the formulation using the time-evolution operator of neutron spins [81]. Chapter 2 provided a detailed discussion of the interaction between isolated nuclei and neutrons. However, in practical experiments, it is necessary to consider the time evolution of neutron spins propagating through a media with finite thickness, taking into account neutron spin rotation and polarization due to optical activity, as well as the Larmor precession induced by external magnetic fields [34, 35, 82]. In this chapter, the expressions developed by Kabir and Lamoreaux [78, 81] are extended to describe the time evolution of neutron spins when polarized neutrons propagate through a polarized media. The discussion focuses on spin observables in the context of the search for TRIV, including the pseudomagnetism resulting from the correlation term $(\boldsymbol{\sigma}\cdot\hat{\boldsymbol{I}})$, as represented by the coefficients in Eq.2.70.

3.1 Spin observables propagating through a polarized media

The effect of low energy neutrons of wavenumber k_n propagating in a number density ρ media can be expressed using the complex refractive index n as follows since the potential is uniform in the media by application of the first Born approximation[83].

$$n=\sqrt{1-\frac{U_{\mathrm{F}}}{E_n}}\simeq 1+\frac{2\pi}{k_n^2}\rho f \tag{3.1}$$

where U_F is the Fermi pseudopotential and f is the forward scattering amplitude. Typically if $U_F \sim 100\,\mathrm{neV}$ and $E_n \sim 1\,\mathrm{eV}$, then the approximation in Eq.3.1 is sufficient. The forward scattering amplitude f for low-energy neutrons assuming that it has a correlation term similar to that in Eq.2.66 can be written as follows

$$f=\mathcal{A}+\boldsymbol{\sigma}\cdot\hat{\boldsymbol{I}}\mathcal{B}+\boldsymbol{\sigma}\cdot\hat{\boldsymbol{k}}_n\mathcal{C}+\boldsymbol{\sigma}\cdot\hat{\boldsymbol{k}}_n\times\hat{\boldsymbol{I}}\mathcal{D}. \tag{3.2}$$

$\mathcal{A}$ is the spin-independent scattering amplitude, $\mathcal{B}$ is the neutron and nuclear spin-dependent scattering amplitude, and $\mathcal{C}$ is the neutron helicity-dependent scattering amplitude. Since $\mathcal{D}$ is proportional to the scalar triple product $\boldsymbol{\sigma}\cdot\hat{\boldsymbol{k}}_n\times\hat{\boldsymbol{I}}$, the sign reverses with time reversal. From the discussion in Chapter 2.3, $\mathcal{D}$ represents the interaction of TRIV directly without including the final-state interactions. Then, let the nuclear polarization vector be the arbitrary direction (ϑ_I,φ_I), as shown in Fig.3.1, the coordinate system can be defined as follows

$$\hat{\boldsymbol{k}}_n=\begin{pmatrix}0\\0\\1\end{pmatrix},\quad \hat{\boldsymbol{I}}=\begin{pmatrix}\sin\vartheta_I\cos\varphi_I\\ \sin\vartheta_I\sin\varphi_I\\ \cos\vartheta_I\end{pmatrix},\quad \hat{\boldsymbol{k}}_n\times\hat{\boldsymbol{I}}=\begin{pmatrix}-\sin\vartheta_I\sin\varphi_I\\ \sin\vartheta_I\cos\varphi_I\\ 0\end{pmatrix}. \tag{3.3}$$

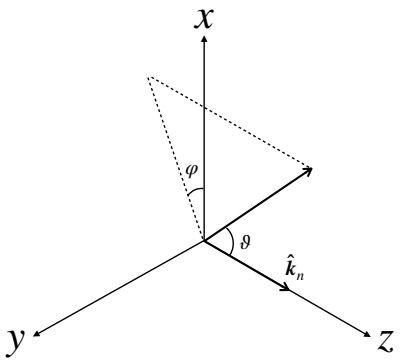

Fig. 3.1 Experimental coordinate system represented by the first angle ϑ and the second angle φ. The neutron momentum direction is fixed to the z-axis.

The effective Hamiltonian represented in the spin space of 2×2 is the sum of the Fermi pseudopotential and the potential due to the external magnetic field $B_{\rm ext}$ ($\| \hat{\boldsymbol{I}}$):

$$H = -\frac{2\pi\hbar^2}{m_n}\rho f - \boldsymbol{\mu}_n \cdot \boldsymbol{B}_{\rm ext} \tag{3.4}$$

This allows us to consider time evolution operators acting on neutron spin states propagating through a polarized media [81]. Here, m_n is the neutron mass, $\mu_n = \frac{g_n}{2}\mu_N$ is the neutron magnetic moment with neutron Landé factor g_n and nuclear magneton μ_N. The external magnetic field is applied uniformly only over the target thickness z, and at the boundary between the polarized media and the vacuum $E_n(\sim 1\,\mathrm{eV}) \gg U_F(\sim 200\,\mathrm{neV})$, then reflection effects can be negligible. The time evolution operator at $(t = z/v_n)$ in the polarized media from Eq.3.4 yields

$$\begin{aligned} U &= e^{-i\frac{H}{\hbar}t} \\ &= \exp\left\{-i\frac{m_n z}{\hbar^2 k_n}\left(-\frac{2\pi\hbar^2}{m_n}\rho f - \boldsymbol{\mu}_n \cdot \boldsymbol{B}_{\mathbf{ext}}\right)\right\} \\ &= \exp\left\{i\frac{2\pi}{k_n}\rho z\left(f + \frac{m_n\mu_n}{2\pi\hbar^2\rho}B_{\rm ext}(\sin\vartheta_I\cos\varphi_I + \sin\vartheta_I\sin\varphi_I + \cos\vartheta_I)\right)\right\} \\ &= \exp\left\{iZ\left(\mathcal{A} + \sigma_x\beta_x + \sigma_y\beta_y + \sigma_z\beta_z\right)\right\}. \end{aligned} \tag{3.5}$$

where $(\sigma_x, \sigma_y, \sigma_z)$ are Pauli matrices, respectively

$$\sigma_x = \begin{pmatrix} 0 & 1 \\ 1 & 0 \end{pmatrix} \quad \sigma_y = \begin{pmatrix} 0 & -i \\ i & 0 \end{pmatrix} \quad \sigma_z = \begin{pmatrix} 1 & 0 \\ 0 & -1 \end{pmatrix} \tag{3.6}$$

Also, v_n is the neutron velocity, $\mu_{\rm eff} = -\frac{m_n\mu_n}{2\pi\hbar^2\rho}$ is the effective magnetic moment in the polarized media, and $Z = \frac{2\pi}{k_n}\rho z$. Now consider the following correspondence

$$\begin{aligned} \boldsymbol{\beta} = \begin{pmatrix} \beta_x \\ \beta_y \\ \beta_z \end{pmatrix} &= Z\begin{pmatrix} (\mathcal{B} - \mu_{\rm eff}B_{\rm ext})\sin\vartheta_I\cos\varphi_I - \mathcal{D}\sin\vartheta_I\sin\varphi_I \\ (\mathcal{B} - \mu_{\rm eff}B_{\rm ext})\sin\vartheta_I\sin\varphi_I + \mathcal{D}\sin\vartheta_I\cos\varphi_I \\ \mathcal{C} + (\mathcal{B} - \mu_{\rm eff}B_{\rm ext})\cos\vartheta_I \end{pmatrix} \\ \alpha &= Z\mathcal{A}, \quad \beta = \sqrt{\boldsymbol{\beta}\cdot\boldsymbol{\beta}} \end{aligned} \tag{3.7}$$

Then, Eq.3.5 can be transformed as

$$\begin{aligned} U &= e^{i\alpha}\left[\cos\beta + i\frac{\sin\beta}{\beta}\boldsymbol{\sigma}\cdot\boldsymbol{\beta}\right] \\ &= \begin{pmatrix} e^{i\alpha}\cos\beta + ie^{i\alpha}\frac{\sin\beta}{\beta}\beta_z & ie^{i\alpha}\frac{\sin\beta}{\beta}\beta_x + ie^{i\alpha}\frac{\sin\beta}{\beta}\beta_y \\ ie^{i\alpha}\frac{\sin\beta}{\beta}\beta_x - ie^{i\alpha}\frac{\sin\beta}{\beta}\beta_y & e^{i\alpha}\cos\beta - ie^{i\alpha}\frac{\sin\beta}{\beta}\beta_z \end{pmatrix}. \end{aligned} \tag{3.8}$$

Here, we introduce

$$\begin{pmatrix} A \\ B \\ C \\ D \end{pmatrix} = e^{i\alpha}\begin{pmatrix} \cos\beta \\ i\frac{\sin\beta}{\beta}\beta_x \\ i\frac{\sin\beta}{\beta}\beta_z \\ i\frac{\sin\beta}{\beta}\beta_y \end{pmatrix}. \tag{3.9}$$

Then, Eq.3.8 can be descrived as

$$U = \begin{pmatrix} A+C & B-iD \\ B+iD & A-C \end{pmatrix} \tag{3.10}$$

Next, we consider the density matrix of the neutron beam operating on the time evolution operator. Let the z axis be the quantization axis, the diagonalized density matrix representing the initial state is

$$\begin{aligned} \hat{\rho}_i &= \frac{1}{2}(\sigma_0 + p_0\sigma_z) \\ &= \frac{1}{2}\begin{pmatrix} 1+p_0 & 0 \\ 0 & 1-p_0 \end{pmatrix} \end{aligned} \tag{3.11}$$

where σ_0 is the unit matrix and $p_0 \geq 0$ is the polarization of the incident neutron beam. The density matrix is normalized by the incident neutron beam intensity. Arbitrary rotation operations on the diagonal basis matrix expressed in Eq.3.11 must be applied to evaluate a polarizer (analyzer) before and after the polarized media, intentional quantization axis changes, and neutron spin misalignment. Then, the unitary matrix representing the rotation operation can be expressed as follows

$$R = \begin{pmatrix} \cos\left(\frac{\vartheta_\sigma}{2}\right) & -\sin\left(\frac{\vartheta_\sigma}{2}\right)e^{-i\varphi_\sigma} \\ \sin\left(\frac{\vartheta_\sigma}{2}\right)e^{i\varphi_\sigma} & \cos\left(\frac{\vartheta_\sigma}{2}\right) \end{pmatrix}. \tag{3.12}$$

By including the polar angle ϑ_σ and azimuthal angle φ_σ expressed in spherical coordinates according to Fig.3.1, we obtain

$$\begin{aligned} \hat{\rho} &= R\hat{\rho}_i R^\dagger \\ &= \frac{1}{2}\begin{pmatrix} 1+p_z & p_x - ip_y \\ p_x + ip_y & 1-p_z \end{pmatrix} \end{aligned} \tag{3.13}$$

$$p_x = p_0\sin\vartheta_\sigma\cos\varphi_\sigma, \quad p_y = p_0\sin\vartheta_\sigma\sin\varphi_\sigma, \quad p_z = p_0\cos\vartheta_\sigma. \tag{3.14}$$

3.1.1 Analyzing power and Polarizing power

Let $\hat{\rho}^p$ denote the density matrix of the neutron beam polarized by the polarizer installed upstream of the polarizing media, and let N_+^a, N_-^a denote the number of transmitted neutrons after upstream $(+)$ or downstream $(-)$ polarization through the polarized media, respectively, and Eq.3.10 and 3.13 can be described as

$$N_+^a = \mathrm{Tr}(U\hat{\rho}_+^p U^\dagger), \quad N_-^a = \mathrm{Tr}(U\hat{\rho}_-^p U^\dagger) \tag{3.15}$$

Here, the superscript p denotes the polarizer. The expected number of neutrons for each is

$$\begin{aligned} N_+^a &= \mathrm{Tr}(U\hat{\rho}_+^p U^\dagger) \\ &= |A|^2 + |B|^2 + |C|^2 + |D|^2 + 2p_x^p\left[\mathrm{Re}A^*B + \mathrm{Im}C^*D\right] + 2p_y^p\left[\mathrm{Re}A^*D + \mathrm{Im}B^*C\right] + 2p_z^p\left[\mathrm{Re}A^*C + \mathrm{Im}D^*B\right] \\ N_-^a &= \mathrm{Tr}(U\hat{\rho}_-^p U^\dagger) \\ &= |A|^2 + |B|^2 + |C|^2 + |D|^2 - 2p_x^p\left[\mathrm{Re}A^*B + \mathrm{Im}C^*D\right] - 2p_y^p\left[\mathrm{Re}A^*D + \mathrm{Im}B^*C\right] - 2p_z^p\left[\mathrm{Re}A^*C + \mathrm{Im}D^*B\right]. \end{aligned} \tag{3.16}$$

Thus, the observed asymmetry (analyzing power of the polarization media) A_{pow} can be described as

$$\begin{aligned} A_{\mathrm{pow}} &= \frac{N_+^a - N_-^a}{N_+^a + N_-^a} \\ &= \frac{\mathrm{Tr}(U\hat{\rho}_+^p U^\dagger) - \mathrm{Tr}(U\hat{\rho}_-^p U^\dagger)}{\mathrm{Tr}(U\hat{\rho}_+^p U^\dagger) + \mathrm{Tr}(U\hat{\rho}_-^p U^\dagger)} \\ &= \frac{2p_x^p\left[\mathrm{Re}A^*B + \mathrm{Im}C^*D\right] + 2p_y^p\left[\mathrm{Re}A^*D + \mathrm{Im}B^*C\right] + 2p_z^p\left[\mathrm{Re}A^*C + \mathrm{Im}D^*B\right]}{|A|^2 + |B|^2 + |C|^2 + |D|^2}. \end{aligned} \tag{3.17}$$

Next, consider an unpolarized beam propagating through a polarized media and observing its polarization (polarizing power of the polarized media) P_{pow}. This corresponds to an experimental system in which the polarizer and the spin transport guide coil are rotated by π about the x axis, then Eq.3.13 is regarded as the density matrix of the analyzer (superscript a). Then, the number of transmitted neutrons N_+^p, N_-^p can be described as

$$\begin{aligned} N_+^p &= \mathrm{Tr}(\hat{\rho}_+^a U U^\dagger) \\ &= |A|^2 + |B|^2 + |C|^2 + |D|^2 + 2p_x^a\left[\mathrm{Re}A^*B - \mathrm{Im}C^*D\right] + 2p_y^a\left[\mathrm{Re}A^*D - \mathrm{Im}B^*C\right] + 2p_z^a\left[\mathrm{Re}A^*C - \mathrm{Im}D^*B\right] \\ N_-^p &= \mathrm{Tr}(\hat{\rho}_-^a U U^\dagger) \\ &= |A|^2 + |B|^2 + |C|^2 + |D|^2 - 2p_x^a\left[\mathrm{Re}A^*B - \mathrm{Im}C^*D\right] - 2p_y^a\left[\mathrm{Re}A^*D - \mathrm{Im}B^*C\right] - 2p_z^a\left[\mathrm{Re}A^*C - \mathrm{Im}D^*B\right]. \end{aligned} \tag{3.18}$$

Calculating as same as Eq.3.17 to obtain

$$\begin{aligned} P_{\mathrm{pow}} &= \frac{N_+^p - N_-^p}{N_+^p + N_-^p} \\ &= \frac{\mathrm{Tr}(\hat{\rho}_+^a U U^\dagger) - \mathrm{Tr}(\hat{\rho}_-^a U U^\dagger)}{\mathrm{Tr}(\hat{\rho}_+^a U U^\dagger) + \mathrm{Tr}(\hat{\rho}_-^a U U^\dagger)} \\ &= \frac{2p_x^a\left[\mathrm{Re}A^*B - \mathrm{Im}C^*D\right] + 2p_y^a\left[\mathrm{Re}A^*D - \mathrm{Im}B^*C\right] + 2p_z^a\left[\mathrm{Re}A^*C - \mathrm{Im}D^*B\right]}{|A|^2 + |B|^2 + |C|^2 + |D|^2} \end{aligned} \tag{3.19}$$

where the neutron spins in the polarizer (p) and analyzer (a) correspond to the following, respectively

$$\boldsymbol{p}^p = p_0^p \begin{pmatrix} \sin\vartheta_\sigma^p \cos\varphi_\sigma^p \\ \sin\vartheta_\sigma^p \sin\varphi_\sigma^p \\ \cos\vartheta_\sigma^p \end{pmatrix}, \quad \boldsymbol{p}^a = p_0^a \begin{pmatrix} \sin\vartheta_\sigma^a \cos\varphi_\sigma^a \\ \sin\vartheta_\sigma^a \sin\varphi_\sigma^a \\ \cos\vartheta_\sigma^a \end{pmatrix}. \tag{3.20}$$

As Eq.3.17 and 3.19 show, the denominator of the asymmetry is the total cross section. In addition, since the analyzing and polarizing power are equivalent as long as the time reversal is not violated, the combination $\mathrm{Re}A^*D$ that maximizes the sensitivity to the D term (proportional to $\mathcal{D}$) can be evaluated by comparing both. Here, the

first- and second-order neutron spin transformation inside the polarized media contained in Eq.3.17 and 3.19 can be specifically expanded from Eq.3.9 as

$$\begin{aligned} A^* X_i &= \frac{e^{-2\mathrm{Im}\alpha}}{2|\beta|^2}\left(i\sin(2\mathrm{Re}\beta) - \sinh(2\mathrm{Im}\beta)\right)\beta^*\beta_i \\ X_i^* X_j &= \frac{e^{-2\mathrm{Im}\alpha}}{2|\beta|^2}\left(-\cos(2\mathrm{Re}\beta) + \cosh(2\mathrm{Im}\beta)\right)\beta_i^*\beta_j \end{aligned} \tag{3.21}$$

where i and j correspond to $(1,2,3) = (x,y,z)$ and $(X_1, X_2, X_3) = (B, D, C)$. An exponential factor is $e^{-2\mathrm{Im}\alpha} = e^{-\frac{4\pi}{k_n}\rho z \mathrm{Im}\mathcal{A}}$, which indicates neutron beam attenuation due to the total cross section. For the denominator, it can be expanded as follows

$$\begin{aligned} |A|^2 + |B|^2 + |C|^2 + |D|^2 &= \frac{e^{-2\mathrm{Im}\alpha}}{2}\left(|\cos\beta|^2 + \left|\frac{\sin\beta}{\beta}\right|^2 \sum_i |\beta_i|^2\right) \\ &= \frac{e^{-2\mathrm{Im}\alpha}}{2}\left(\cos(2\mathrm{Re}\beta) + \cosh(2\mathrm{Im}\beta) + \frac{-\cos(2\mathrm{Re}\beta) + \cosh(2\mathrm{Im}\beta)}{|\beta|^2}\sum_i |\beta_i|^2\right) \end{aligned} \tag{3.22}$$

The β included in the spin observable as a common term greatly contributes to the pseudomagnetism described later in the chapter 3.2. In general, for $\mathrm{Im}\beta \sim 10^{-3}\,\mathrm{fm}$, $\mu_{\mathrm{eff}} B_{\mathrm{ext}} \sim 10\,\mathrm{fm}$, we can approximate $|\sin\beta/\beta| \sim 1$ by applying external magnetic field to make $\mathrm{Re}\beta$ smaller. In this case, Eq.3.22 can be approximated as

$$|A|^2 + |B|^2 + |C|^2 + |D|^2 \sim |A|^2 + |X_i|^2 = e^{-2\mathrm{Im}\alpha}\cosh(2\mathrm{Im}\beta_i). \tag{3.23}$$

In addition, consider the case where the neutron momentum vector and nuclear spin are orthogonal and the analyzing power (polarizing power) for each axis is observed. A second spin transformation term inside a polarized media, $\mathrm{Im}X_i^* X_j$ contained in Eq.3.17 and 3.19, can be considered small compared to $\mathrm{Re}A^* X_i$ and can be described as follows

$$\begin{aligned} A^i_{\mathrm{pow}} &= 2p_0^p \frac{\mathrm{Re}A^* X_i + \mathrm{Im}X_i^* X_j}{|A|^2 + |B|^2 + |C|^2 + |D|^2} \\ &\approx 2p_0^p \frac{\mathrm{Re}A^* X_i}{|A|^2 + |B|^2 + |C|^2 + |D|^2}. \end{aligned} \tag{3.24}$$

Thus, by using Eq.3.21 and 3.23, Eq.3.24 can be approximated as

$$\begin{aligned} \frac{A^i_{\mathrm{pow}}}{p_0^p} = \frac{P^i_{\mathrm{pow}}}{p_0^a} &\approx -\frac{\sinh(2\mathrm{Im}\beta_i)}{\cosh(2\mathrm{Im}\beta_i)} \\ &= -\tanh(2\mathrm{Im}\beta_i) \\ &\approx -2\mathrm{Im}\beta_i. \end{aligned} \tag{3.25}$$

3.1.2 Polarization transfer coefficients

In the section 3.1.1, we assumed a measurement using either a polarizer or an analyzer. In this section, we discuss neutron spin observables when both polarizer and analyzer are installed in the experimental system. Let $\hat{\rho}_{\pm}^{a(p)}$ denote the density matrix upstream ($p_0^{p(a)} = +1$) and downstream ($p_0^{p(a)} = -1$) of neutron spins for Eq.3.20, the corresponding transmission of the expected value N_{ap} can be calculated from

$$\begin{aligned} N_{++} &= \mathrm{Tr}(\rho_+^a U \rho_+^p U^\dagger), \quad N_{-+} = \mathrm{Tr}(\rho_-^a U \rho_+^p U^\dagger) \\ N_{+-} &= \mathrm{Tr}(\rho_+^a U \rho_-^p U^\dagger), \quad N_{--} = \mathrm{Tr}(\rho_-^a U \rho_-^p U^\dagger). \end{aligned} \tag{3.26}$$

The corresponding equation to the asymmetry K_a^p, can be expressed as follows [79]

$$K_p^a = \frac{N_{++} - N_{-+} - N_{+-} + N_{--}}{N_{++} + N_{-+} + N_{+-} + N_{--}} \tag{3.27}$$

Thus, a combination of four different measurements yields the polarization transfer coefficients. Choosing one of $\vartheta_{\sigma^{p(a)}} = 0,\ \pi/2,\ \pi,\ \varphi_{\sigma^{p(a)}} = 0,\ \pi/2,\ \pi,\ 3\pi/2,\ 2\pi$, that is, for neutron spins completely along the (x, y, z) axis, Eq.3.27 can be calculated as

$$K_m^n = p_0^a p_0^p \frac{\left(|A|^2 - \sum_i |X_i|^2\right)\delta_{nm} + 2\sum_i \epsilon_{nmi}\mathrm{Im}A^* X_i + 2\mathrm{Re}X_m^* X_n}{|A|^2 + \sum_i |X_i|^2} \tag{3.28}$$

where $(a, p) = (n, m)$ and $i, m, n = (1, 2, 3) = (x, y, z)$, $(X_1, X_2, X_3) = (B, D, C)$. ϵ_{nmi} denotes Eddington's Epsilon. Calculating for $n = m$ and $n \neq m$, respectively, yields

$$\begin{aligned} K_m^n(m = n) &= p_0^a p_0^p \frac{\left(|A|^2 - |B|^2 - |C|^2 - |D|^2\right) + 2|X_m|^2}{|A|^2 + |B|^2 + |C|^2 + |D|^2} \\ K_m^n(m \neq n) &= 2p_0^a p_0^p \frac{\mathrm{Re}X_m^* X_n + \sum_i \epsilon_{nmi}\mathrm{Im}A^* X_i}{|A|^2 + |B|^2 + |C|^2 + |D|^2}. \end{aligned} \tag{3.29}$$

3.2 Pseudomagnetism

Neutron spin rotation correlated with the inner product $(\boldsymbol{\sigma} \cdot \hat{\boldsymbol{I}})$ of neutron magnetic moment and nuclear magnetic moment is called pseudomagnetism. This phenomenon was predicted by Baryshevsky et al. in 1964 and was demonstrated by Abragam et al. in 1972 [84, 85]. It was pointed out by Bunakov, Gudkov, and Stodolsky in the 1980s that this pseudomagnetic field greatly suppressed the experimental sensitivity in TRIV search with neutron optics, and a solution was subsequently presented [76]. In this section, we discuss the theoretical aspects of pseudomagnetic fields and their solution methods. Let f_+ and f_- be the forward scattering amplitudes corresponding to neutron spins parallel and antiparallel to nuclear spins, respectively, and their corresponding complex refractive indices n_+ and n_- using the Eq.3.1 and 3.2 can be described as

$$n_+ = 1 + \frac{2\pi\rho}{k_n^2}(\mathcal{A} + \mathcal{B}), \quad n_- = 1 + \frac{2\pi\rho}{k_n^2}(\mathcal{A} - \mathcal{B}). \tag{3.30}$$

Therefore, the difference in refractive index for spin parallel and antiparallel is

$$\Delta n = n_+ - n_- = \frac{4\pi\rho}{k_n^2}\mathcal{B} \tag{3.31}$$

The neutron spin angle is

$$\varphi_{\mathrm{pm}} = k_n \Delta n z. \tag{3.32}$$

Then, the rotation frequency of neutron spins due to the pseudomagnetic field can be described as

$$\omega_p = v_n \frac{d\varphi_{\mathrm{pm}}}{dz} = \frac{4\pi\hbar\rho}{m_n}\mathrm{Re}\mathcal{B} \tag{3.33}$$

Therefore, the pseudomagnetic field can be obtained from Eq.3.33) as [86]

$$B_p = \frac{\hbar\omega_p}{2\mu_n} = \frac{2\pi\hbar^2\rho}{m_n\mu_n}\mathrm{Re}\mathcal{B} \tag{3.34}$$

In other words, in a polarized media, low-energy neutrons feel a pseudomagnetic field B_p parallel to the direction of nuclear polarization and undergo Larmor precession at a frequency ω_p. To simplify the coordinate system, let the nuclear spin direction be $\vartheta_I = 2/\pi$ and $\varphi_I = 0$, where $\hat{\boldsymbol{k}}_n \times \hat{\boldsymbol{I}}$ is parallel to the y axis. Since $\mathcal{D}$ is a projection onto the component with respect to the y axis, the torque around the x-axis leads to a significant suppression in

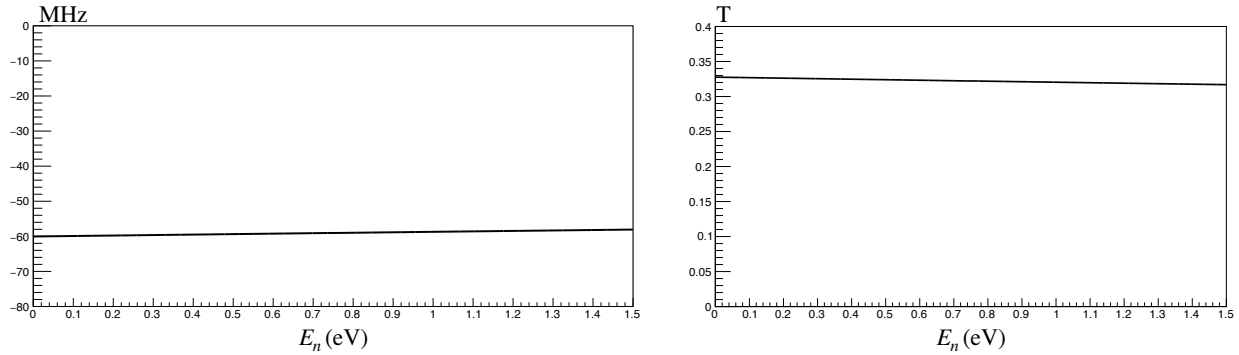

Fig. 3.2 Pseudomagnetism for fully polarized $^{139}\mathrm{La}$.

The left and right figures indicate the neutron energy dependency of the pseudomagnetism frequency and field respectively.

experimental sensitivity in the TRIV search. The most dominant suppression factor is $\mathrm{Re}B'$, which correlates to $(\boldsymbol{\sigma}\cdot\hat{\boldsymbol{I}})$ as shown in Fig.2.4, causing neutron spin rotation of frequency ω_p around the x axis.

Applying the above argument to the $^{139}\mathrm{La}$ polarized target of purity 100%, when the perfect experimental position alignment $(\hat{\boldsymbol{k}}_n\cdot\hat{\boldsymbol{I}})=0$ is achieved in Eq.2.66, it can be assumed that P_3 is very small based on Fig.2.6, then $\mathcal{B}=P_1B'$ is acceptable. Using $^{139}\mathrm{La}$ number density $\rho_{\mathrm{La}}=2.67\times10^{22}\,/\mathrm{cm}^3$ and Table2.3, Eq.3.33 and 3.34 can be expressed as Fig.3.2. In this case, the vector polarization $P_1=1$ is assumed.

In the vicinity of p-wave resonance, this result can be interpreted as neutron spins feel a pseudomagnetic field of $B_p=0.322\,\mathrm{T}$ and rotate with $\omega_p=-59.0\,\mathrm{MHz}$. Therefore, we can improve the experimental sensitivity for TRIV by applying an external magnetic field in the opposite direction, $B_{\mathrm{ext}}=-0.322\,\mathrm{T}$, to cancel the effect of the pseudomagnetic field. This operation corresponds to an approximation to $\sin\beta/\beta\to1$ in Eq.3.9, which is a matrix element in the time evolution operator of neutron spin.

3.3 Expected TRIV asymmetry

We will discuss the measured quantities by applying $^{139}\mathrm{La}$ of purity 100% to the experimental system defined by Fig.3.1. The forward scattering amplitude defined by Eq.3.2 and 2.70 in the previous section is as follows

$$\begin{aligned}
\mathcal{A}&=A'+P_1H'(\hat{\boldsymbol{k}}_n\cdot\hat{\boldsymbol{I}})+P_2E'\left((\hat{\boldsymbol{k}}_n\cdot\hat{\boldsymbol{I}})^2-\frac{1}{3}\right)\\
\mathcal{B}&=P_1B'+P_2F'(\hat{\boldsymbol{k}}_n\cdot\hat{\boldsymbol{I}})+P_3\frac{B'_3}{3}\left((\hat{\boldsymbol{k}}_n\cdot\hat{\boldsymbol{I}})^2-1\right)\\
\mathcal{C}&=C'+P_1K'(\hat{\boldsymbol{k}}_n\cdot\hat{\boldsymbol{I}})-P_2\frac{F'}{3}+P_3\frac{2B'_3}{3}(\hat{\boldsymbol{k}}_n\cdot\hat{\boldsymbol{I}})\\
\mathcal{D}&=P_1D'.
\end{aligned}\tag{3.35}$$

Choosing $(\vartheta_I,\varphi_I)=(\pi/2,0)$ as the coordinates of nuclear spin, leads to $(\hat{\boldsymbol{k}}_n\cdot\hat{\boldsymbol{I}})=0$ and $P_3=0$ corresponding to neutron beam divergence. Assume the external magnetic field cancels the pseudomagnetic field completely at p-wave. Let A_x,A_y,A_z and P_x,P_y,P_z be the analyzing power (polarizing power) parallel to the x,y,z axes for the neutron spin direction defined by Eq.3.14, the measurement with sensitivity to the D' term can be described from

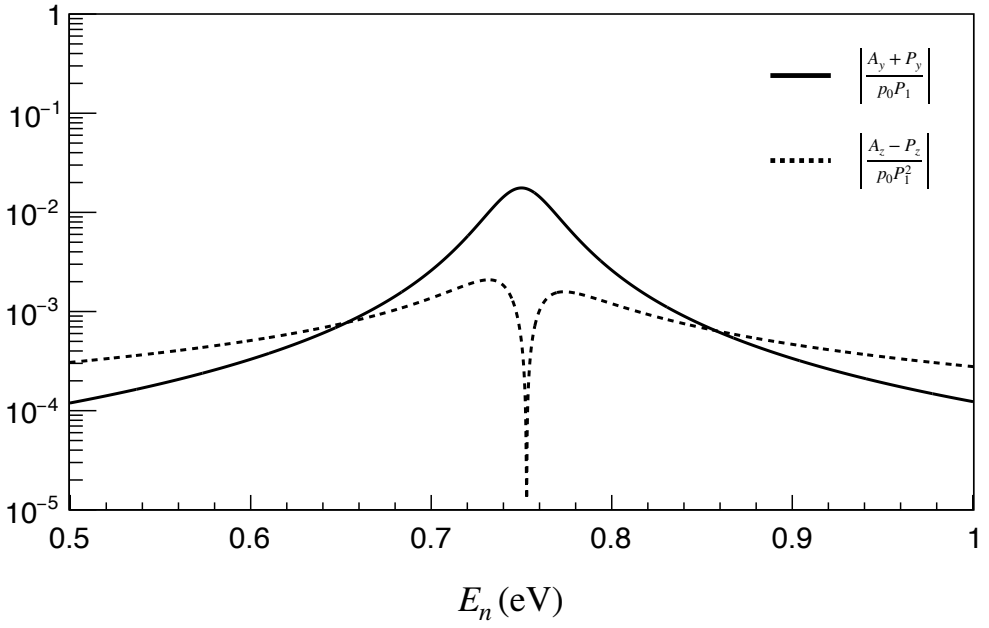

Fig. 3.3 Expected TRIV observables.

Being asumed the P- and T-odd matrix element $w/v = 1$ and $20\,\mathrm{mm}$ target thickness.

Eq.3.17 and 3.19 as follows

$$\begin{aligned}
\frac{A_x}{p_0^p} - \frac{P_x}{p_0^a} &= \frac{4\mathrm{Im}C^*D}{|A|^2+|B|^2+|C|^2+|D|^2} \\
\frac{A_y}{p_0^p} + \frac{P_y}{p_0^a} &= \frac{4\mathrm{Re}A^*D}{|A|^2+|B|^2+|C|^2+|D|^2} \\
\frac{A_z}{p_0^p} - \frac{P_z}{p_0^a} &= \frac{4\mathrm{Im}D^*B}{|A|^2+|B|^2+|C|^2+|D|^2}.
\end{aligned} \tag{3.36}$$

Here, from the functional form of Eq.2.70, $\mathrm{Im}C'^*D'$ is exactly zero. This indicates the condition of $(\hat{\boldsymbol{k}}_n \cdot \hat{\boldsymbol{I}}) = 0$ yields $A_x/p_0^p - P_x/p_0^a$ as completely zero. Therefore, only the combination of $A_y/p_0^p + P_y/p_0^a$ or $A_z/p_0^p - /P_z/p_0^a$ should be considered. Then, normalizing by neutron polarization and vector polarization for the Eq.3.36, the neutron energy dependence in the vicinity of the p-wave resonance can be depicted as Fig.3.3. As an example, we assume a target thickness of $z = 20\,\mathrm{mm}$ and $w/v = 1$. Calculating specific observables with $p_0^p = p_0^a = 1$, $P_1 = 0.5$ for neutron polarization and vector polarization, respectively, we obtain $A_y + P_y = 7.7\times10^{-3}$, $A_z - P_z = 4.8\times10^{-4}$ in the vicinity of p-wave resonance. In other words, since our ultimate goal is a measurement with $A_y + P_y$, which is the most sensitive to the D' term, the experimental system must be orthogonal to the neutron and nuclear spins. Therefore, the control of the pseudomagnetic field is extremely important, and the measurement of the term proportional to $(\boldsymbol{\sigma} \cdot \hat{\boldsymbol{I}})$, is essential in the search for TRIV.

Chapter 4

Experimental setup and results

The B' term, as mentioned in the previous chapter, proportional to $\boldsymbol{\sigma} \cdot \hat{\boldsymbol{I}}$ representing neutron spin and nuclear spin respectively, generates a pseudomagnetic field that can lead to significant background in the search for time-reversal invariance violation (TRIV). Additionally, as indicated in Eq.2.70, B' includes the mixing angle ϕ_F in the scatering amplitude of resonance term in p-wave. Therefore, neutron transmission experiments allow for the measurement of ϕ_F that is independent of the final state. In this chapter, the experimental procedure and results for measuring $\mathrm{Im}B'$, which corresponds to spin-dependent cross-sections in neutron transmission experiments, will be detailed. This includes the use of both polarized neutrons and La metal polarized employing the brute force (BF) method.

4.1 J-PARC MLF

The experiment was conducted at the Japan Proton Accelerator Research Complex (J-PARC), situated in Ibaraki prefecture. This section provides an overview of the proton beam production and neutron transport procedures, with reference to [87]. The proton beam production involves the utilization of a linear accelerator, called LINAC, with a total length of 330 m. The primary function of LINAC is the generation of negative hydrogen ions from hydrogen gas. These negative hydrogen ions are accelerated up to 400 MeV at a frequency of 25 Hz and subsequently injected into a Rapid Cycle Synchrotron (RCS) accelerator, featuring a circumference of 350 m. At the injection point into RCS, the use of carbon foil facilitates the conversion of negative hydrogen ions into a proton beam. The pulsed proton beam is further accelerated to 3 GeV and then transported to the Materials and Life Science Experimental Facility (MLF). In MLF, a 3-GeV pulsed proton beam collides with a liquid mercury target, where a spallation reaction produces a neutron beam which is transported to 23 beam ports as shown in Fig4.1, each with a different physical purpose. To manage the heat generated during these reactions, a 20-ton mercury target is continuously circulated within a stainless steel container. Positioned adjacent to the mercury target is a liquid hydrogen moderator. This moderator is instrumental in reducing the energy of the neutrons generated by spallation reaction through multiple inelastic scattering. The choice of moderator type (coupled, decoupled, or poisoned) is determined based on the specific requirements of each beamline, particularly with regard to neutron intensity and energy resolution. During this experiment, the proton bunch width supplied by RCS was 100 ns (double bunch mode) with an interval of 600 ns, and the average proton beam power was 750 kW.

4.1.1 BL22 RADEN

The experiment was conducted in beamline 22, RADEN, in MLF which is dedicated to energy-resolved neutron imaging. Notably, this beamline offers enough space for the installation of a dilution refrigerator and a superconducting magnet, crucial for achieving nuclear polarization. The beamline configuration, encompassing neutron optical instruments and the length of the beam path is illustrated in Fig. 4.2. The upstream beam size can be selected from three options at a distance of approximately 3 m from the moderator surface using a shutter. Additionally, the neutron beam size and intensity entering the experimental room can be collimated by the first rotary collimator (RC-1) at 8.0 m and the RC-2 at 11.5 m. The optical devices can be adjusted according to the purpose, either to avoid neutron detector counting loss or to suppress gamma-ray background using a filter at 7.0 m. Information on these optical devices is summarized in Table4.1 and 4.2[89].

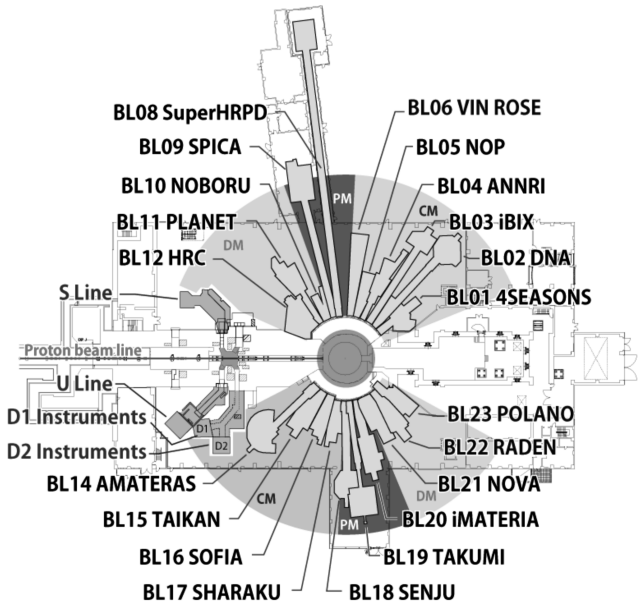

Fig. 4.1 Illustration of 23 beam ports in MLF[87]. The CM, DM, and PM correspond to coupled, decoupled, and poisoned moderators. The proton beam incident from the left side and collides with the liquid mercury target, and then neutrons are transported to each beam port through the moderator.

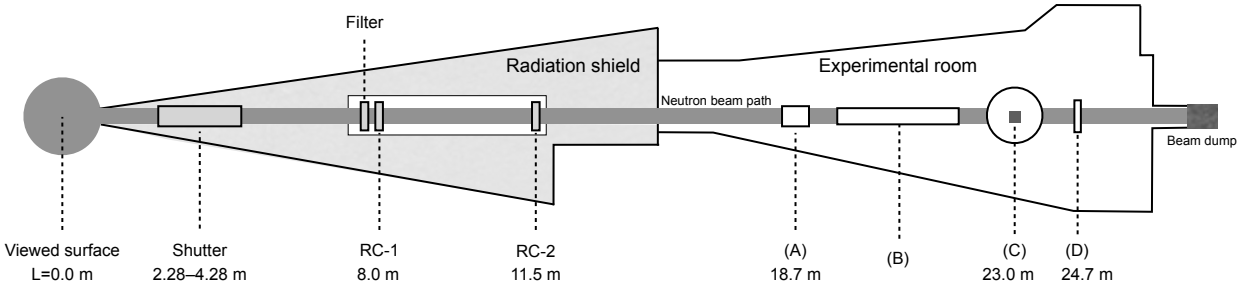

Fig. 4.2 Top view illustration of RADEN configuration[88]. The left circle corresponds to the decoupled moderator surface and each number below is distance from it. The (A),(B),(C), and (D) in the experimental room represent a ^{3}He spin filter to obtain polarized neutrons, a guide magnet coil to transport neutrons adiabatically, a La metal target inside the dilution refrigerator surrounded by a superconducting magnet, and a neutron detector, respectively. These instruments are detailed in the text.

Table 4.1 Options list of beam collimation

	Distance from the surface (m)	Collimator size (mm)
Shutter	$2.28 - 4.28$	$\phi 26.4$, $\phi 50.1$, 100sq
RC-1	8.0	$\phi 2$, $\phi 5$, $\phi 15$, 102sq
RC-2	11.5	$\phi 6$, 43sq, $\phi 100$, $\phi 128$

Table 4.2 Options list of beam filter

Material	Selectable total thickness (mm)
Bi	25, 50, 75, 100
Pb	25, 50, 75
Cd	1
Acrylic resin	5
Borosilicate glass	2

4.2 Experimental apparatus

4.2.1 Neutron polarizer

A $^3\mathrm{He}$ gas spin filter was employed to obtain a polarized neutron beam. $^3\mathrm{He}$ exhibits significantly different absorption cross-sections for neutron spin with up and down. When the polarized $^3\mathrm{He}$ nuclei and neutron spin are parallel, the absorption cross section is almost $0\,\mathrm{bn}$, whereas when they are antiparallel, $10666\,\mathrm{bn}$ at a neutron energy of $25\,\mathrm{meV}$ [90]. The $^3\mathrm{He}$ spin filter was pre-polarized with a spin-exchange optical pumping method (SEOP) [91] before being irradiated by the neutron beam and was installed on the beamline. In the following sections, the $^3\mathrm{He}$ polarization technique and the method for maintaining polarization will be explained.

Polarization of $^3\mathrm{He}$ nuclei with SEOP

In the polarization of $^3\mathrm{He}$ nuclei using the SEOP method, alkali metal electrons are polarized through optical pumping, and the polarization of $^3\mathrm{He}$ nuclei occurs through the Fermi contact hyperfine interaction resulting from collisions between alkali-metal and $^3\mathrm{He}$ nuclei. To optimize the optical pumping efficiency, the glass cell containing $^3\mathrm{He}$ gas is simultaneously filled with adjusted amounts of rubidium and potassium, as reported in [92, 93]. During the SEOP, a linearly polarized fiber laser with a wavelength of 794.7 nm (FWHM: 0.4 nm) and an output power of 110 W is circularly polarized and directed into the entire cell as shown in Fig.4.3. Simultaneously, a static magnetic field of $15\,\mathrm{G}$ is applied parallel to the cell. The laser wavelength corresponds to the excitation from $(5\mathrm{S}_{1/2}, \mathrm{m_J} = -1/2)$ to $(5\mathrm{P}_{1/2}, \mathrm{m_J} = 1/2)$ in Rb atoms (D_1 absorption line). When $^3\mathrm{He}$ interacts with the energy state, the two levels of $5\mathrm{P}_{1/2}$ mix and de-excite with equal probability to $m_\mathrm{J} = -1/2, 1/2$. As the pumping time passes, the population of the $5\mathrm{S}_{1/2}, \mathrm{m_J} = 1/2$ state increases, leading to the polarization of Rb atoms. The enclosed alkali metals are solid at room temperature, and they are heated using a heater to a range of $170\mathrm{C}^\circ$ to $220\mathrm{C}^\circ$, allowing them to vaporize. The vaporized alkali metal atoms, which are polarized through optical pumping, then collide with $^3\mathrm{He}$ nuclei, resulting in the polarization of $^3\mathrm{He}$ nuclei.

4.2.2 AFP-NMR

Our measurement, as described in Eq.3.17, was achieved by taking the asymmetry of the number of transmitted neutrons for neutron spins parallel and anti-parallel to the polarized target. To minimize the systematic uncertainty

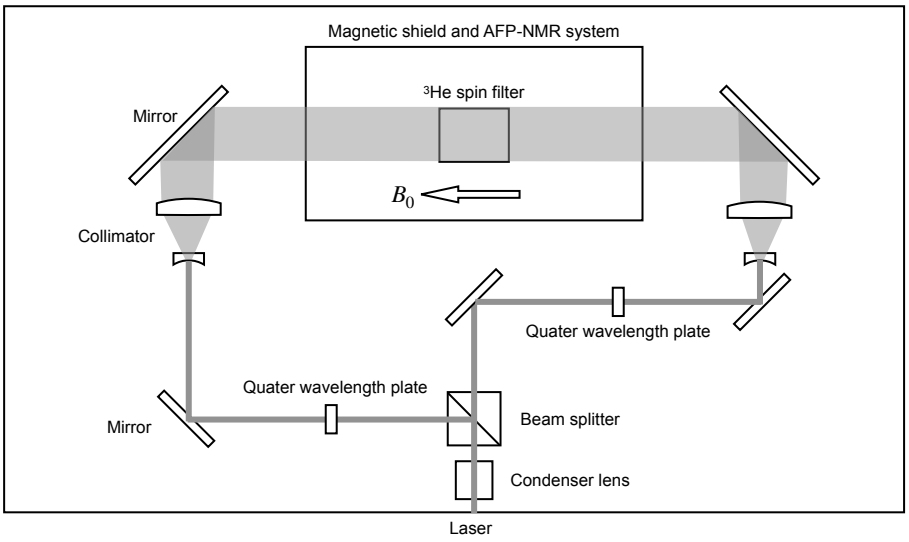

Fig. 4.3 Top view of SEOP system.

in neutron polarization, it is essential to flip the neutron spins multiple times during the measurement since the polarization decreases exponentially with time when laser pumping stops. For this purpose, an adiabatic fast-passage (AFP) NMR technique, as illustrated in Fig.4.4, was employed, allowing fast and loss-minimized spin flipping [94]. AFP-NMR involves rapidly applying RF in a much shorter time than $^3\mathrm{He}$ relaxation time, enabling adiabatic spin-flip and suppressing depolarization. Given that the Larmor frequency for $^3\mathrm{He}$ nuclear spins, with a magnetic gyromagnetic ratio of $|\gamma_{^3\mathrm{He}}| = 32.4\,\mathrm{MHz/T}$, is around 50 kHz with an applied static magnetic field of 15 G, the spin is fliped by sweeping around the frequency over a duration of $0.2\,\mathrm{s}$. The polarization loss due to each spin flip has been confirmed to be sufficiently low at 3.8×10^{-5} /flip [92].

Relaxation of polarized $^3\mathrm{He}$

The polarization of $^3\mathrm{He}$ nuclei developed using the SEOP method can be relaxed by several factors. The polarization $P_{\mathrm{He}}(t)$ at the time t can be described as

$$P_{\mathrm{He}}(t) = P_0 \exp(-t/\tau) \tag{4.1}$$

where P_0 is the initial polarization at the stopping optical pumping, and τ is a polarization relaxation time. The dominant contribution to the relaxation is dipole-dipole interactions between $^3\mathrm{He}$ nuclear spin [95]. This fundamentally limits polarization relaxation in gas, and this effect is unavoidable even under ideal environments. Thus, our attention should be focused on curbing causes of polarization relaxation that are caused by the environment. The most practical point to note is the relaxation limitation due to collisions with the cell wall. Therefore, a boron-free aluminosilicate GE180 glass is used as a $^3\mathrm{He}$ spin filter to avoid the polarization relaxation and attenuation of the neutron beam due to boron with a high absorption cross-section [96]. Another cause of the relaxation is due to static and oscillating magnetic field gradients. This is the reason shown in Fig4.4 that the side and compensation coils are installed inside the B_0 coil and surrounded by a double magnetic shield. Thus, the effective relaxation time is given by

$$\frac{1}{\tau_{\mathrm{eff}}} = \frac{1}{\tau_{\mathrm{dipole}}} + \frac{1}{\tau_{\mathrm{wall}}} + \frac{1}{\tau_{\mathrm{grad}}} \tag{4.2}$$

where τ_{dipole}, τ_{wall}, and τ_{grad} correspond to the relaxation due to dipole-dipole interaction, the collision with the wall, and the gradient of the magnetic field.

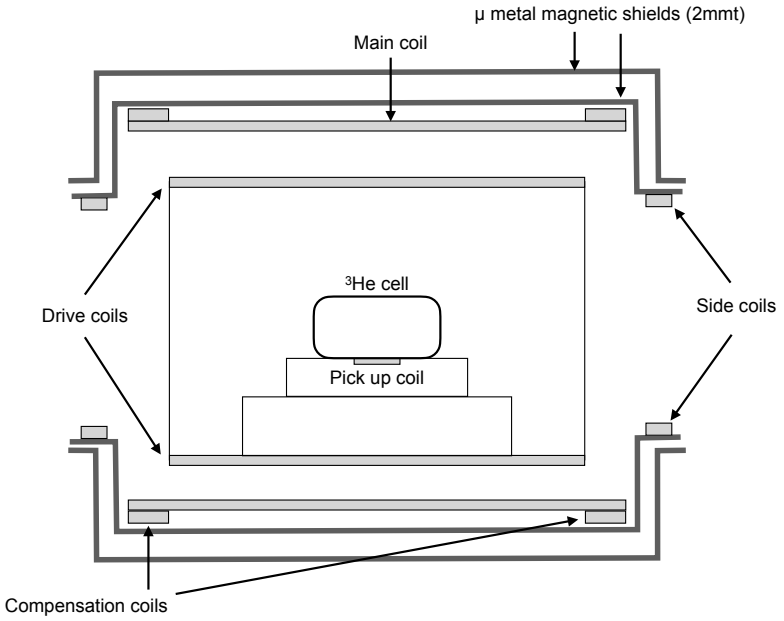

Fig. 4.4 Sectional view of B_0 coil and AFP-NMR system.The $^3\mathrm{He}$ cell is installed inside a double μ-metal magnetic shield to avoid external field disturbances. The magnetic field to hold the nuclear spins is applied by the main coil, and the compensation coils and side coils are to achieve good field uniformity within the cell position.

4.2.3 Nuclear polarized target

A $2.0\,\mathrm{cm}$ cubic lanthanum metal was used as the polarized target. The isotope abundance, nuclear spin and parity I^P, and nuclear magnetic moment μ_0 in the metal La are listed in Tab.4.3. The lanthanum metal target was coated

Table 4.3 Properties of lanthanum metal isotopes[2]. The unit of the nuclear magnetic moment is nuclear magneton.

Isotope	Abundance	I^P	μ_0
$^{139}\mathrm{La}$	99.91%	$7/2^+$	2.78
$^{138}\mathrm{La}$	0.09%	$5/2^+$	3.71

with a thin layer of Apiezon grease to prevent oxidation and reduce thermal contact resistance, then clamped tightly to a copper holder and attached to the cold head of the dilution refrigerator using copper screws. A calibrated ruthenium oxide thermometer was mounted inside the bottom of the cold head to monitor temperature deviation during the experiment. The configuration around the target is shown in Fig.4.5. A dilution refrigerator for low stray field superconducting magnet manufactured by Taiyo Nippon Sanso was employed. The target was mounted and placed in the center of a superconducting magnet manufactured by Scientific Magnetics which was custom-made by Japan Atomic Energy Agency. The target was placed inside the experimental room with the superconducting magnet at 23.0 m from the moderator surface, as shown in (C) of Fig.4.2. The simulation result of the magnetic field distribution when a central magnetic field of 6.8 T was applied is shown in Fig.4.6, considering the nominal configuration of the magnet components. Since the superconducting coils are asymmetric on the upper and lower side, stray magnetic fields in the z-axis direction, which is the beam axis, are also generated as well as in the x-direction. On the other hand, at a distance of more than 2 m, the stray field is below 10 G for all components

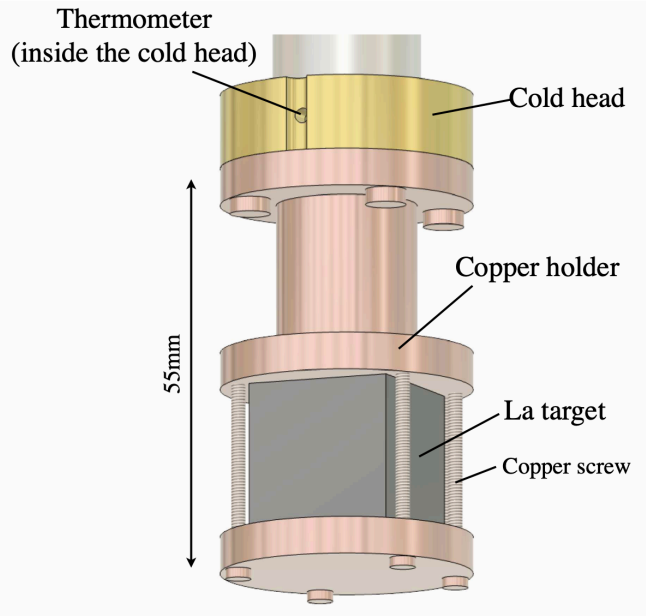

Fig. 4.5 Configuration around the La target.

of the magnetic field. In addition, the magnet is designed not to experience zero-field region along the beam axis, and then the neutron spins incident on the target can be transported without depolarization. The target was constantly cooled by a dilution refrigerator during the experiment, and a high magnetic field was applied to the target perpendicular to the neutron beam axis. The cryogenic and high magnetic field environment (BF method) provides nuclear polarization of the La target following Fig.2.6.

4.2.4 Neutron spin transportation

A polarized neutron beam, obtained by the spin selectivity of a polarized ^{3}He nucleus, is required to tilt its spin (classically the direction of the neutron magnetic moment) along the beam axis to parallel with the target nuclear polarization direction during propagation to a polarized target 4.3 m away from the polarizer. For this purpose, a guide magnet coil of length 3 m, shown in (B) of Fig.4.2, was installed on the neutron path to adiabatically transport neutron spins to the target by the combined magnetic field with the stray field of the superconducting magnet.

Assuming neutron spin $\boldsymbol{\sigma}$, neutron magnetic rotation ratio $\gamma_n (= 1.83 \times 10^8\ /\mathrm{s/T})$, and magnetic field $\boldsymbol{B}$, the equation of motion for spins in a magnetic field can be written as follows

$$\frac{d\boldsymbol{\sigma}}{dt} = \gamma_n \boldsymbol{\sigma} \times \boldsymbol{B} \tag{4.3}$$

This differential equation can be written for each x, y, and z component, and a numerical solution was obtained by the Runge-Kutta method. The gamma factor Γ_{factor}, which represents the adiabatic condition for neutron spin, is expressed as follows

$$\Gamma_{\mathrm{factor}} = \frac{\omega_L}{\omega_B} = \gamma_n \frac{|\boldsymbol{B}|}{v_n (d\theta_B/dz)} \tag{4.4}$$

where, ω_L is the neutron Larmor frequency, ω_B is the rotation frequency in the magnetic field, v_n is the neutron velocity, and $d\theta_B/dz$ is the magnetic field gradiet, and the z axis represents a neutron beam direction. As previously stated, our focus lies in the vicinity of p-wave for ^{139}La, and thus, the calculation was conducted using neutron velocity associated with the p-wave resonance. The guide coil magnetic field was measured using a magnetic probe and was found to be $B_z \sim 20\,\mathrm{G}$ on the beam axis. Considering the magnetic field distribution shown in Fig.4.6 and treating the measured magnetic field of the guide coil as uniform, the calculation for Eq.4.4 was carried out, and it

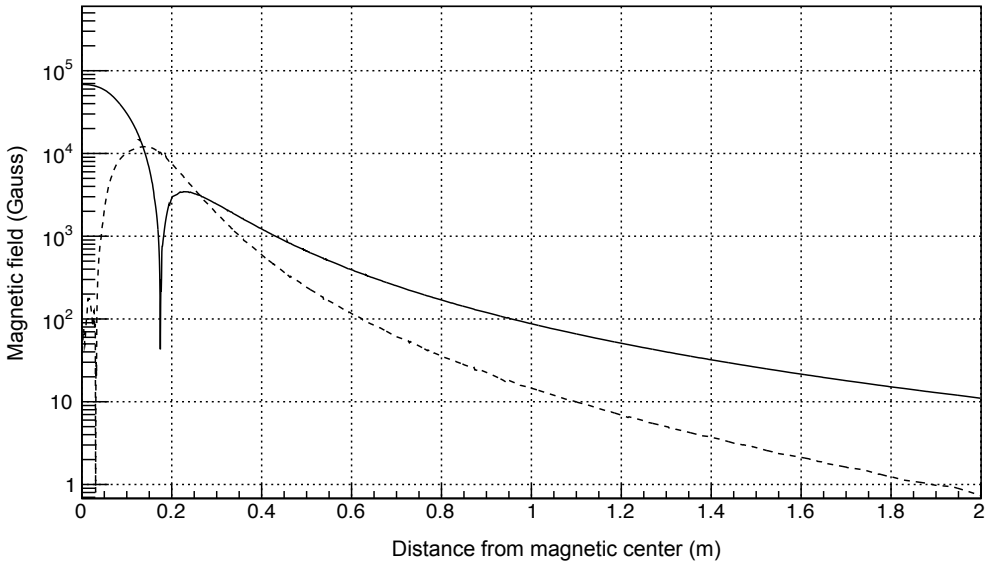

Fig. 4.6 Stray magnetic field in 6.8 T applied.The magnetic field distribution of the superconducting magnet was calculated using FEMTEM, a three-dimensional finite element method magnetic field simulation software provided by Murata software. The solid and dotted lines represent the stray field distribution components corresponding to the x-axis and z-axis directions, respectively. Both are expressed in absolute value, with the x component being negative beyond the vicinity of 0.18 m and the z component being negative beyond the vicinity of the center.

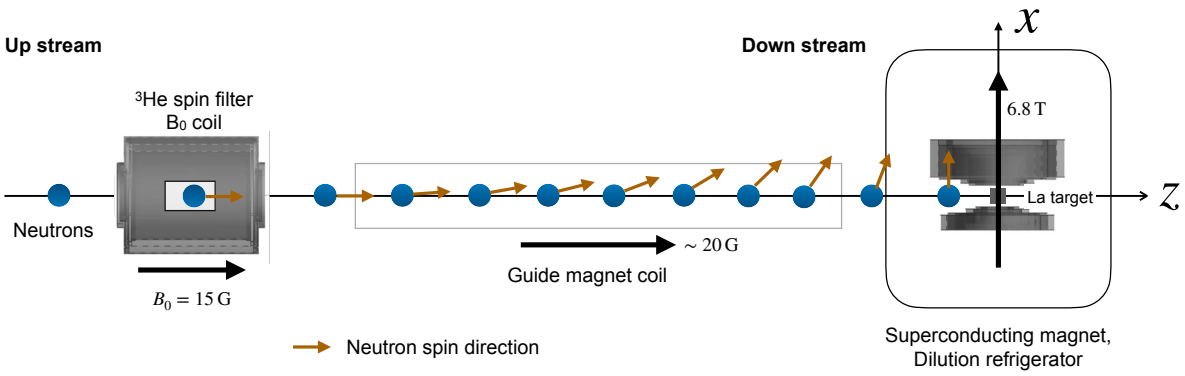

Fig. 4.7 A conceptual diagram that neutron spin propagates through the guide coil.

was found that the adiabatic factor Γ_{factor} exceeded 20 in all regions between the polarizer and the polarized target. Generally, an adiabatic factor of 10 or higher is considered acceptable [97], and this requirement was satisfied by a sufficient margin. Figure 4.7 shows the conceptual diagram that neutron spins obtained by the ^{3}He spin filter as propagating to the La target.

4.2.5 Neutron detector

A ^{6}Li time analyzer (LiTA), 16×16 multi-anode flat panel PMT with a lithium glass scintillator attached to each pixel as a neutron converter, was employed as the neutron detector [98]. The size of each pixel consists of 3 mm

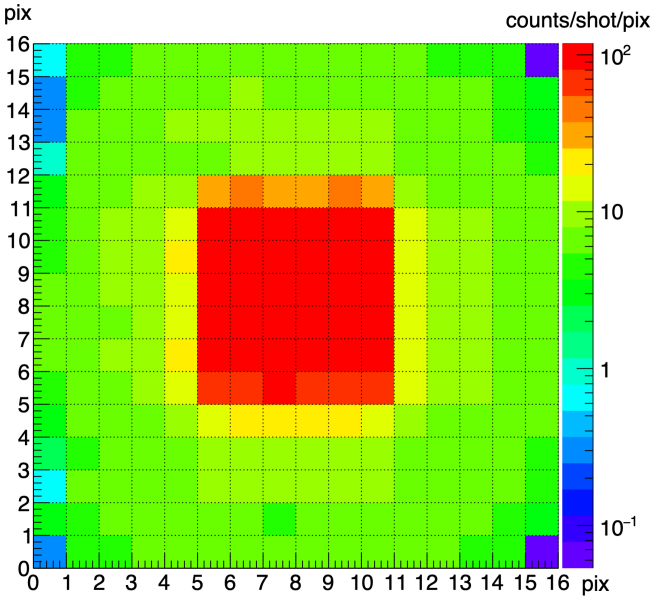

Fig. 4.8 2D neutron position distribution with LiTA. The number of neutron counts per pixel is normalized by the number of shots of the proton beam.

square (position resolution), and a two-dimensional position can be obtained. The neutron energy can be obtained by recording the time of flight (TOF) between the signal of the proton bunch incident from the RCS to the mercury target and the signal of the neutron detection. The number of detected neutrons is recorded in list mode for each pixel, and the TOF is recorded at the same time. The detector position of LiTA from the moderator surface was determined with the nuclear resonance absorption peak to obtain $L_{\mathrm{md}} = 24.713\,\mathrm{m}$. The correspondence between TOF and neutron energy can be obtained as

$$E_n\,(\mathrm{eV}) = 5.227 \times 10^{-3} \frac{L_{\mathrm{md}}\,(\mathrm{m})}{\mathrm{TOF}\,(\mathrm{ms})} \tag{4.5}$$

4.3 Measurement

4.3.1 Determination of neutron optical condition

In addition to the equipment shown in Fig.4.2, stainless steel collimators were installed 0.7 m upstream of the ^{3}He spin filter and 7 cm upstream of the LiTA in the experimental room, respectively. The respective collimator sizes were 3 cm$\times$ 3 cm (spin filter side) and 2 cm$\times$2 cm (LiTA side). The optimal collimation and filtering conditions that can be remotely controlled were searched for by measuring the TOF spectra of the neutron beam with different RC sizes and filter materials to obtain the maximum neutron flux within the detector count rate. The measurements were performed with both the La target and the ^{3}He spin filter installed and a cadmium filter of 1 mm thickness was always inserted to reduce the heat load on the La target. First, the two-dimensional neutron position distribution by LiTA is shown in Fig4.8. The position region near the center of the figure $(6\,\mathrm{pix} \times 6\,\mathrm{pix})$ is collimated and therefore high intensity. The following analysis applies only to this position region since this region is considered to have neutrons passed through the La target. The TOF distribution of detected neutrons for different RC-2 and filter conditions and the ratio to the lowest counting condition is depicted in Fig.4.9 and Fig.4.10, respectively. From these results, we determined the condition of $(\mathrm{RC2}, \mathrm{Pb}, \mathrm{Bi}) = (100, 25, 0)$ because a resonance peak appears around TOF=2.4 ms when Bi filter is used, and to give high neutron intensity while minimizing count loss less than 1% around p-wave region. The neutron optics in the determined beam conditions are represented in Fig.4.11. It can be seen that the maximum neutron beam divergence angle is less than $3\,\mathrm{mrad}$ for this beam path.

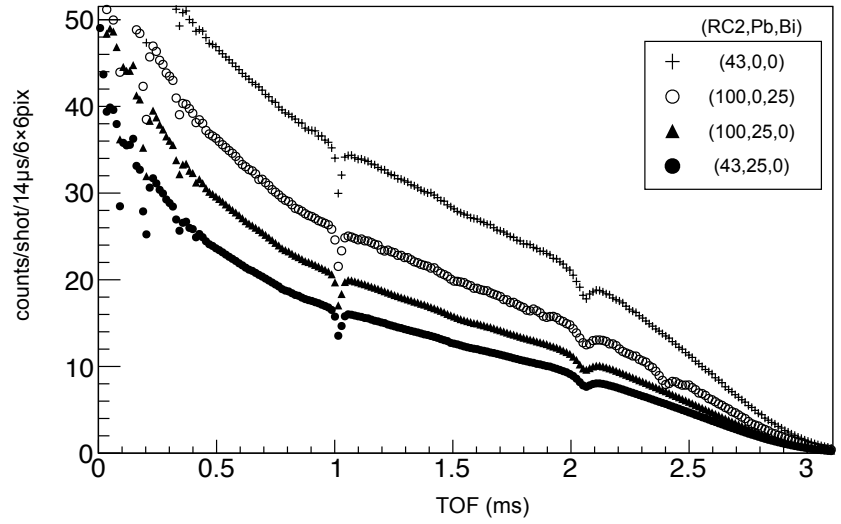

Fig. 4.9 TOF distribution for different collimation and filter conditions. The dip at $2.1\,\mathrm{ms}$ corresponds to a p-wave resonance (our interest) at $0.75\,\mathrm{eV}$. The RC-1 was set to its maximum size of $102\mathrm{sqmm}$, and a cadmium filter stripped neutron energy above $\mathrm{TOF} > 3\mathrm{ms}$, i.e., below $0.3\,\mathrm{eV}$.

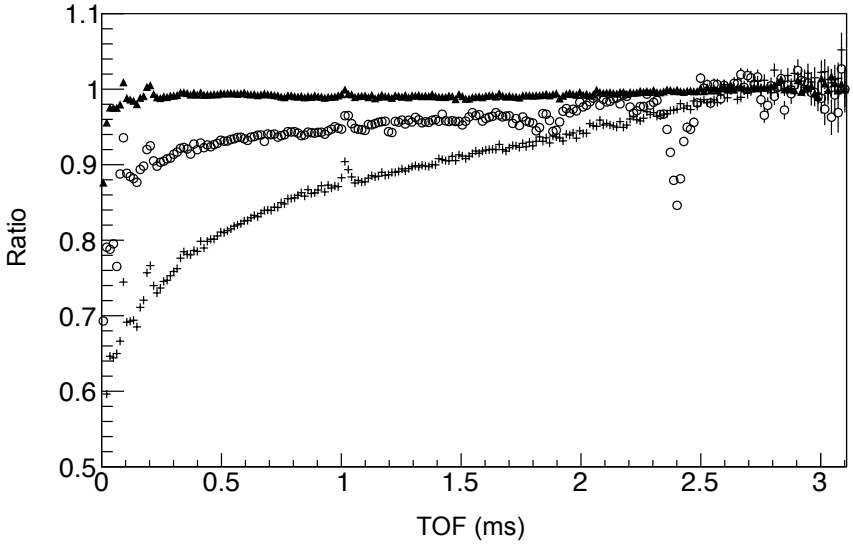

Fig. 4.10 Ratio of counting losses to the condition $(\mathrm{RC2, Pb, Bi}) = (43, 25, 0)$, normalized to 1 for $\mathrm{TOF} = 3.1\mathrm{ms}$, respectively. Each symbol conforms to Fig.4.9.

4.3.2 Asymmetry

The experiment for the asymmetry was performed in the following two conditions: (I) low-temperature condition $(\mathrm{T} = 67\,\mathrm{mK})$ and (II) high-temperature condition $(\mathrm{T} = 1\,\mathrm{K})$. These comparisons exclude spin-dependent asymmetries that are caused by any systematics other than nuclear polarization. The neutron irradiation times were 22 hours and 6 hours, respectively. In condition (I), the temperature increase by the beam irradiation to the La target was approximately 1mK. It indicates that the temperature difference between the cold head and the La target can

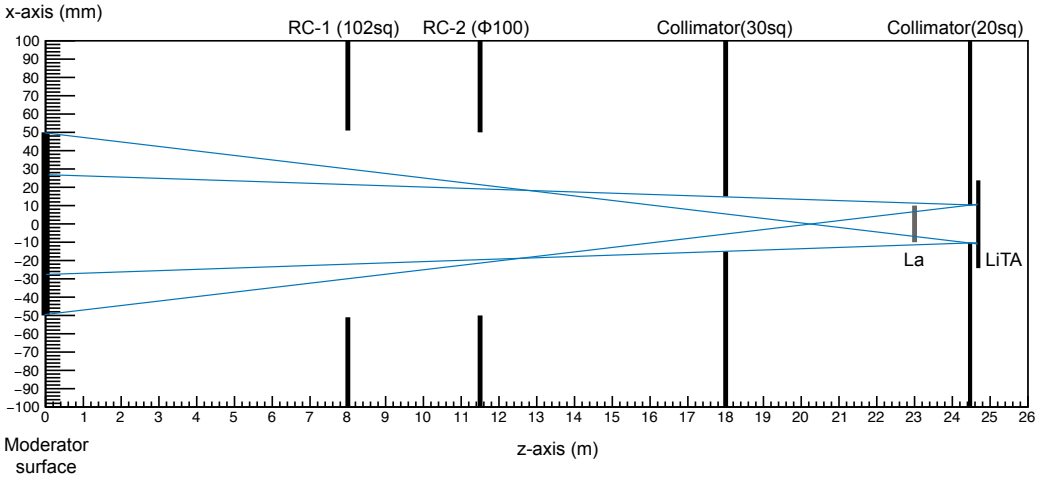

Fig. 4.11 Beam path under optimized beam conditions.The horizontal axis represents the distance(m) from the moderator surface and the vertical axis corresponds to the aperture size(mm) in the x-direction. The solid lines represent the umbra and penumbra, respectively.

be considered negligible. The temperature fluctuation during the measurement was also around 1 mK, which was caused by beam interruptions in the accelerator due to malfunctions. The asymmetry of neutron counts for parallel and anti-parallel spins transmitted through the polarized lanthanum target is defined as

$$A_{\mathrm{pow}} = \frac{N_- - N_+}{N_- + N_+} \tag{4.6}$$

where N_- and N_+ are the neutron counts for parallel and anti-parallel neutron spins. The spin-dependent asymmetry A_{pow} for $(\vartheta_\sigma^p, \varphi_\sigma^p) = (0, \pi/2)$ in Eq.3.17 can be described using Eq.3.25 as

$$A_{\mathrm{pow}} = p_0^p \tanh(2\mathrm{Im}\beta_x) \tag{4.7}$$

where p_0^p, and β_x are the neutron polarizer efficiency and the corresponding $\boldsymbol{\beta}$ in the neutron-nuclear target spin system substituting $(\vartheta_I, \varphi_I) = (\pi/2, 0)$ for Eq.3.7. In this argument, the measurement and analysis were performed using resonance parameters listed in Table 2.3. In the neutron beam condition previously defined in Section 4.3.1, the measurement of the TOF spectra of transmitted neutrons and the corresponding asymmetry A_{pow} for conditions (I) and (Ⅱ) were performed as shown in Fig4.12. In condition (I), corresponding to a few percent of nuclear polarization, a significant asymmetry was observed, while the asymmetry disappeared in condition (Ⅱ) due to lower nuclear polarization. Notably, the peak and dip structures at the 2.99 eV and 0.75 eV resonances were observed. The global structure observed in less than $0.3\,\mathrm{ms}$ can be attributed to the spin-dependent cross-section of the negative s-wave resonance.

Neutron polarization

The ^{3}He spin filter was polarized using SEOP outside the beamline and then installed on the beamline with a B_0 coil depicted in Fig 4.4 to maintain the ^{3}He polarization and decide the quantization axis parallel to the beam direction. The ^{3}He cell was 45 mm in diameter by 70 mm in length and the pressure was 0.31 MPa. The neutron beam, longitudinally polarized by the ^{3}He spin filter, was guided using a guide magnet explained in the previous section. The ^{3}He polarization was determined with the ratio of the transmitted neutrons for polarized and unpolarized ^{3}He spin filter. The ratio of the transmitted neutrons is described as

$$\frac{N_{\mathrm{pol}}}{N_{\mathrm{unpol}}} = \cosh(P_{\mathrm{He}}(t)\rho_{\mathrm{He}}d_{\mathrm{He}}\sigma_{\mathrm{He}}) \tag{4.8}$$

where σ_{He} and $\rho_{\mathrm{He}}d_{\mathrm{He}}$ are the neutron absorption cross section of ^{3}He and areal density of ^{3}He gas, respectively. Here, N_{pol} is defined as $N_- + N_+$ to average the counts of transmitted neutrons with the spin-dependent of the La

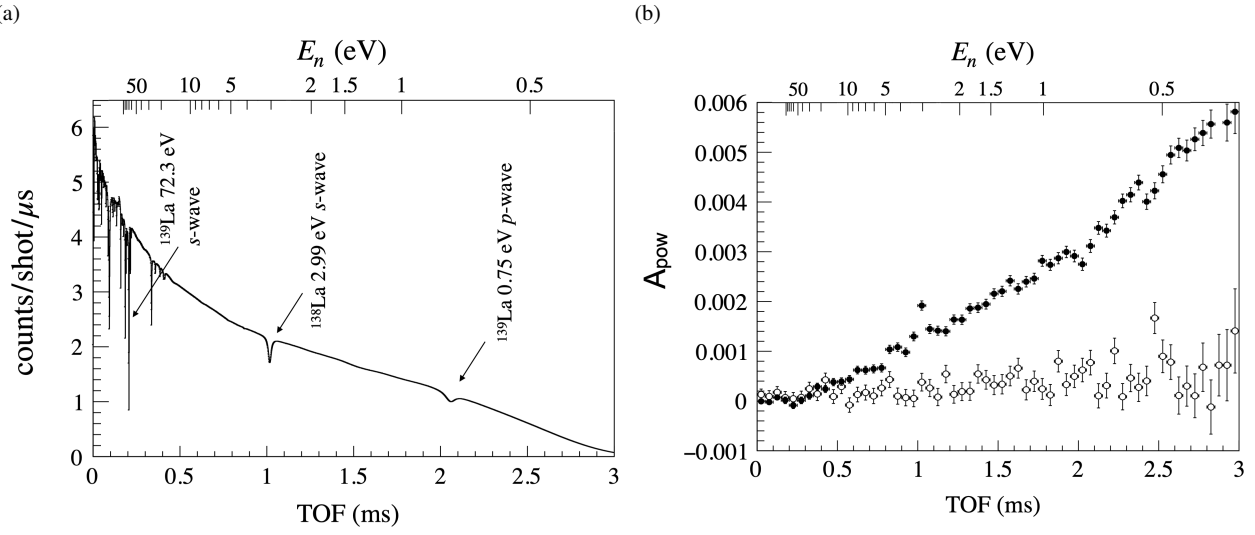

Fig. 4.12 TOF spectra of the transmitted neutrons (a) and the spin-dependent asymmetries (b). Black and white points denote the asymmetries under the conditions (I) and (II), respectively.

Table 4.4 Resonance parameters of ^{138}La [3]

Isotope	E_0 (eV)	J	l	Γ^γ (meV)	$g\Gamma^n$ (meV)
^{138}La	2.99 ± 0.02	$11/2$	0	95 ± 6	0.65 ± 0.03

target. The areal density $\rho_{\rm He} d_{\rm He}$ was measured by the ratio of transmitted neutrons for unpolarized ^{3}He spin filter and empty cell as 21.4 $\mathrm{atm \cdot cm}$. The ^{3}He polarization was obtained for each flip by fitting the TOF dependence of $N_{\rm pol}/N_{\rm unpol}$ using Eq.4.8 with a fit parameter of $P_{\rm He}$ as shown in Fig 4.13. The time dependence of the ^{3}He polarization is depicted in Fig 4.14. The relaxation time of the ^{3}He polarization $\tau_{\rm eff}$as described in Eq.4.2, which was obtained by fitting with Eq.4.1, was 161 hour. The average ^{3}Hepolarization $\bar{P}_{\rm He}$ during the measurement was $(68 \pm 1)\%$. The neutron polarizer efficiency p_0^p is determined as

$$p_0^p(t) = -\tanh(P_{\rm He}(t)\rho_{\rm He} d_{\rm He}\sigma_{\rm He}) \tag{4.9}$$

This equation can be obtained by following the same procedure for a polarized target as written in section 3. A polarization $\bar{p}_0^p$ shown in Fig 4.15 as a function of the neutron energy calculated from the average ^{3}He polarization. The averaged neutron polarization at 0.75 eV during the asymmetry measurement for higher nuclear polarization was $(36.1 \pm 0.5)\%$.

Nuclear polarization

The ^{139}La nuclear polarization was determined using the spin-dependent symmetry at the 2.99 eV s-wave resonance of ^{138}La because the thermometer shows the cold head temperature, not the actual target temperature. The spin-dependent asymmetry at the 2.99 eV resonance, after subtracting the negative s-wave resonance, was obtained as

$$A_{\rm pow} = (5.1 \pm 0.7) \times 10^{-4} \tag{4.10}$$

The spin-dependent cross section of the 2.99 eV resonance of ^{138}La can be theoretically calculated using the resonance parameters listed in Table 4.4 as

$$\sigma_{{\rm S},s}^{\rm theo} = \frac{5\pi}{11k_n^2} \frac{\Gamma_s^n \Gamma_s}{(E - E_s)^2 + (\Gamma_s/2)^2} \tag{4.11}$$

where E_s, Γ_s^n, and Γ_s are the resonance energy, neutron width, and total width of the 2.99 eV s-wave resonance, respectively. The nuclear polarization of ^{138}La can be calculated using Eq.4.7,4.9,4.10, and 4.11, taking into

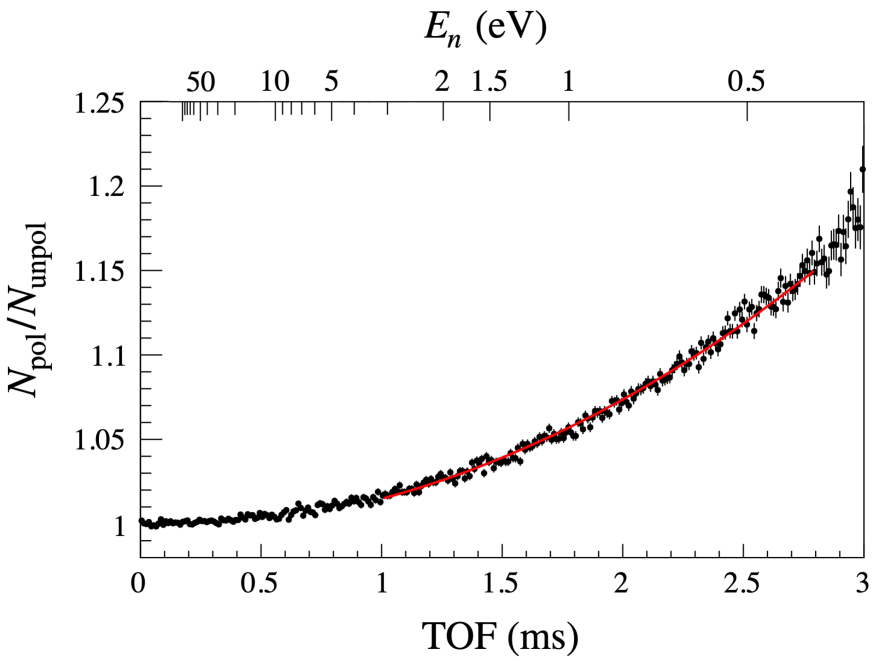

Fig. 4.13 Ratio of the counts of transmitted neutrons for the polarized to the unpolarized ^{3}He spin filter. The curved red line shows the best fit.

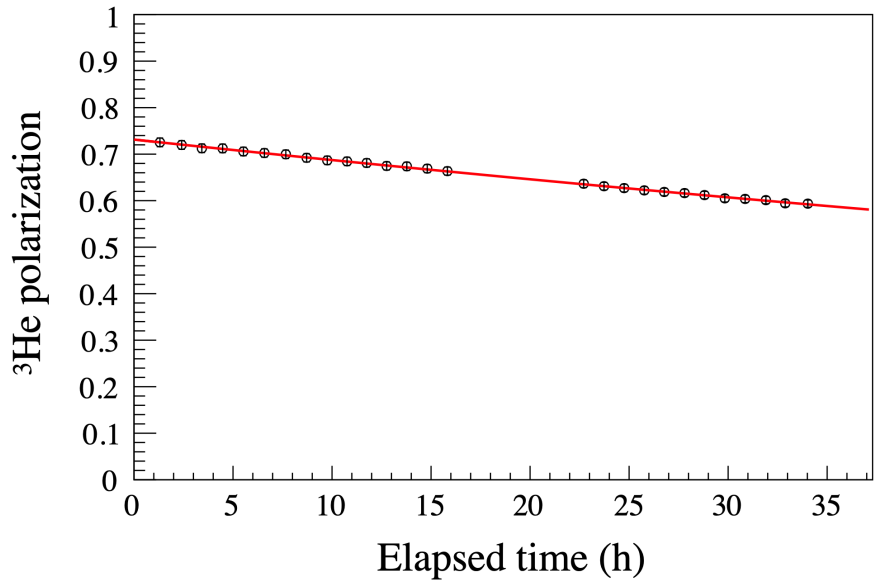

Fig. 4.14 The elapsed time dependence of ^{3}He polarization from the beginning of the asymmetry measurement. The curved line represents the best fit with an exponential function. The measurement was stopped from 16 h to 22 h due to a liquid He transfer for the superconducting magnet.

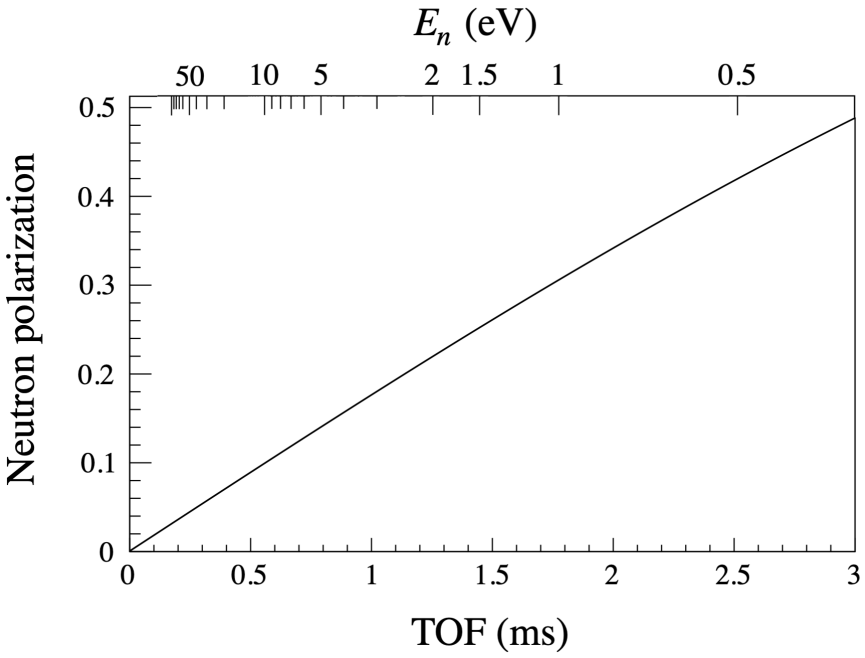

Fig. 4.15 Neutron polarizer efficiency obtained from the averaged ^{3}Hepolarization.

account its natural abundance shown in Table 4.3, yielding a value of $4.9 \pm 0.7\%$. The target temperature $T_{\rm La}$ was calculated based on a Boltzmann distribution and using the magnetic moment and nuclear spin listed in Table 4.3, resulting in $T_{\rm La} = 75.7^{+10.2}_{-8.9}$ mK, which is consistent with the RuO_2 thermometer temperature measured at the cold head of 67 mK. Assuming that the spin temperature of ^{139}La matches that of ^{138}La, the nuclear vector polarization of ^{139}La was calculated to be $P_1 = 3.9 \pm 0.5\%$. Then, the P_2, P_3 representing the target 2nd-rank and 3rd-rank tensor polarization yields $P_2 = 0.1^{+0.03}_{-0.02}\%, P_3 = (2.1 \pm 1.0) \times 10^{-3}\%$, respectively in the present experimental conditions.

4.3.3 Spin-dependent cross section at the p-wave resonance

The experimental spin-dependent cross section value, denoted as $\sigma_{\rm S}^{\rm exp}$, was determined by the asymmetry $A_{\rm pow}$ using Eq.4.7. To extract the K-th resonance component $\sigma_{{\rm S},K}^{\rm exp}$, a fit of the global structure associated with the negative s-wave resonance component using a third-order polynomial function was performed. The regions corresponding to resonances listed in Table 2.3 were excluded from this fitting procedure. The TOF dependence of $P_1\sigma_{\rm S}^{\rm exp}$ and $P_1\sigma_{{\rm S},K}^{\rm exp}$ can be seen in Fig.4.16, which was computed based on the areal density of ^{139}La ($\rho_{\rm La}d_{\rm La} = 0.0534, /{\rm bn}$). A p-value, defined as $p = (1 - {\rm C.L.})/2$, where C.L. represents the confidence level of the non-zero asymmetry, also indicates the significance of $P_1\sigma_{{\rm S},K}^{\rm exp}$ in Fig.4.16. This p-value conveys the likelihood of observing a non-zero value under the assumption of no asymmetry. A confidence level exceeding 99.7% corresponds to a p-value less than 1.35×10^{-3}. Consequently, the spin-dependent cross section was first observed at the p-wave resonance with a confidence level exceeding 99.7%.

The spin-dependent cross section in the vicinity of the p-wave resonance region of $E_p - 3\Gamma_p < E_n < E_p + 3\Gamma_p$ after subtracting the contribution from the negative s-wave component was defined as $\sigma_{{\rm S},K}^{\rm exp}$. It can be obtained using the nuclear vector polarization P_1 as

$$\sigma_{{\rm S},p}^{\rm exp} = -0.26 \pm 0.08\,{\rm bn} \tag{4.12}$$

where E_p and Γ_p are the resonance energy and total width of the p-wave resonance, shown in Table 2.3. The asymmetry of the spin-dependent cross section relative to the spin-independent cross section of the p-wave

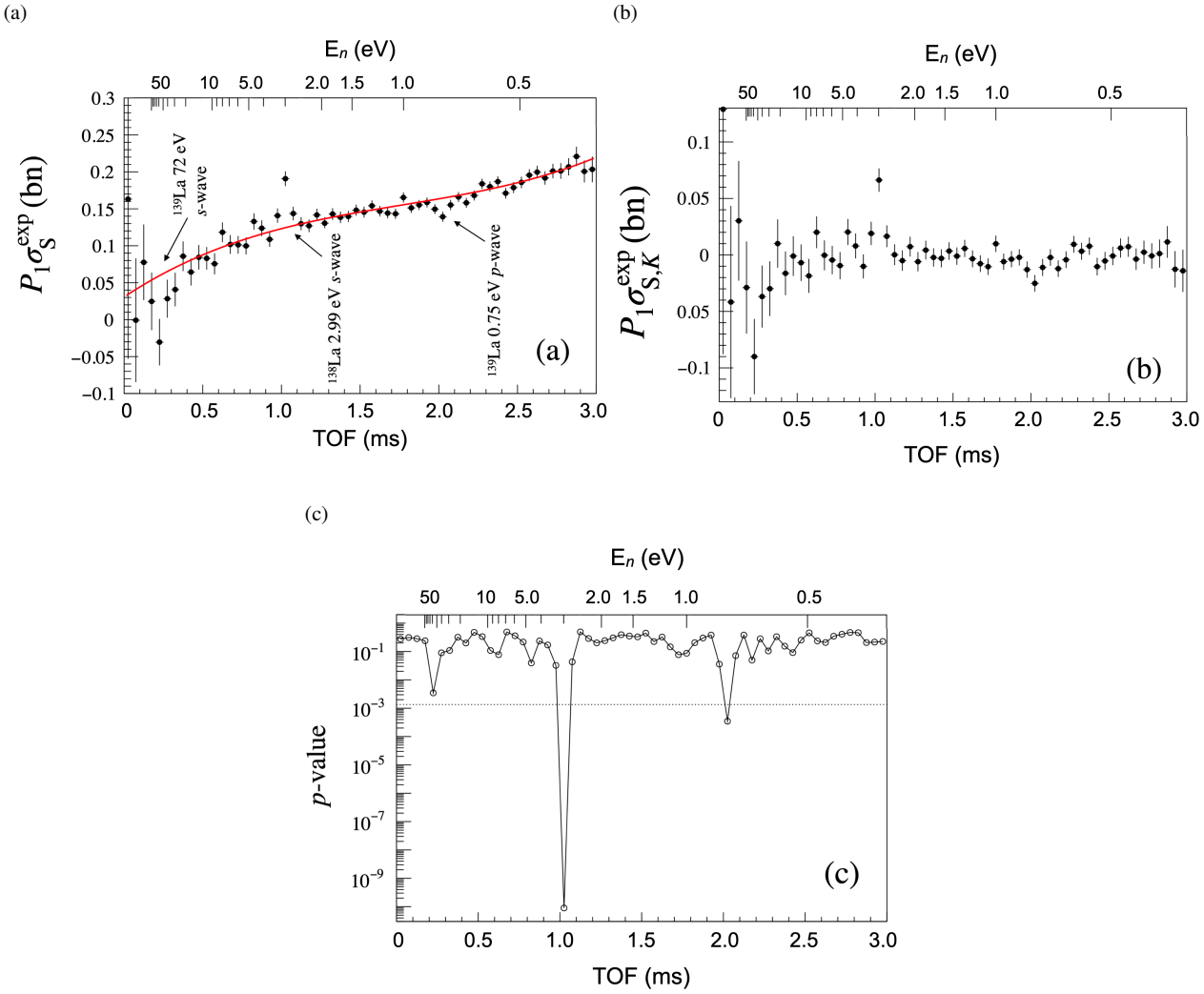

Fig. 4.16 (a) TOF dependence of $P_1\sigma_{\rm S}^{\rm exp}$. The curved line is the best fit of the global structure derived from the negative s-wave resonance. (b) Resonance component of spin-dependent cross section. (c) p-value for $P_1\sigma_{{\rm S},p}$. The dotted line shows a 99.7% confidence level.

component was also obtained as

$$\begin{aligned}\varepsilon_{\rm S} &= \frac{\sigma_+^p - \sigma_-^p}{\sigma_+^p + \sigma_-^p} = \frac{\sigma_{{\rm S},p}^{\rm exp\ theo}}{\sigma_0, p} \\ &= -0.36 \pm 0.11\end{aligned} \tag{4.13}$$

The spin-independent cross section $\sigma_{0,p}^{\rm theo}$ was theoretically calculated by the total cross section contributed from the p-wave represented as ${\rm Im}A'$ based on the optical theorem in Eq.2.70. When utilizing the nuclear polarization P_1 calculated from the thermometer temperature measured at the cold head, the differences between the values of $\sigma_{{\rm S},p}^{\rm exp}$ and $\varepsilon_{\rm S}$ from those calculated in Eq.4.12 and Eq.4.13 were +0.03 bn and +0.04 bn, respectively. These differences were found to be smaller than the statistical error.

Chapter 5

Analysis

Given the orientation of the neutrons and nuclear polarization during the experiment, the spin-dependent asymmetry can be described from Eq.4.7 and 3.35 as

$$\begin{aligned} A_{\rm pow} &= \bar{p}_0^p \tanh(2{\rm Im}\beta_x) \\ &\simeq \bar{p}_0^p \frac{4\pi}{k_n} \rho_{\rm La} d_{\rm La} {\rm Im}\mathcal{B} \end{aligned} \tag{5.1}$$

The beam divergence and the vector, 2nd-, and 3rd-rank tensor polarization were already obtained from the previous discussion in chapter 4. Non-zero values of the $(\hat{\boldsymbol{k}}_n \cdot \hat{\boldsymbol{I}})$ originate from the beam divergence up to the maximum value of 2×10^{-3}. Then, the dominant contribution in the $\mathcal{B}$ term can be determined by comparing it with each value at p-wave resonance as

$$\frac{P_2 {\rm Im}F'(\hat{\boldsymbol{k}}_n \cdot \hat{\boldsymbol{I}})}{P_1 {\rm Im}B'} \sim 10^{-8}, \quad \frac{P_3 {\rm Im}B_3'/3}{P_1 {\rm Im}B'} \sim 10^{-7} \tag{5.2}$$

Therefore, the spin-dependent asymmetry Eq.5.1 can be approximated as

$$A_{\rm pow} \simeq P_1 \bar{p}_0^p \frac{4\pi}{k_n} \rho_{\rm La} d_{\rm La} {\rm Im}B' \tag{5.3}$$

representing the spin-spin interaction in the forward scattering amplitude.

5.1 Determination of partial neutron width using spin-dependent neutron cross section

As mentioned in chapter 2, the partial neutron width can be extracted from the angular correlations of γ-rays emitted from p-wave resonances, which arise from interference between s- and p-wave amplitudes. The advantage of using the spin-dependent cross section is that the neutron partial width can be directly determined without assuming the interference between partial amplitudes and the final state spin after the γ decay. The spin-dependent cross section at the p-wave resonance can be calculated using the explicit theoretical expression of B' in Eq.2.70 as

$$\sigma_{{\rm S},p}^{\rm theo} = \frac{4\pi}{k_n} {\rm Im}B' = \frac{\pi}{16 k_n^2} \frac{\Gamma_p^n \Gamma_p}{(E - E_p)^2 + (\Gamma_p/2)^2} \left(-\frac{39}{4} x_S^2 + \frac{9}{2}\sqrt{\frac{7}{5}} x_S y_S + \frac{63}{20} y_S^2 \right) \tag{5.4}$$

where x_S and y_S are defined in Eq.2.36. The broadening effect by the pulse shape of the neutron beam at 0.75 eV was negligibly small compared with the total width of the p-wave resonance and the statistical error. Therefore, the spin-dependent cross section obtained in Eq.4.12 can be directly compared with the theoretical calculation. Calculating the Breit-Wigner function over the region $E_p - 3\Gamma_p < E_n < E_p + 3\Gamma_p$ in Eq.5.4 and converting

(x_S, y_S) to (x_F, y_F) based on Eq.2.28, the following equation can be obtained as

$$-0.26 \pm 0.08 = 0.079 \left(-7x_F^2 - 2\sqrt{35}x_F y_F + \frac{2}{5} y_F^2 \right) \tag{5.5}$$

Therefore, the solutions for ϕ_F as

$$\phi_F = (74 \pm 4)^\circ,\ (164 \pm 4)^\circ,\ (254 \pm 4)^\circ,\ (344 \pm 4)^\circ \tag{5.6}$$

The corresponding x_F and y_F values are also obtained as

$$\begin{aligned}(x_F, y_F) =& (0.28 \pm 0.06,\ 0.96 \pm 0.02),\ (-0.96 \pm 0.02,\ 0.28 \pm 0.06),\\ & (-0.28 \pm 0.06,\ -0.96 \pm 0.02),\ (0.96 \pm 0.02,\ -0.28 \pm 0.06).\end{aligned} \tag{5.7}$$

5.2 Determination of the physical solution

The four possible solutions were obtained from the spin-dependent cross section measurement. As discussed in chapter 2.5, the angular correlation measurements in the (n, γ) reactions depend on the exit channel parameters. Therefore, the results of the (n, γ) measurement were utilized to determine the physical solution from the possible four solutions obtained by neutron transmission experiments that are independent of the final state.

As the same proceedure depicted in Fig2.3, equations 5.5, 2.48, 2.53, and 2.49 can be interpreted as the probability density function (PDF) on the unit circle. The PDFs suggest that the physical solution is in the second qudrant on the (x_F, y_F) plane as shown in Fig.5.2. Thus the physical solution is obtained as $(x_F, y_F) = (-0.96 \pm 0.02,\ 0.28 \pm 0.06)$, which corresponds to

$$\phi_F = (164 \pm 4)^\circ. \tag{5.8}$$

Therefore, the spin-dependent factor in Eq.2.38 is obtained as

$$\kappa(J) = 0.59 \pm 0.05. \tag{5.9}$$

The p-wave resonance cross-section is calculated to be 3.06 ± 0.09 barn using the optical theorem in Eq.2.70 and the resonance parameters in Tab.2.3, and with the longitudinal asymmetry in Tab.2.1, the TRIV cross-section in Eq.2.34 is

$$\Delta\sigma_T = (0.17 \pm 0.02) \frac{w}{v}\,(\text{barn}). \tag{5.10}$$

5.3 Fundamental TRIV effects in compound necleus

As mentioned in Chapter 1.2.2, the effects of TRIV in the compound nucleus may be related to the effects of PV in a three-body system of neutron-deuteron scattering [23]. The neutron helicity-dependent asymmetry P_L^{nd} was theoretically calculated [21] using the best value of DDH potential, including the strong potential of Argonne two-nucleon interaction [99] and the Urbana IX three-nucleon interaction [100], as follows

$$P_L^{nd} = 0.899 \times 10^{-8}. \tag{5.11}$$

This value was calculated for the case of the DDH potential with infinite cutoff and a total cross-section of $3.35\,\text{bn}$ at $E_n = 15\,\text{keV}$. Therefore, using Eq.5.9 and the longitudinal asymmetry $P_L = 0.0955$ of ^{139}La in Tab.2.1, the enhancement of TRIV in Eq.2.34 denoted as A_{La}, which relate to the neutron cross sections of TRIV and PV, can be calculated as

$$A_{\text{La}} = \kappa(J) \frac{P_L}{P_L^{nd}} \sim 6 \times 10^6 \tag{5.12}$$

Thus, the effects of TRIV were found to be 6×10^6-fold, as well as the effects of PV.

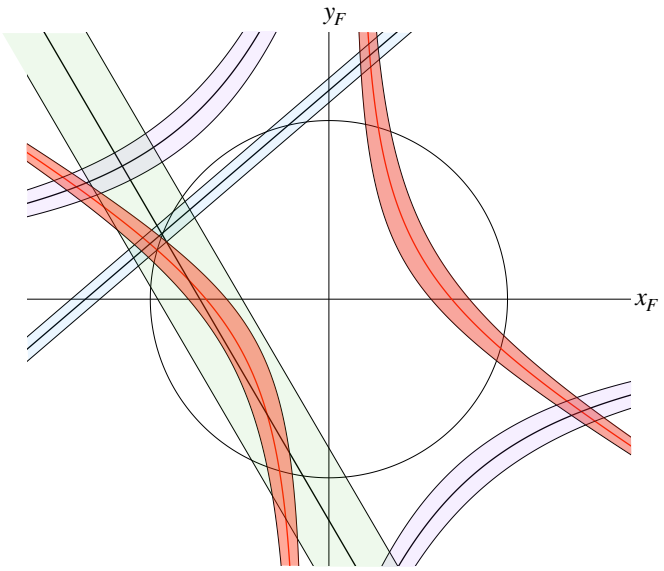

Fig. 5.1 Visualization of the value of ϕ on the (x, y) plane.The red, blue, green, and purple filled areas represent Eqs.5.5, 2.48, 2.53, and 2.49 with 1σ region. The corresponding solid lines indicate the central values.

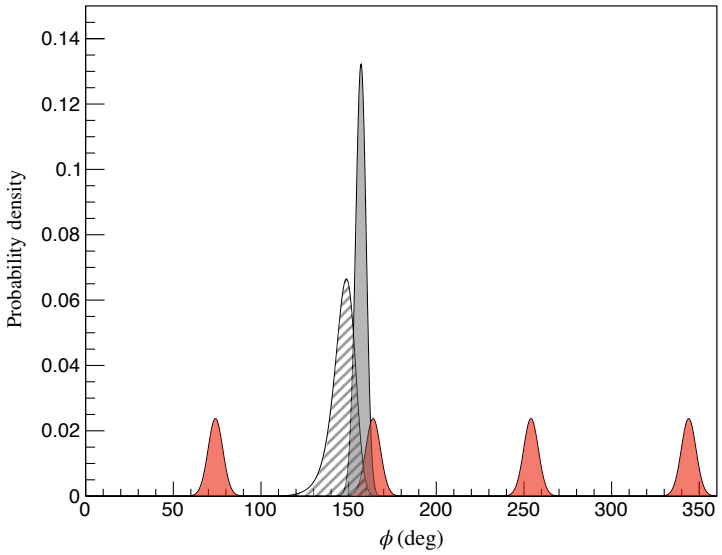

Fig. 5.2 PDFs for ϕ on the unit circle. The red, shaded, and gray filled area represent the PDFs of Eq.5.5, the product of PDFs of Eqs.2.48, 2.53, and 2.49, and the product of PDFs of Eqs.5.5, 2.48, 2.53, and 2.49, respectively.

Chapter 6

Discussion

Since the explicit forward scattering amplitude for $^{139}\mathrm{La}$ was calculated in Chapter 2, the spin observables in neutron transmission can now be calculated without any omission shown in Chapter 3. In addition, we obtained the most plausible mixing angle ϕ_F in the analysis. Thus, these provide specific quantities of possible systematic uncertainties and experimental sensitivity for TRIV search with neutron optics. In this chapter, the configuration and possible systematic uncertainties of future experiments in the TRIV search, as well as the achievable experimental sensitivity, will be discussed.

6.1 Concept of the future experiment for TRIV search

6.1.1 Experimental configuration

As shown in Eq.3.36, the most sensitive neutron transmission experiments for TRIV will be achieved by the combination of analyzing power and polarizing power, $A_y + P_y$. The concept of the experimental apparatus is depicted in Fig.6.1 in which the nuclear spin and the neutron spin lie on $(\vartheta_I, \varphi_I) = (\pi/2, 0)$ and $(\vartheta_\sigma, \varphi_\sigma) = (\pi/2, \pi/2)$, respectively, corresponding to the ideal spin direction. A quantization axis of $^3\mathrm{He}$ spin filter is determined parallel to the y axis due to the B_0 coil, and a polarized neutron beam is transported to just before the polarization target with its spin direction maintained by the guide magnet. A target, $\mathrm{LaAlO_3}$, is polarized using the DNP method under an environment of a temperature of 0.1 K and an applied magnetic field of 5 T. The nuclear polarization is still maintained even in a zero magnetic field by using the spin-frozen method. The spin-frozen method is already used for protons and deuterium to decouple nuclear and electron spin by bringing the electron spin polarization close to 100% at a cryogenic temperature, thereby yielding a long relaxation time for the nuclear spin [101, 102]. The pseudomagnetic field adjusting for the p-wave resonance is canceled by applying a magnetic field B_{ext} to the polarized target in the opposite direction of the polarization. The polarized target is attached to the cold head of the dilution refrigerator and is surrounded by an RF coil to apply the external magnetic field and a superconducting magnetic shield made of niobium. The superconducting shield is designed to prevent a stray magnetic field of the target, and because the magnetic field becomes discontinuous at this boundary, neutron spin incidents into the polarized target unadiabatically. A two-dimensional position-sensitive neutron detector is installed downstream of the polarized target to monitor the transmitted neutron beam energy and beam divergence. The design of the superconducting magnetic shield and coils around the polarization target is under discussion, and the detailed design is not mentioned here. At the same time, we should consider the Kapitza resistance [103] in solid-solid interfacial thermal resistance between the cold head and the target for cooling to 0.1 K and the thermal conductivity of heat inflow caused by radiation to design the size and shape of the target. Since the analyzing power and polarizing power are assumed to be measured independently, it is required that the measurements for correcting for neutron and nuclear spin misalignment, nuclear polarization, and external magnetic field misalignment should be performed for each asymmetry. These correction methods are described in the following section.

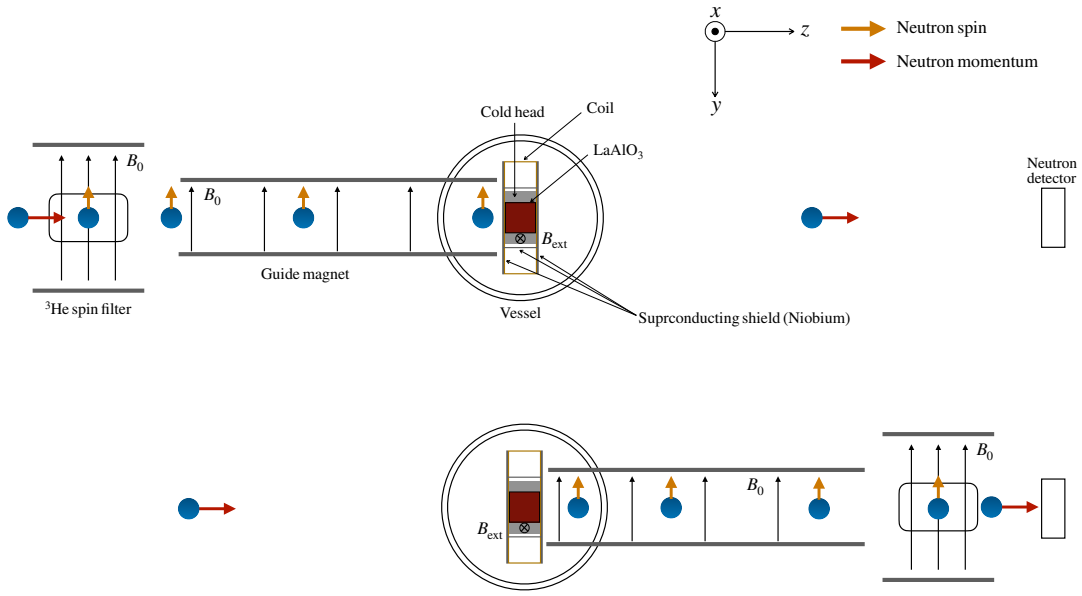

Fig. 6.1 Aparatus to search for the TRIV with neutron optics. The upper and lower figures correspond to analyzing power and polarizing power measurements, respectively. It is assumed that each measurement will be performed independently. ^{3}He spin filter, a guide magnet, a $LaAlO_3$ target and its polarization device, a superconducting magnetic shield, and a neutron detector are installed.

6.1.2 Nuclear target

Pseudomagnetism

The pseudomagnetism has already been mentioned in chapter 3.2, however since this calculation only considered ^{139}La with 100% purity, we will discuss it again for $LaAlO_3$, which is used as a polarized target. Since $LaAlO_3$ target is composed of elements such as oxygen with zero nuclear spin and aluminum with nuclear spin $I = 5/2$, it is necessary to consider not only ^{139}La but also pseudomagnetism caused by ^{27}Al at the same time. Let the nuclear polarization of ^{27}Al be P_{Al} and the correlation term proportional to $(\boldsymbol{\sigma} \cdot \hat{\mathrm{I}})$ be B'_{Al}, the scattering amplitude corresponding to the pseudomagnetism is expressed as

$$\mathrm{Re}P_{\mathrm{Al}}B'_{\mathrm{Al}} = \frac{I}{2I+1}P_{\mathrm{Al}}\left(b^{\mathrm{Al}}_{\mathrm{coh}(+)} - b^{\mathrm{Al}}_{\mathrm{coh}(-)}\right) \tag{6.1}$$

where $b^{\mathrm{Al}}_{\mathrm{coh}(+)}$ and $b^{\mathrm{Al}}_{\mathrm{coh}(-)}$ are the coherent scattering length for neutron spin parallel and antiparallel, respectively. Since ^{27}Al has no resonance for incident neutron energy below 1 keV, it can be treated as a constant independent of neutron energy in the p-wave resonance of ^{139}La. Therefore, the pseudomagnetic field of polarized $LaAlO_3$ target can be calculated as

$$B_p = \frac{2\pi\hbar^2}{m_n\mu_n}\rho_{\mathrm{LaAlO_3}}\left(\mathrm{Re}P_1B' + \mathrm{Re}P_{\mathrm{Al}}B'_{\mathrm{Al}}\right) \tag{6.2}$$

As mentioned in chapter 2.4, the study for $LaAlO_3$ using DNP method has been achieved

$$P_1 = 47.5\%, \quad P_{\mathrm{Al}} = 62\%. \tag{6.3}$$

Applying these results for Eq.6.2, thus it leads to

$$B_p = 0.10\,\mathrm{T} \tag{6.4}$$

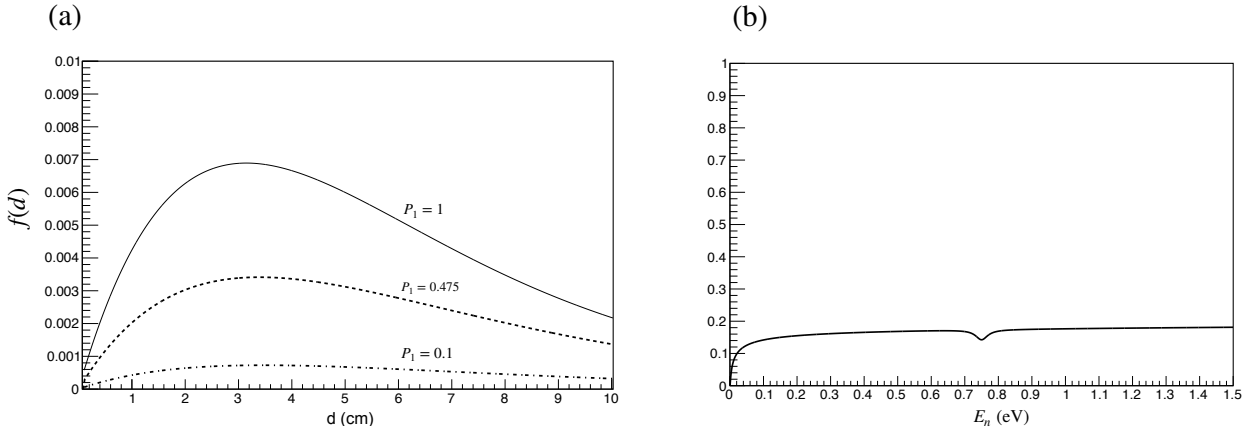

Fig. 6.2 Optimal thickness for $LaAlO_3$ and its neutron transmission. (a): The maximum value of the curve, d, indicates the optimum thickness, and the solid, dashed, and solid-dashed lines correspond to the varying vector polarization of ^{139}La. (b): Neutron transmission with optimal thickness for neutron energy.

where $\rho_{\mathrm{LaAlO_3}} = 1.887 \times 10^{28}\,/\mathrm{m}^3$, $b^{\mathrm{Al}}_{\mathrm{coh}(+)} = 3.60\,\mathrm{fm}$, and $b^{\mathrm{Al}}_{\mathrm{coh}(-)} = 3.24\,\mathrm{fm}$ were used as the number of nuclei of $LaAlO_3$, and coherent scattering length [3].

Optimal thickness of the target

We discuss the optimal $LaAlO_3$ target thickness in terms of the TRIV search sensitivity and statistics in the measurements shown in Fig.6.1. Let the statistical errors for A_y and P_y be ΔA_y and ΔP_y, respectively, the statistical error for $A_y + P_y$ can be expressed as $\sqrt{\Delta A_y^2 + \Delta P_y^2}$. Therefore, a function with thickness d as an argument is introduced as

$$f(d) = \frac{A_y + P_y}{\sqrt{\Delta A_y^2 + \Delta P_y^2}} \tag{6.5}$$

then was maximized to find the value for d. Let N_+ and N_- denote the number of neutron transmissions at the asymmetry according to Eq.3.16, $\mathrm{Re}A^*D \pm \mathrm{Im}B^*C$, the observables proportional to p_y^p or p_y^a, are very small at 10^{-3} even in the vicinity of the p-wave resonance, then denote as $N \equiv 2N_+ = 2N_-$ since $N_+ \sim N_-$ in the statistical error discussion. The number of neutrons after passing through the polarized target is $N = \exp(-\rho_{\mathrm{LaAlO_3}}\sigma_{\mathrm{LaAlO_3}}d)$, which can be described as

$$\sqrt{\Delta A_y^2 + \Delta P_y^2} = \frac{\sqrt{2}}{\sqrt{\exp(-\rho_{\mathrm{LaAlO_3}}\sigma_{\mathrm{LaAlO_3}}d)}}. \tag{6.6}$$

Here, $\sigma_{\mathrm{LaAlO_3}}$ represents the total cross section of the target, and the total cross section for each nuclide at 0.75 eV for neutron energy can be calculated as

$$\sigma_{\mathrm{La}} = 16.17\,\mathrm{bn}, \quad \sigma_{\mathrm{Al}} = 1.55\,\mathrm{bn}, \quad \sigma_{\mathrm{O}} = 4.23\,\mathrm{bn} \tag{6.7}$$

based on 2.70, and scattering length in [83]. Therefore $\sigma_{\mathrm{LaAlO_3}} = 30.4\,\mathrm{bn}$ can be calculated and substituted into Eq.6.5 and can be expressed as Fig.6.2. This result indicates the optimal thickness is 3.4 cm for a vector polarization 0.475 for ^{139}La and neutron transmission of 14%. Essentially, the optimization function is strongly dependent on transmittance, indicating that changes in vector polarization have no significant effect on the optimal thickness.

6.2 Possible systematics

As mentioned in chapter 6.1.1, the experiment should be tuned by intentionally creating a misalignment of the neutron, nuclear spin, and the external magnetic field and feedback during the asymmetry measurement. In this

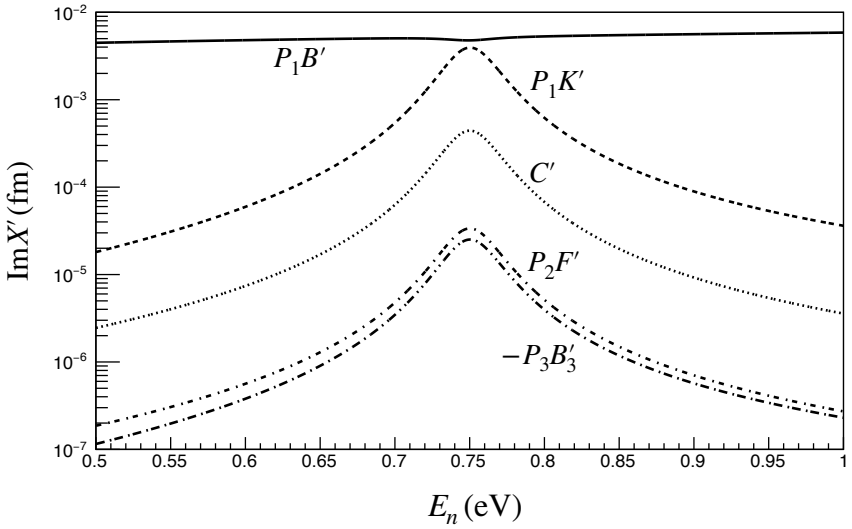

Fig. 6.3 Comparison of the imaginary part of each coefficient for $\mathcal{B}$ and $\mathcal{C}$.

section, we will specifically indicate how the quantities of the coefficients proportional to 2nd- or 3rd-rank tensor polarization are calculated and observables intentionally shifted for each spin and the external magnetic field.

6.2.1 Higher-rank tensor polarization

As Eq.3.35 shows, the spin correlation terms in the forward scattering amplitude f consist of a linear combination of 1st- to 3rd- rank tensor polarizations or coefficients proportional to $(\hat{\boldsymbol{k}}_n \cdot \hat{\boldsymbol{I}})$. The $\mathcal{A}$ vanishes by taking the asymmetry, however the other terms represented by Eq.3.9 remain as β_i and their contribution must be considered. Here we discuss the contribution of observables of terms proportional to higher-rank tensor polarization or $(\hat{\boldsymbol{k}}_n \cdot \hat{\boldsymbol{I}})$ by comparing terms other than the leading terms for $\mathcal{B}$ and $\mathcal{C}$, except for $\mathcal{D}$.

Consider the case in which the vector polarization of $P_1 = 0.475$ is achieved and the pseudomagnetism is completely canceled. Assuming that the spin temperature of the tensor polarization obeys a Boltzmann distribution, the 2nd- and 3rd-rank tensor polarization as $P_2 = 0.16$, $P_3 = 0.044$ was calculated from Eq.2.74. Next, the assumption that the nuclear spin is perfectly aligned along the x axis and the neutron beam divergence is 1 mrad leads to $(\hat{\boldsymbol{k}}_n \cdot \hat{\boldsymbol{I}}) \sim 1 \times 10^{-3}$. Since Eq.3.25 indicates that the imaginary parts of β_x and β_y are dominant, the imaginary parts for each coefficient are compared and shown in Fig.6.3. This result leads to the following ratios at p-wave resonance as

$$\begin{aligned} &\frac{P_2\mathrm{Im}F'(\hat{\boldsymbol{k}}_n \cdot \hat{\boldsymbol{I}})}{P_1\mathrm{Im}B'} = 7 \times 10^{-6}, \quad \frac{P_3\mathrm{Im}B'_3/3\left((\hat{\boldsymbol{k}}_n \cdot \hat{\boldsymbol{I}})^2 - 1\right)}{P_1\mathrm{Im}B'} = 5 \times 10^{-3} \ \text{ for } \mathcal{B} \\ &\frac{P_1\mathrm{Im}K'(\hat{\boldsymbol{k}}_n \cdot \hat{\boldsymbol{I}})}{\mathrm{Im}C'} = 9 \times 10^{-3}, \quad \frac{P_2\mathrm{Im}F'/3}{\mathrm{Im}C'} = 8 \times 10^{-2}, \quad \frac{2P_3\mathrm{Im}B'_3/3}{\mathrm{Im}C'} = -6 \times 10^{-2} \ \text{ for } \mathcal{C} \end{aligned} \tag{6.8}$$

The calculation indicates that under the condition that the pseudomagnetic field is completely canceled, the contribution of coefficients other than the leading term is at most 8%. In light of this result, we ignore the higher-rank tensor polarization in the following discussion, and thus only the leading terms P_1B' and C' can be taken into account.

6.2.2 Neutron and nuclear spin misalignments

Stray fields due to the target-applied magnetic field and the tilt of neutron spins due to the accuracy of the polarizer and analyzer and the guide magnet appear as unintended observables. Therefore, it is possible to measure the misalignment and get feedback on the measurement by indicating the observed quantities for the neutron spin

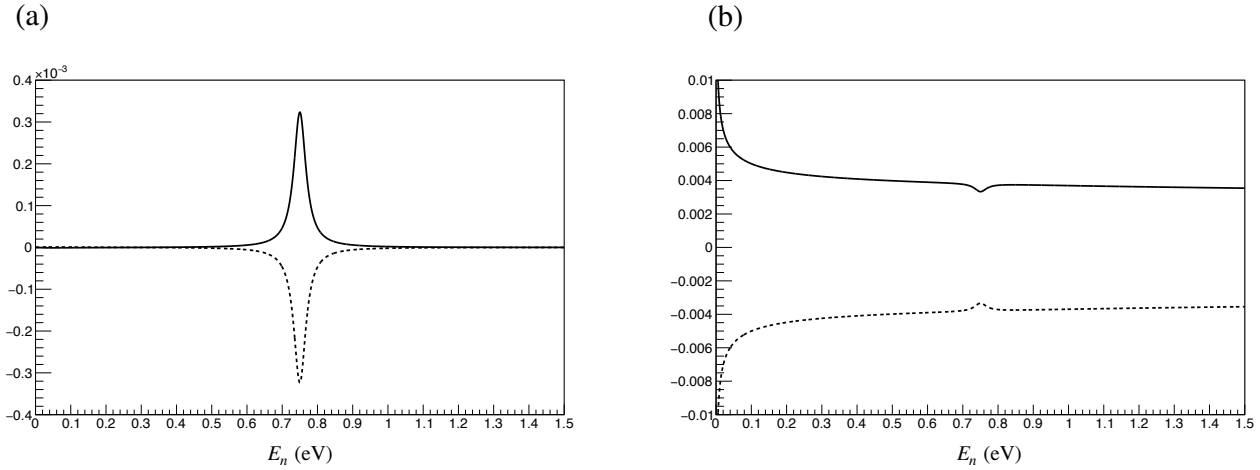

Fig. 6.4 The deviation of varying neutron spin angle in Eq.6.9. The solid and dashed lines correspond to the -1° and $+1^\circ$ from 90°, respectively. The left figure (a) and the right figure (b) represent varying of ϑ^p_σ and φ^p_σ. The pseudomagnetism is completely canceled for $P_1 = 0.475$, the polarizer efficiency $p^p_0 = 1$, and the target thickness is optimal (3.4 cm).

misalignment.

Neutron spin

We first assume that the nuclear spin is perfectly aligned, i.e., $(\vartheta_I, \varphi_I) = (\pi/2, 0)$, and discuss the deviation of the asymmetry (e.g., analyzing power) with neutron spin. Let the analyzing power, given in Eq.3.17, denote $A^{\vartheta^p_\sigma,\varphi^p_\sigma}_{\rm pow}$. For only one angle parameter, the deviation from the ideal neutron spin orientation can be described as

$$\begin{aligned} A^{\pi/2,\pi/2}_{\rm pow} - A^{\vartheta^p_\sigma,\pi/2}_{\rm pow} &= 2\frac{(1-\sin\vartheta^p_\sigma){\rm Im}B^*C - \cos\vartheta^p_\sigma {\rm Re}A^*C}{|A|^2+|B|^2+|C|^2} \\ A^{\pi/2,\pi/2}_{\rm pow} - A^{\pi/2,\varphi^p_\sigma}_{\rm pow} &= 2\frac{(1-\sin\varphi^p_\sigma){\rm Im}B^*C - \cos\varphi^p_\sigma {\rm Re}A^*B}{|A|^2+|B|^2+|C|^2} \end{aligned} \tag{6.9}$$

for $w/v = 0$ of the TRIV parameter. Equation 6.9 when $\vartheta^p_\sigma = (90 \pm 1)^\circ$ and $\varphi^p_\sigma = (90 \pm 1)^\circ$ are shown in Fig.6.4, respectively. One degree deviation around 90 degrees shows the opposite asymmetry in the vicinity of p-wave resonance and the magnitude of the asymmetry is larger than 10^{-4}, which indicates a enough large magnitude to measure quickly as shown in Fig.4.12.

Nuclear spin

We next assume that the neutron spin is perfectly aligned, i.e., $(\vartheta^p_\sigma, \varphi^p_\sigma) = (\pi/2, \pi/2)$. The nuclear spin misalignment in the asymmetry denoted as $A^{\vartheta_I,\varphi_I}_{\rm pow}$ can be described as follows

$$\begin{aligned} A^{\pi/2,0}_{\rm pow} - A^{\vartheta_I,0}_{\rm pow} &= \frac{2({\rm Im}B^*C - {\rm Im}B^*_\vartheta C_\vartheta)}{|A|^2+|B|^2+|C|^2} \\ A^{\pi/2,0}_{\rm pow} - A^{\pi/2,\varphi_I}_{\rm pow} &= \frac{2({\rm Im}B^*C - {\rm Im}B^*_\varphi C_\varphi)}{|A|^2+|B|^2+|C|^2} \end{aligned} \tag{6.10}$$

where B_ϑ, C_ϑ and B_φ, C_φ are satisfied with in Eq.3.7 and approximation of Eq.6.8 as follows

$$\begin{pmatrix} \beta^\vartheta_x \\ \beta^\vartheta_y \\ \beta^\vartheta_z \end{pmatrix} = Z \begin{pmatrix} (P_1B' - \mu_{\rm eff}B_{\rm ext})\sin\vartheta_I \\ 0 \\ C' + (P_1B' - \mu_{\rm eff}B_{\rm ext})\cos\vartheta_I \end{pmatrix}, \quad \begin{pmatrix} \beta^\varphi_x \\ \beta^\varphi_y \\ \beta^\varphi_z \end{pmatrix} = Z \begin{pmatrix} (P_1B' - \mu_{\rm eff}B_{\rm ext})\cos\varphi_I \\ (P_1B' - \mu_{\rm eff}B_{\rm ext})\sin\varphi_I \\ C' \end{pmatrix} \tag{6.11}$$

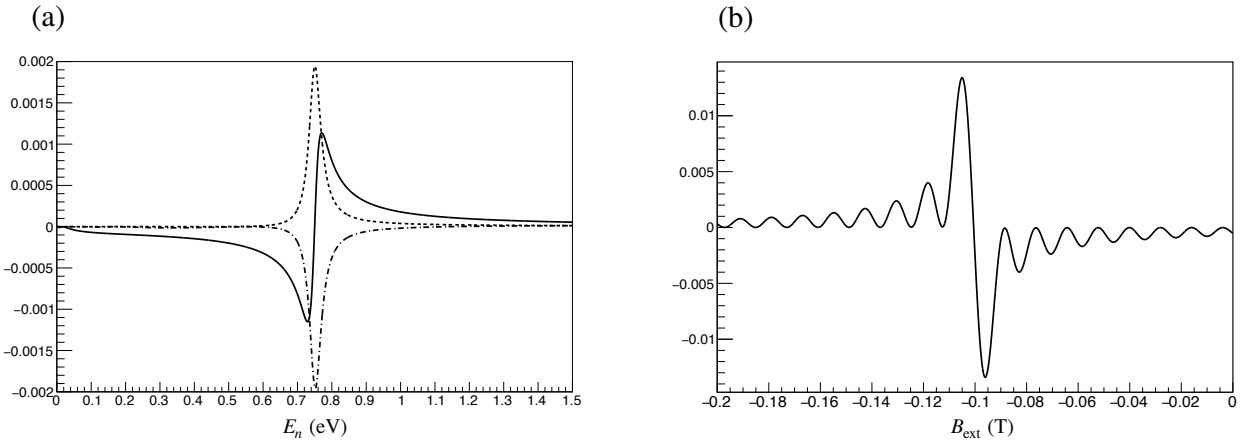

Fig. 6.5 Dependency of the external magnetic field. (a): The solid, dashed, and dashed-dotted lines correspond to the asymmetry in Eq.6.12 of ±0 G, -100 G, and +100 G from the pseudomagnetism calculated in Eq.6.4, respectively. (b): The maximum value of the asymmetry at p-wave resonance for the external magnetic field.

In this case, since the neutron and nuclear spin misalignment are equivalent in the observed asymmetries for ϕ_σ^p, the 1-degree deviations in ϑ_I and φ_I correspond to (b) in Fig.6.4.

6.2.3 Nuclear polarization and external magnetic field

While it is essential in the TRIV search to completely cancel the neutron spin rotation caused by the pseudomagnetism in nuclear polarization and the external magnetic field, it is generally not easy to measure the actual nuclear polarization of the target accurately, thus it is necessary to find the optimal field while adjusting the external magnetic field. Therefore, it is useful to show how much the spin observables depend on the external magnetic field. Here we propose a method to find the optimum external magnetic field from the asymmetry of the spin observable, assuming an experimental system in which the neutron and nuclear spin are perfectly aligned. The asymmetry consists of the imaginary part of the interference term between the helicity-dependent term C' and the B' term involving the pseudomagnetic field and the external magnetic field as follows

$$A_y = \frac{2p_0^p \mathrm{Im} B^* C}{|A|^2 + |B|^2 + |C|^2}. \tag{6.12}$$

Assuming a polarizer efficiency of $p_0^p = 1$ and $D' = 0$, the calculation results, when the external magnetic field is varied around the pseudomagnetic field by ± 100 G, are shown in Fig.6.5. It indicates that the sign of the asymmetry changes as the pseudomagnetic field varies, and a 100 G change results in a magnitude shift of 0.002 at the p-wave resonance. The measurement of the asymmetry in the p-wave resonance while manipulating the external magnetic field corresponds to (b) in Fig.6.5, and it can be utilized to ascertain the external magnetic field required to nullify the pseudomagnetism.

It should be noted that in actual experiments, misalignments occur not individually but in combination. Therefore, it is necessary to extract and correct individual misalignments by shifting the spins and magnetic field by a relatively large ammount.

6.3 Sensitivity estimation

We discuss the possible experimental sensitivity to TRIV that can be explored in the neutron transmission shown in Fig.6.1. Assume $4\,\mathrm{cm} \times 4\,\mathrm{cm}$ as the beam cross sectional area of the $\mathrm{LaAlO_3}$ target and an optimal thickness of 3.4 cm for 47.5% vector polarization. The experiment is conducted at beam port 07 in MLF, where the poisoned moderator is employed, shown in Fig.4.1 and assumes a proton beam power of 1 MW. The J-PARC website

[87] publishes the time-integrated intensity of the incident neutron beam for each beam port, and is shown in Fig.6.6. The experimental conditions including the neutron beam optics are summarized in Table 6.1. The ^{3}He

Table 6.1 Experimental condition for beam port 07.

Time-averaged flux of incident neutrons	$I_{\rm in}$	Fig.6.6
Moderator surface area	$S_{\rm mod}$	$100\,{\rm mm} \times 100\,{\rm mm}$
Distance between moderator and target	$L_{\rm mt}$	$15\,{\rm m}$
Cross-sectional area of target	$S_{\rm t}$	$4\,{\rm cm} \times 4\,{\rm cm}$
Solid angle with respect to target area	$\Omega_{\rm t}$	$S_{\rm t}/L_{\rm mt} = 7.11 \times 10^{-6}\,{\rm sr}$
Detector efficiency	$\epsilon_{\rm det}$	1

spin filters as the polarizer and analyzer are used, and we have already calculated the optimal areal density of $\rho_{\rm He}d_{\rm He} = 72{\rm atmcm}$ at room temperature and $P_{\rm He} = 70\%$ for ^{3}He polarization from a previous study of [104] can maximize the figure-of-merit for TRIV search at p-wave resonance. It yields the efficiency of 87% and neutron transmission of 30% at p-wave resonance calculated from Eq.4.9 and

$$T_{\rm He} = \exp(-\rho_{\rm He}d_{\rm He}\sigma_{\rm He})\cosh(P_{\rm He}\rho_{\rm He}d_{\rm He}\sigma_{\rm He}) \tag{6.13}$$

as shown in Fig.6.7. Let the transmission with the optimal thickness target denote as $T_{\rm LaAlO_3}$ as shown in Fig.6.2, thus the detected neutrons $N_{\rm det}$ can be described as

$$N_{\rm det} = \epsilon_{\rm det}T_{\rm He}T_{\rm LaAlO_3}I_{\rm in}S_{\rm mod}\Omega_{\rm t}\Delta E_n \tag{6.14}$$

Thus the energy spectrum of the detected neutrons for $A_{\rm pow}$ and $P_{\rm pow}$ can be obtained as Fig.6.8. We assume the neutron energy width of 30 meV, which corresponds to the $0.8\Gamma_p^\gamma$. Following the same assumption of chapter 6.1.2, we can calculate the statistical error as

$$\Delta A_{\rm pow} = \Delta P_{\rm pow} = \frac{1}{\sqrt{N_{\rm det}}}. \tag{6.15}$$

6.3.1 Sensitivity estimation under ideal experimental condition

Initially, the experimental sensitivity under ideal experimental conditions is presented. We assume the neutron spin, nuclear spin, and pseudomagnetism are completely aligned and adjusted and the polarizer and analyzer neutron efficiency are equal. Summation of the number of detected neutrons over the energy region with $0.72\,{\rm eV} \le E_n \le 0.78\,{\rm eV}$ around p-wave resonance energy of E_p in Fig.6.8 yields 331 kcps; if we hypothesize that new physics can be excluded with 90% confidence level, the evaluation function $f(t)$ is

$$\begin{aligned} f(t) &= 1.64\sqrt{\Delta A_y^2 + \Delta P_y^2} \\ &= 1.64\sqrt{\frac{2}{N_{\rm det}t}} = 4.0 \times 10^{-3}\frac{1}{\sqrt{t}} \end{aligned} \tag{6.16}$$

as a function of measurement time t. The observed asymmetry with the discovery potential $w/v = 2.9 \times 10^{-4}$ estimated in Eq.1.13 averaged for the same energy region of $0.72\,{\rm eV} \le E_n \le 0.78\,{\rm eV}$ as Eq.6.16 can be calculated from Eqs.3.25, 3.36, and 5.10 as

$$|A_y + P_y|_{\rm ave} \simeq 2\rho_{\rm La}d\Delta\sigma_T p_0 P_1 = 4.3 \times 10^{-6} p_0 P_1 \tag{6.17}$$

Here, the averaged P-odd cross-section is used as $\overline{\Delta\sigma_P} = 0.20\,{\rm barn}$. We can show the statistical error and the corresponding sensitivity in Fig.6.9. This result indicates the required measurement time to reach the discovery potential with a 90% confidence level for the case of $p_0 = P_1 = 1$ and $p_0 = 0.87$, $P_1 = 0.475$. Therefore the required measurement time is 240 hours and 1400 hours.

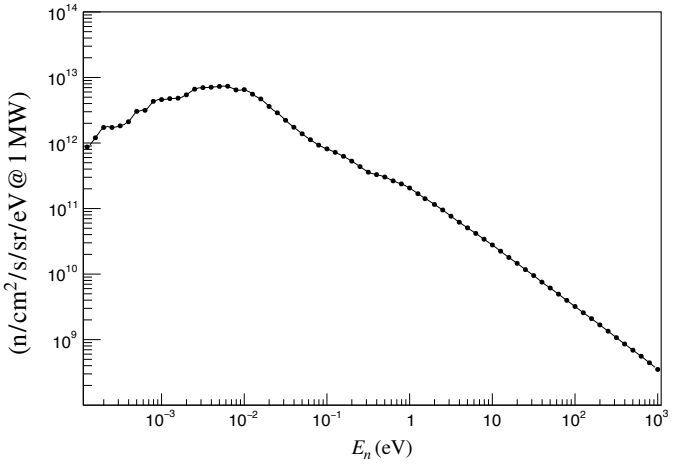

Fig. 6.6 Computed time-averaged neutron intensity for beam port 07 at 1 MW proton beam power. Each point on the graph represents a published data point, and a third polynomial splined function interpolation was applied. The poisoned moderator is employed for this beam port and the intensity is calculated with a moderator surface area of $1\,\mathrm{cm} \times 1\,\mathrm{cm}$ area.

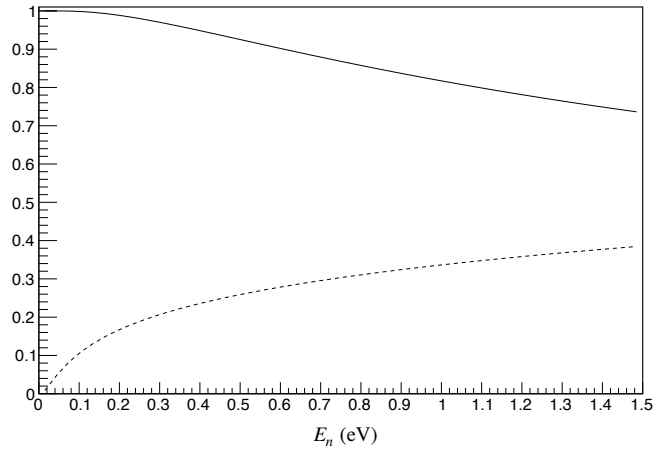

Fig. 6.7 Neutron efficiency and transmission for optimized $^3\mathrm{He}$ spin filter. The solid and dashed lines correspond to the neutron polarizer or analyzer efficiency and neutron transmission, respectively.

6.3.2 Sensitivity estimation with chi-square fitting

The actual experiment involves misalignments arising from various causes outlined in Chapter 6.2. Among these, the control of a neutron spin by a magnetic field and superconducting magnetic shielding poses the most formidable challenge. Therefore, in this section, assuming adjustments have been performed to the nuclear spin and pseudomagnetic field to appropriate values in Eq.6.3 and Eq.6.4, we include a neutron spin in the fitting parameters. This allows us to employ pseudorandom numbers to simulate the experimental sensitivity to the parameter w/v with a chi-square method. The computed asymmetry A_{pow} and P_{pow} are presumed to adhere to Eq.3.17 and Eq.3.19, where the neutron efficiency is consistent for both of $p_0 = 0.87$. The experimental system follows Table 6.1. The asymmetry values generated in the simulation are assumed to follow a Gaussian distribution with a mean of $A_{\mathrm{pow}}(E_i)$ and $P_{\mathrm{pow}}(E_i)$, where E_i is the corresponding neutron energy for Fig.6.8, and a standard deviation following Eq.6.15, representing the statistical error. The simulation results of the asymmetries are shown

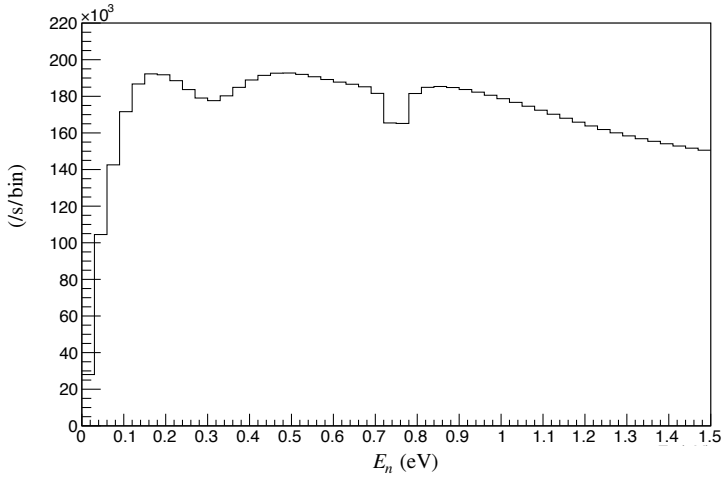

Fig. 6.8 Energy spectrum of the detected neutrons. The bin width of neutron energy is 30 meV.

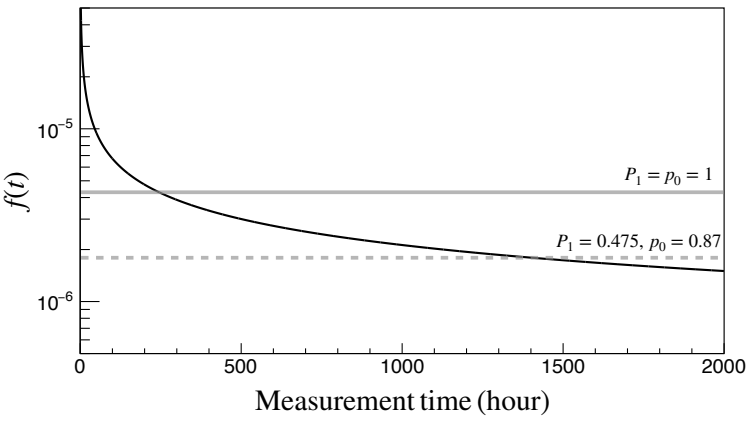

Fig. 6.9 Statistical error and possible measurement sensitivity. The black solid represents the statistical error for measurement time in Eq.6.16. The gray solid and dashed lines correspond to Eq.6.17 for ultimate technology with $p_0 = P_1 = 1$ and present technology with $p_0 = 0.87,\ P_1 = 0.475$, respectively.

in Fig.6.10 for the case where the neutron spin is perfectly aligned at 90 degrees. The value included in coefficient D' is calculated as $w/v = 0$. The experimental sensitivity was obtained from chi-square fitting in the region of $E_p \pm 3\Gamma_p$ with the same function of $A_{\rm pow} + P_{\rm pow}$ with w/v as a free parameter, yielding $w/v = (-7.6 \pm 7.6) \times 10^{-3}$ for a 1-hour measurement, which indicates a zero-consistent with one standard deviation.

Next, consider the case of neutron spin misalignment in $A_{\rm pow}$ and $P_{\rm pow}$. Here, since $\mathrm{Re}A^*C$, the term for which is proportional to $\cos\vartheta_\sigma$, is one-tenth the magnitude of $\mathrm{Re}A^*B$ as shown in Fig.6.4, then the two fitting parameters to represent neutron spin are used as φ^p and φ^a. The fitting function in this case can be written explicitly as follows.

$$A_{\rm pow} + P_{\rm pow} = 2p_0 \frac{(\cos\varphi_\sigma^p + \cos\varphi_\sigma^a)\mathrm{Re}A^*B + (\sin\varphi_\sigma^p + \sin\varphi_\sigma^a)\mathrm{Re}A^*D + (\sin\varphi_\sigma^p - \sin\varphi_\sigma^a)\mathrm{Im}B^*C}{|A|^2 + |B|^2 + |C|^2 + |D|^2} \tag{6.18}$$

To ensure that both $\mathrm{Re}AB$ and $\mathrm{Im}BC$ contributions intentionally appear, the asymmetries of neutron spins with φ^p and φ^a shifted by 1 and 2 degrees from $\pi/2$, i.e. $\varphi^p = 91^\circ, \varphi^a = 92^\circ$, are computed and fitted with Eq.6.18 with three fitting parameters, φ^p, φ^a, and w/v. Figure 6.11 shows the computed results corresponding to 100 hours of measurement time. The chi-square over the number degree of freedom was 1.58 and the w/v was $(2.2 \pm 0.9) \times 10^{-3}$. A reliable experimental sensitivity can be obtained by iterating the generation of random numbers and fitting, which corresponds to the number of measurements. This can be performed by fitting the

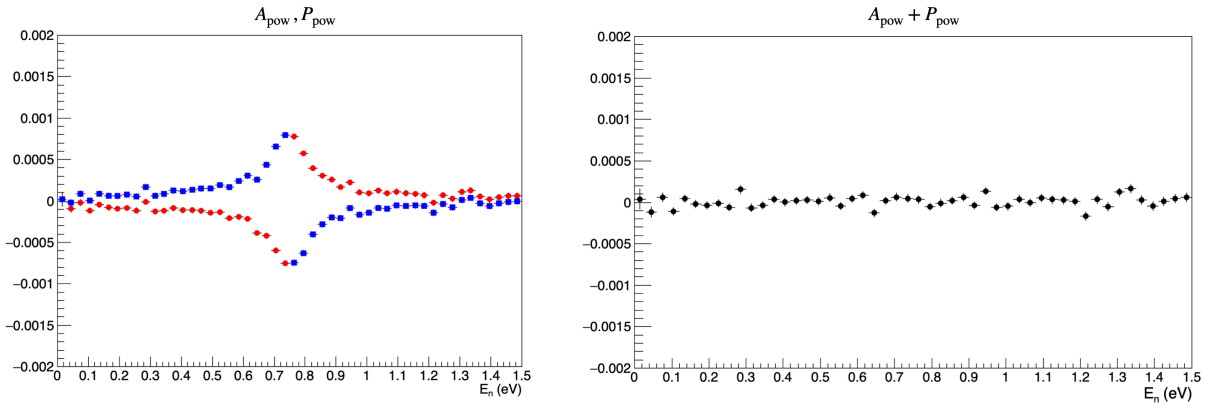

Fig. 6.10 Simulation results for $(\vartheta_\sigma, \varphi_\sigma) = (\pi/2, \pi/2)$ for an hour measurement. The left and right figures show $A_{\rm pow}$ and $P_{\rm pow}$ which correspond to red and blue symbols and the combination. In this condition, $A_{\rm pow}$ and $P_{\rm pow}$ are proportional to $\pm \mathrm{ImB^*C}$.

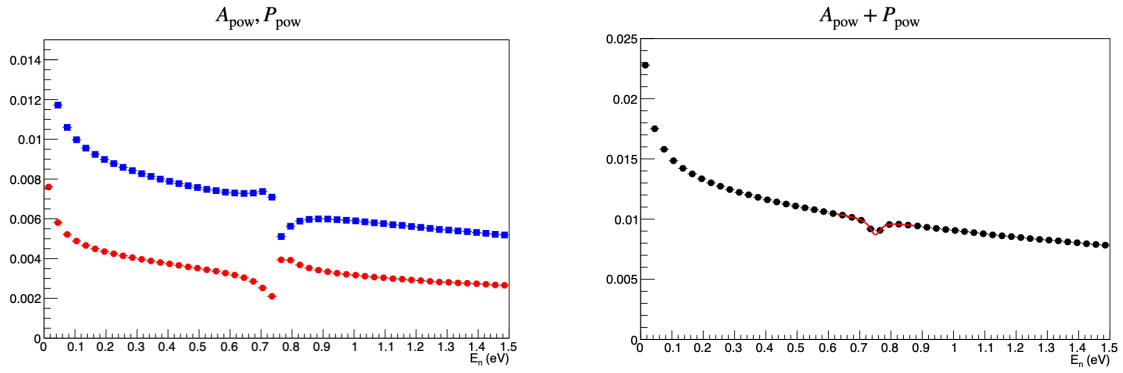

Fig. 6.11 Simulation results for $(\varphi_\sigma^p, \varphi_\sigma^a) = (91^\circ, 92^\circ)$. The left and right figures show $A_{\rm pow}$ and $P_{\rm pow}$, corresponding to red and blue symbols and the combination. The red curve is the best fit in the region of $E_p \pm 3\Gamma_p$.

histogram of the obtained central value of w/v using a Gaussian distribution. The distribution of w/v obtained by iterating the 10 hours measurement 100 times is shown in Fig.6.12. The histogram for w/v under ideal experimental conditions is black, while the histogram with spin misalignment corresponds to red. This result shows that it can be fitted with a Gaussian distribution whose mean value was $(-4.7 \pm 2.3) \times 10^{-4}$ for the ideal case and $(2.3 \pm 4.9) \times 10^{-4}$ for the misalignment, which yields $w/v < 3.8 \times 10^{-4}$ and $w/v < 8.0 \times 10^{-4}$ at a 90% confidence level, respectively. This indicates that the sensitivity deteriorates by only a factor of 2 even when neutron spin misalignment is included. Even in the case of neutron spin misalignment, it is suggested that a six-fold increase in beam intensity or measurement time is needed to reach the discovery potential, which could be solved by an improved neutron source or beam optics dedicated to epithermal neutron transport. Also, as proposed by [28], the theoretical prediction limit induced by axion exchange provides $w/v < 10^{-3}$, which could be meaningful enough for a 10-hour measurement.

6.4 Current upper limit using existing neutron transmission data

The neutron transmission experiment presented in Chapter 4 is a measurement of the spin-dependent cross section proportional to $(\boldsymbol{\sigma} \cdot \hat{\boldsymbol{I}})$. However, it may be possible to obtain an upper limit for TRIV by applying the spin

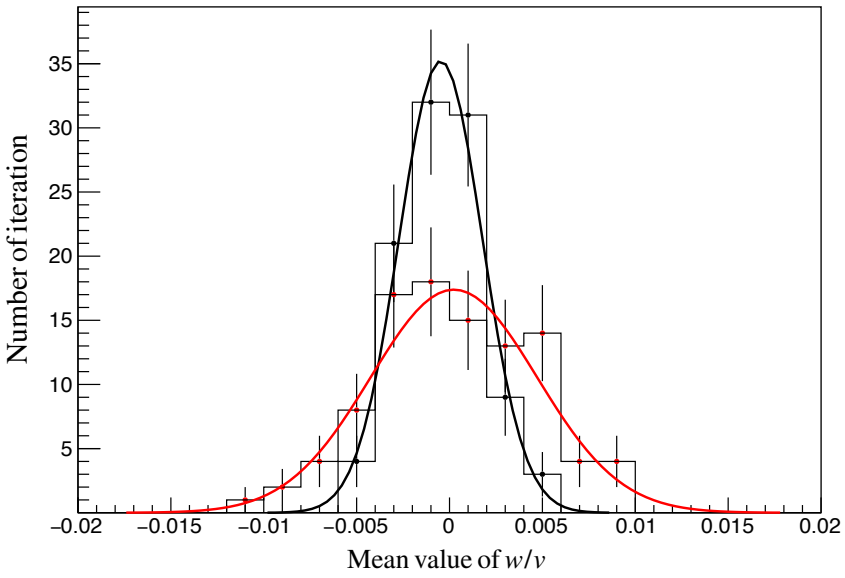

Fig. 6.12 Histograms of w/v for 100 iterations of 10-hour measurements for cases with aligned neutron spin and cases with misalignment. The black and red markers represent the cases where the neutron spin is perfectly aligned and $\Delta\varphi^p = 1^\circ, \Delta\varphi^a = 2^\circ$, respectively, and the solid line represents their corresponding Gaussian fit.

observables described in Chapter 3. This is the first attempt to search for TRIV using a neutron transmission experiment and is considered beneficial because it can serve as an indicator for the upper limit for TRIV discussed above. For the asymmetry $A^x_{\rm pow}/\bar{p_0}^p$, corresponding to Fig.4.12, after being corrected by the averaged neutron polarization, Eq.3.24 can be transformed as

$$\frac{A^x_{\rm pow}}{\bar{p_0}^p} = -2\frac{{\rm Re}A^*B}{|A|^2+|B|^2+|C|^2+|D|^2}. \tag{6.19}$$

In other words, since the denominator represents the total cross section including D, the contribution of TRIV can be evaluated by fitting with w/v as a free parameter. For the mixing angle ϕ_F, Eq.2.55 was used to avoid self-contradiction, and for the nuclear resonance parameters and vector polarization, Table 2.3 and $P_1 = 3.9\%$ were used, respectively. On the other hand, since the independent values of the potential radii R_{s0} and R_{s1} vary with the indefiniteness of the negative resonance, one parameter was reduced by the constraint due to the averaged potential radius as follows

$$R_{\rm ave} = \sqrt{g_4 R^2_{s0} + g_3 R^2_{s1}}. \tag{6.20}$$

Here, $R_{\rm ave} = 5.89 \pm 0.09\,{\rm fm}$ and $g_J = (2J+1)/(2(2I+1))$ from [1]. Therefore, the result of fitting Eq.6.19 in the range of neutron energy $E_p \pm 3\Gamma_p$ with two free parameters R_{s0} and w/v is shown in Fig.6.13. The fitting result yields $\chi^2/{\rm ndf} = 1.9$ and the parameters $R_{s0} = 4.12 \pm 0.04\,{\rm fm}$ and zero-consistent value of $w/v = 0 \pm 4183$. Thus, $|w/v| < 6.8 \times 10^3$ was obtained at a 90% confidence level. This is seven orders of magnitude above our goal of the discovery potential and indicates a potential improvement of that magnitude from the discussion in section 6.3. Therefore, this result provides the constraints on the leading terms in the coupling constants of TRIV in Eq.1.10 as follows

$$-0.47\left[\frac{\bar{g}^{(0)}_\pi}{h^1_\pi} + 0.26\frac{\bar{g}^{(1)}_\pi}{h^1_\pi}\right] < |6.8 \times 10^3|. \tag{6.21}$$

Substituting the value of Eq.1.12, the explored parameter space $(\bar{g}^{(0)}_\pi, \bar{g}^{(1)}_\pi)$ can be illustrated as Fig.6.14. The dominant coupling constants of TRIV for nEDM and HgEDM correspond to $\bar{g}^{(0)}_\pi$ and $\bar{g}^{(1)}_\pi$, respectively, and although they give strong upper limits as $\bar{g}^{(0)}_\pi < 1.6 \times 10^{-10}$ and $\bar{g}^{(1)}_\pi < 0.5 \times 10^{-11}$. However, our experiment indicates that the different parameter spaces can be explored.

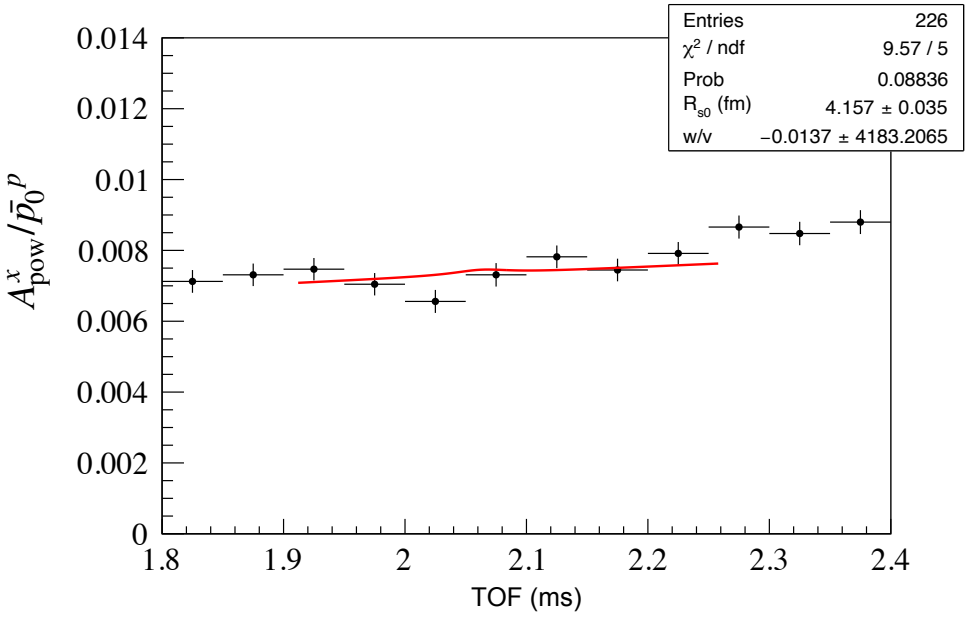

Fig. 6.13 Fit results for asymmetry after correction for averaged neutron polarization. The solid red line represents the fitting function and was fitted to the TOF region corresponding to $E_p \pm 3\Gamma_p$.

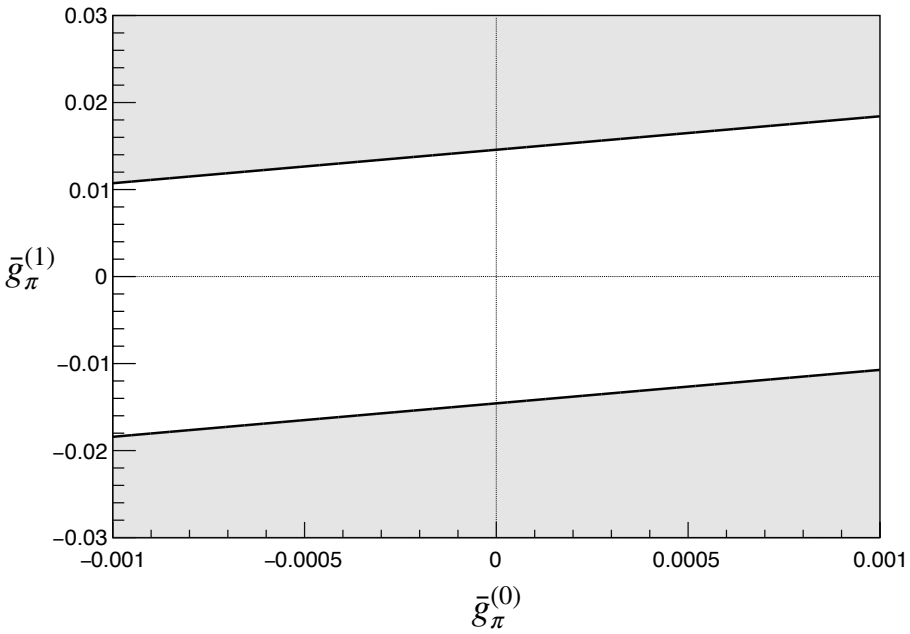

Fig. 6.14 Parameter space on π meson of TRIV isoscalar and isovector coupling constants. The shaded region represents the excluded region at a 90% confidence level with the neutron transmission experiment. The upper limits shown in Eq.1.11 are $\bar{g}_\pi^{(0)} < 1.6 \times 10^{-10}$ and $\bar{g}_\pi^{(1)} < 0.5 \times 10^{-11}$.

Chapter 7

Conclusion

As well as the enhancement of PV in compound nucleus reactions, TRIV can also be enhanced, which is connected to final-state interaction-free transmission experiments in neutron optics. The conditions for the magnitude of parity-violating effects and its low p-wave resonance energy lead to the most promising target nucleus being ^{139}La. The spin-dependent factor $\kappa(J)$, which links the P-odd, P- and T-odd cross sections, is a function of the mixing angle ϕ_F. Due to the complexity of the compound nucleus, ϕ_F is incalculable, and it can only be obtained by experiments sensitive to the p-wave resonance and its sign. In the previous study, ϕ_F was obtained by measuring the asymmetry of the gamma-ray distribution when a compound nucleus excited by a neutron absorption reaction transitions to the ground state. In this study, by applying the technique using the polarized nuclear target and polarized neutrons in neutron transmission experiments, ϕ_F was obtained by comparing the spin-dependent cross-section measurement with the explicit theoretical expression of scattering amplitudes. The phsysical solution, $\phi_F = (164 \pm 4)^\circ$, was determined by restriction of the previous studies. This determination of ϕ_F and the expression of neutron spin observables from the description of the time evolution provide a quantitative basis for our future experiment. It is found that the cross sections that are proportional to the tensor polarization, resulting from realistically achievable nuclear polarization, are at most 8% of the cross-section of the dominat P-odd coefficient when the inner product of the neutron beam and nuclear spin direction is suppressed below 1 mrad. According to the method of tuning the pseudomagnetism, which is the dominant suppression factor in the neutron transmission experiment, it was shown that the deviation in the asymmetries of 2×10^{-3} corresponding to a change in the external magnetic field of ± 100 G is a sufficient amount to monitor neutron rotation, and the application of this method enables the canceling of pseudomagnetism. Based on these arguments, we estimated the experimental sensitivity of TRIV, including the most technically challenging neutron spin misalignment, and found that it was a factor of 2 worse than if ideal experiments had been performed. This result gives the upper limit w/v of 10^{-4}, comparable to nEDM, after approximately 1400 hours of measurement, and provides a strong limit on BSM physics. Also, access to w/v was firstly achieved with the neutron transmission experiment, and the result of the current upper limit of 10^3 indicates that our future experiment will improve sensitivity on the order of 7. The implementation of this experiment is desired to involve research efforts that simultaneously fulfill the requirements of magnetic field control through a superconducting magnetic shield and the application of techniques for sufficiently cooling the target sample.

Acknowledgments

I extend my deepest gratitude to Professor Hirohiko M. Shimizu, my dissertation supervisor, for not only providing me with the opportunity to immerse myself in neutron physics research but also for the countless discussions and invaluable guidance that have led me to the successful submission of my dissertation. His unwavering support has been instrumental throughout this journey. The foundational experiments in this dissertation were made possible by the innovative ideas and support of Assistant Professor Takuya Okudaira. My sincere appreciation goes to him for his extensive support, encompassing advice on various discussions, revisions, analyses, and guidance on both the dissertation and the accompanying paper. I also wish to express my heartfelt thanks to Associate Professor Masaaki Kitaguchi for his effective guidance and foundational supervision, playing a pivotal role in the completion of this doctoral dissertation. Your valuable advice has been truly cherished. Gratitude is also extended to the collaborators from NOPTREX, whose critical advice and theoretical support during our meetings have significantly enriched the depth of my research. Thank you for your invaluable contributions. Special acknowledgment goes to Dr. Takenao Shinohara and Dr. Yusuke Tsuchikawa of the J-PARC RADEN scientists for their unwavering support, enabling the successful execution of essential experiments at the core of this dissertation. I would also like to express my appreciation to everyone in the J-PARC Neutron Beam Instrumentation technicians for their substantial contributions to the neutron beam operation and apparatus. This work was made possible through financial support from JST SPRING, Grant Number JPMJSP2125. I would also like to take this opportunity to express my gratitude to the "Interdisciplinary Frontier Next-Generation Researcher Program of the Tokai Higher Education and Research System".

References

[1] S. Endo *et al.*, Measurements of neutron total and capture cross sections of ^{139}La and evaluation of resonance parameters (2023). arXiv:2308.08802.
URL http://arxiv.org/abs/2308.08802

[2] H. Krüger, O. Lutz, H. Oehler, Nuclear magnetic moments and ratios of quadrupole moments 135Ba, 137Ba, 138La, 139La by NMR spectroscopy, Physics Letters A 62 (2) (1977) 131–132. doi:10.1016/0375-9601(77)90974-4.

[3] S. Mughabghab, Atlas of Neutron Resonances, sixth Edition, Vol. Volume:1, Elsevier, 2018. doi:10.1016/C2015-0-00522-6.
URL https://linkinghub.elsevier.com/retrieve/pii/C20150005226

[4] T. D. Lee, C. N. Yang, Question of Parity Conservation in Weak Interactions, Physical Review 106 (6) (1957) 1371–1371. doi:10.1103/PhysRev.106.1371.
URL https://link.aps.org/doi/10.1103/PhysRev.106.1371

[5] C. S. Wu *et al.*, Experimental Test of Parity Conservation in Beta Decay, Physical Review 105 (4) (1957) 1413–1415. doi:10.1103/PhysRev.105.1413.
URL https://link.aps.org/doi/10.1103/PhysRev.105.1413

[6] J. H. Christenson *et al.*, Evidence for the 2pi decay of the K02 meson, Physical Review Letters 13 (4) (1964) 138–140. doi:10.1103/PhysRevLett.13.138.
URL https://link.aps.org/doi/10.1103/PhysRevLett.13.138

[7] G. Aad *et al.*, Observation of a new particle in the search for the Standard Model Higgs boson with the ATLAS detector at the LHC, Physics Letters, Section B: Nuclear, Elementary Particle and High-Energy Physics 716 (1) (2012) 1–29. arXiv:1207.7214, doi:10.1016/j.physletb.2012.08.020.

[8] G. Hinshaw *et al.*, Nine-year wilkinson microwave anisotropy probe (WMAP) observations: Cosmological parameter results, Astrophysical Journal, Supplement Series 208 (2) (2013). arXiv:1212.5226, doi:10.1088/0067-0049/208/2/19.

[9] A. D. Sakharov, VIOLATION OF CP-INVARIANCE, C-ASYMMETRY, AND BARYON ASYMMETRY OF THE UNIVERSE, JETP Lett. (USSR)(Engl. Transl.), 5: 24-7(Jan. 1, 1967). (1967) 84–87doi:10.1142/9789812815941_0013.
URL http://www.worldscientific.com/doi/abs/10.1142/9789812815941{_}0013

[10] M. Kobayashi, T. Maskawa, CP -Violation in the Renormalizable Theory of Weak Interaction , Progress of Theoretical Physics 49 (2) (1973) 652–657. doi:10.1143/ptp.49.652.

[11] P. A. Zyla *et al.*, Review of particle physics, Progress of Theoretical and Experimental Physics 2020 (8) (2020) 1–2093. doi:10.1093/ptep/ptaa104.

[12] A. Belavin *et al.*, Pseudoparticle solutions of the Yang-Mills equations, Physics Letters B 59 (1) (1975) 85–87. doi:10.1016/0370-2693(75)90163-X.
URL http://link.springer.com/10.1007/BF01398073https://linkinghub.elsevier.com/retrieve/pii/037026937590163X

[13] C. G. Callan, R. F. Dashen, D. J. Gross, The structure of the gauge theory vacuum, Physics Letters B 63 (3) (1976) 334–340. doi:10.1016/0370-2693(76)90277-X.

[14] R. D. Peccei, H. R. Quinn, CP conservation in the presence of pseudoparticles, Physical Review Letters 38 (25) (1977) 1440–1443. doi:10.1103/PhysRevLett.38.1440.

[15] C. Abel *et al.*, Measurement of the Permanent Electric Dipole Moment of the Neutron, Physical Review Letters 124 (8) (2020) 81803. arXiv:2001.11966, doi:10.1103/PhysRevLett.124.081803.
URL https://doi.org/10.1103/PhysRevLett.124.081803

[16] T. S. Roussy *et al.*, An improved bound on the electron's electric dipole moment, Science (New York, N.Y.) 381 (6653) (2023) 46–50. doi:10.1126/science.adg4084.

[17] B. Graner *et al.*, Reduced Limit on the Permanent Electric Dipole Moment of Hg 199, Physical Review Letters 116 (16) (2016) 1–5. arXiv:1601.04339, doi:10.1103/PhysRevLett.116.161601.

[18] T. Chupp, M. Ramsey-Musolf, Electric dipole moments: A global analysis, Physical Review C - Nuclear Physics 91 (3) (2015) 1–11. arXiv:1407.1064, doi:10.1103/PhysRevC.91.035502.

[19] M. Pospelov, A. Ritz, Electric dipole moments as probes of new physics, Annals of Physics 318 (1 SPEC. ISS.) (2005) 119–169. arXiv:0504231, doi:10.1016/j.aop.2005.04.002.

[20] M. T. Gericke *et al.*, Measurement of parity-violating γ-ray asymmetry in the capture of polarized cold neutrons on protons, Physical Review C - Nuclear Physics 83 (1) (2011) 1–18. doi:10.1103/PhysRevC.83.015505.

[21] Y. H. Song, R. Lazauskas, V. Gudkov, Parity violation in low-energy neutron-deuteron scattering, Physical Review C - Nuclear Physics 83 (1) (2011) 1–10. doi:10.1103/PhysRevC.83.015501.

[22] Y. H. Song, R. Lazauskas, V. Gudkov, Time reversal invariance violating and parity conserving effects in neutron-deuteron scattering, Physical Review C - Nuclear Physics 84 (2) (2011) 1–6. doi:10.1103/PhysRevC.84.025501.

[23] J. D. Bowman, V. Gudkov, Search for time reversal invariance violation in neutron transmission, Physical Review C - Nuclear Physics 90 (6) (dec 2014). arXiv:1407.7004, doi:10.1103/PhysRevC.90.065503.

[24] B. Desplanques, J. F. Donoghue, B. R. Holstein, Unified treatment of the parity violating nuclear force, Annals of Physics 124 (2) (1980) 449–495. doi:10.1016/0003-4916(80)90217-1.

[25] I. S. Towner, A. C. Hayes, P,t-violating nuclear matrix elements in the one-meson exchange approximation, Phys. Rev. C 49 (1994) 2391–2397. doi:10.1103/PhysRevC.49.2391.
URL https://link.aps.org/doi/10.1103/PhysRevC.49.2391

[26] V. F. Dmitriev, I. B. Khriplovich, P and T odd nuclear moments, Physics Reports 391 (3-6) (2004) 243–260. doi:10.1016/j.physrep.2003.10.006.

[27] D. Blyth *et al.*, First Observation of P -odd γ Asymmetry in Polarized Neutron Capture on Hydrogen, Physical Review Letters 121 (24) (2018) 242002. arXiv:1807.10192, doi:10.1103/PhysRevLett.121.242002.
URL https://doi.org/10.1103/PhysRevLett.121.242002

[28] P. Fadeev, V. V. Flambaum, Time-reversal invariance violation in neutron-nucleus scattering, Physical Review C 100 (1) (jul 2019). arXiv:1903.08937, doi:10.1103/PhysRevC.100.015504.

[29] Y. H. Song, R. Lazauskas, V. Gudkov, Nuclear electric dipole moment of three-body systems, Physical Review C - Nuclear Physics 87 (1) (2013) 1–8. doi:10.1103/PhysRevC.87.015501.

[30] Y. Abov, P. Krupchitsky, Y. Oratovsky, On the existence of an internucleon potential not conserving spacial parity, Physics Letters 12 (1) (1964) 25–26. doi:10.1016/0031-9163(64)91162-X.
URL https://linkinghub.elsevier.com/retrieve/pii/003191636491162X

[31] S. P. Danilyan, G. V. ; Vodennikov, B. D. ; Dronyaev, V. P. ; Novitskiĭ, V. V. ; Pavlov, V. S. ; Borovlev, P-odd asymmetry in the fission of 239Pu by polarized thermal neutrons, ZhETF Pisma Redaktsiiu 26 (1977) 197.

[32] M. Forte *et al.*, First Measurement of Parity-Nonconserving Neutron-Spin Rotation: The Tin Isotopes, Physical Review Letters 45 (26) (1980) 2088–2092. doi:10.1103/PhysRevLett.45.2088.
URL https://link.aps.org/doi/10.1103/PhysRevLett.45.2088

[33] V. P. Alfimenkov *et al.*, Parity nonconservation in neutron resonances, Nuclear Physics, Section A 398 (1) (1983) 93–106. doi:10.1016/0375-9474(83)90649-8.

[34] F. Michel, Parity non-conservation in nuclei, Reports on Progress in Physics 43 (1) (1964) 67–123. doi:10.1088/0034-4885/43/1/002.

[35] L. Stodolsky, Neutron optics and weak currents, Physics Letters B 50 (3) (1974) 352–356. doi:10.1016/0370-2693(74)90688-1.

[36] L. Stodolsky, Neutron weak spin rotation: Exotic nuclear physics or a new weak force?, "Physics Letters, Section B: Nuclear, Elementary Particle and High-Energy Physics" 96 (1-2) (1980) 127–131. doi:10.1016/0370-2693(80)90227-0.

[37] V. F. OP Sushkov, Possibility of observing parity nonconservation in neutron optics, Jetp Letters 32 (1980) 352–354.

[38] V. Flambaum, O. Sushkov, Mechanism of parity violation in nuclear fission, Physics Letters B 94 (3) (1980) 277–279. doi:10.1016/0370-2693(80)90877-1.
URL https://linkinghub.elsevier.com/retrieve/pii/0370269380908771

[39] V. E. Bunakov, V. P. Gudkov, Parity non-conservation effects in neutron elastic scattering reactions, Zeitschrift für Physik A Atoms and Nuclei 303 (4) (1981) 285–291. doi:10.1007/BF01421525.

[40] V. E. Bunakov, V. P. Gudkov, Parity violation and related effects in neutron-induced reactions, Nuclear Physics, Section A 401 (1) (1983) 93–116. doi:10.1016/0375-9474(83)90338-X.

[41] J. M. Blatt, L. C. Biedenharn, The Angular Distribution of Scattering and Reaction Cross Sections, Reviews of Modern Physics 24 (4) (1952) 258–272. doi:10.1103/RevModPhys.24.258.
URL https://link.aps.org/doi/10.1103/RevModPhys.24.258

[42] C. Mahaux, H. A. Weidenmüller, A. Klein, Shell-Model Approach To Nuclear Reactions, Physics Today 24 (2) (1971) 46–47. doi:10.1063/1.3022571.
URL https://pubs.aip.org/physicstoday/article/24/2/46/427706/Shell-Model-Approach-To-Nuclear-Reactions

[43] G. Karl, D. Tadić, Model for scattering with parity violation, Physical Review C 16 (5) (1977) 1726–1734. doi:10.1103/PhysRevC.16.1726.
URL https://link.aps.org/doi/10.1103/PhysRevC.16.1726

[44] I. Baldin, AM and Gol'danskii, VI and Maksimenko, VM and Rozental, Kinematika yadernykh reaktsii, Atomizdat Moscow (1968).

[45] V. V. Flambaum, O. P. Sushkov, THEORY OF NEUTRON REACTIONS AND WEAK INTERACTION IN HEAVY NUCLEI, Tech. rep. (1984).

[46] D. Bohm, D. Pines, A Collective Description of Electron Interactions. I. Magnetic Interactions, Physical Review 82 (5) (1951) 625–634. doi:10.1103/PhysRev.82.625.
URL https://link.aps.org/doi/10.1103/PhysRev.82.625

[47] H. A. Bethe, Nuclear physics B. nuclear dynamics, theoretical, Reviews of Modern Physics 9 (2) (1937) 69–244. doi:10.1103/RevModPhys.9.69.

[48] V. V. Flambaum, O. P. Sushkov, Angular and polarization correlations in the (n, γ) reaction, Nuclear Physics, Section A 435 (2) (1985) 352–380. doi:10.1016/0375-9474(85)90469-5.

[49] P. K. Kabir, Test of T invariance in neutron optics, Physical Review D 25 (7) (1982) 2013–2014. doi:10.1103/PhysRevD.25.2013.

[50] L. Stodolsky, Parity violation in threshold neutron scattering, Nuclear Physics, Section B 197 (2) (1982) 213–227. doi:10.1016/0550-3213(82)90287-5.

[51] V. G. VE Bunakov, Enhancement ofT-noninvariant effects in neutron-induced nuclear reactions, Zeitschrift für Physik A Atoms and Nuclei 308 (4) (1985) 363–364.

[52] V. GUDKOV, SYMMETRY VIOLATION IN HEAVY NUCLEI, 2001, pp. 117–126. arXiv:0009016, doi:10.1142/9789812811189_0009.

[53] V. P. Gudkov, On the test of CP-violation models in neutron reactions, Physics Letters B 243 (4) (1990) 319–322. doi:10.1016/0370-2693(90)91390-W.

[54] V. P. Gudkov, On CP violation in nuclear reactions (1992). doi:10.1016/0370-1573(92)90121-F.

[55] G. E. Mitchell *et al.*, Parity violation in compound nuclei: Experimental methods and recent results, Physics Report 354 (3) (2001) 157–241. doi:10.1016/S0370-1573(01)00016-3.

[56] C.G.Windsor, PULSED NEUTRON SCATTERING, 1981.

[57] A. Abragam, M. Goldman, Principles of dynamic nuclear polarisation, Reports on Progress in Physics 41 (3) (1978) 395–467. doi:10.1088/0034-4885/41/3/002.

[58] P. Hautle, M. Iinuma, Dynamic nuclear polarization in crystals of Nd3+:LaAlO3, a polarized 139La target for a test of time-reversal invariance, Nuclear Instruments and Methods in Physics Research, Section A: Accelerators, Spectrometers, Detectors and Associated Equipment 440 (3) (2000) 638–642. doi:10.1016/S0168-9002(99)01054-2.

[59] F. Bitter, The optical detection of radiofrequency resonance, Physical Review 76 (6) (1949) 833–835. doi:10.1103/PhysRev.76.833.

[60] V. W. Yuan *et al.*, Parity nonconservation in polarized-neutron transmission through 139La, Physical Review C 44 (5) (1991) 2187–2194. doi:10.1103/PhysRevC.44.2187.
URL https://link.aps.org/doi/10.1103/PhysRevC.44.2187

[61] C. M. Frankle *et al.*, Parity nonconservation for the 0.88-eV neutron resonance in 81Br, Physical Review C 46 (4) (1992) 1542–1545. doi:10.1103/PhysRevC.46.1542.
URL https://link.aps.org/doi/10.1103/PhysRevC.46.1542

[62] D. A. Smith *et al.*, Parity violation in neutron resonances of 117Sn, Physical Review C - Nuclear Physics 64 (1) (2001) 155021–155029. doi:10.1103/PhysRevC.64.015502.

[63] J. J. Szymanski *et al.*, Observation of a large parity nonconserving analyzing power in Xe, Physical Review C - Nuclear Physics 53 (6) (1996) 2576–2580. doi:10.1103/PhysRevC.53.R2576.

[64] S. L. Stephenson *et al.*, Parity violation in neutron resonances in [Formula Presented], Physical Review C - Nuclear Physics 61 (4) (2000) 11. doi:10.1103/PhysRevC.61.045501.

[65] T. Okudaira *et al.*, Angular distribution of γ rays from neutron-induced compound states of la 140, Physical

Review C 97 (3) (mar 2018). doi:10.1103/PhysRevC.97.034622.
[66] T. Yamamoto *et al.*, Transverse asymmetry of γ rays from neutron-induced compound states of La 140, Physical Review C 101 (6) (jun 2020). doi:10.1103/PhysRevC.101.064624.
[67] M. Igashira, Y. Kiyanagi, M. Oshima, Nuclear data study at j-parc bl04, Nucl. Instrum. Meth. Phys. Res. A600 (2009) 332.
[68] T. Yamamoto *et al.*, Erratum: Transverse asymmetry of γ rays from neutron-induced compound states of 140La (Physical Review C (2020) 101 (064624) DOI: 10.1103/PhysRevC.101.064624), Physical Review C 105 (3) (2022) 1–2. doi:10.1103/PhysRevC.105.039901.
[69] V. Gudkov, H. M. Shimizu, Nuclear spin dependence of time reversal invariance violating effects in neutron scattering, Physical Review C 97 (6) (2018) 1–5. arXiv:1710.02193, doi:10.1103/PhysRevC.97.065502.
[70] V. Gudkov, H. M. Shimizu, Neutron spin dynamics in polarized targets, Physical Review C 102 (1) (2020) 15503. arXiv:1910.08598, doi:10.1103/PhysRevC.102.015503.
URL https://doi.org/10.1103/PhysRevC.102.015503
[71] D. A. Varshalovich, A. N. Moskalev, V. K. Khersonskii, Quantum Theory of Angular Momentum, Vol. 231, WORLD SCIENTIFIC, 1988. doi:10.1142/0270.
URL https://www.worldscientific.com/worldscibooks/10.1142/0270
[72] H. Paetz gen. Schieck, Nuclear Physics with Polarized Particles, Vol. 842 of Lecture Notes in Physics, Springer Berlin Heidelberg, Berlin, Heidelberg, 2012. doi:10.1007/978-3-642-24226-7.
URL https://link.springer.com/10.1007/978-3-642-24226-7
[73] V. P. Gudkov, THEORY OF T-VIOLATING P-CONSERVING EFFECTS IN NEUTRON-INDUCED REACTIONS, Tech. rep. (1991).
[74] A. Kurylov, G. C. McLaughlin, M. J. Ramsey-Musolf, Constraints on T-odd, P-even interactions from electric dipole moments, reexamined, Physical Review D 63 (7) (2001). doi:10.1103/PhysRevD.63.076007.
[75] V. E. Bunakov, V. P. Gudkov, POSSIBLE T-VIOLATION EXPERIMENTS IN NEUTRON INDUCED REACTIONS, Le Journal de Physique Colloques 45 (C3) (1984) C3–77–C3–80. doi:10.1051/jphyscol:1984315.
URL http://www.edpsciences.org/10.1051/jphyscol:1984315
[76] L. Stodolsky, Novel time-reversal tests in low-energy neutron propagation, Physics Letters B 172 (1) (1986) 5–9. doi:10.1016/0370-2693(86)90206-6.
[77] L. Stodolsky, Some Comments on Time Reversal and Novel T Tests in Neutron Propagation, Workshop on "Tests of Time Reversal Invariance in Neutron Physics" (June) (1987).
[78] P. K. Kabir, Polarization-asymmetry relations in neutron optics, Physical Review Letters 60 (8) (1988) 686–687. doi:10.1103/PhysRevLett.60.686.
[79] P. K. Kabir, Transformation of neutron polarization in polarized media and tests of T invariance, Physical Review D 37 (7) (1988) 1856–1859. doi:10.1103/PhysRevD.37.1856.
[80] P. K. Kabir, Symmetry tests in slow neutron interactions, Nuclear Inst. and Methods in Physics Research, A 284 (1) (1989) 63–65. doi:10.1016/0168-9002(89)90249-0.
[81] S. K. Lamoreaux, R. Golub, General analysis for experimental studies of time-reversal-violating effects in slow neutron propagation through polarized matter, Physical Review D 50 (9) (1994) 5632–5638. doi:10.1103/PhysRevD.50.5632.
[82] P. K. Kabir, G. Karl, E. Obryk, Optical activity for neutrons, Physical Review D 10 (5) (1974) 1471–1474. doi:10.1103/PhysRevD.10.1471.
URL https://link.aps.org/doi/10.1103/PhysRevD.10.1471
[83] V. F. Sears, Fundamental aspects of neutron optics (1982). doi:10.1016/0370-1573(82)90151-X.
[84] M. I. Baryshevskii, V G and Podgoretskii, NUCLEAR PRECESSION OF NEUTRONS, Zh. Eksperim. i Teor. Fiz. Vol.47 (1964) 5.
[85] A. Abragam *et al.*, Pseudo Magnetic Moments of 1H and 51V Measured by a new Method, Physical Review Letters 31 (12) (1973) 776–779. doi:10.1103/PhysRevLett.31.776.
URL https://link.aps.org/doi/10.1103/PhysRevLett.31.776
[86] V. G. Baryshevsky, High-Energy Nuclear Optics of Polarized Particles, WORLD SCIENTIFIC, 2012. doi:10.1142/7947.
URL www.worldscientific.comhttps://www.worldscientific.com/worldscibooks/10.1142/7947
[87] J-PARC MLF webcite.
URL https://mlfinfo.jp/ja/blmap.html

[88] K. Oikawa *et al.*, Custom-Made Shutter Block for Imaging Instrument "RADEN" at J-PARC, in: Proceedings of the 2nd International Symposium on Science at J-PARC — Unlocking the Mysteries of Life, Matter and the Universe —, Journal of the Physical Society of Japan, 2015. doi:10.7566/JPSCP.8.036002.
URL http://journals.jps.jp/doi/10.7566/JPSCP.8.036002

[89] T. Shinohara *et al.*, The energy-resolved neutron imaging system, RADEN, Review of Scientific Instruments 91 (4) (apr 2020). doi:10.1063/1.5136034.
URL https://pubs.aip.org/rsi/article/91/4/043302/1030764/The-energy-resolved-neutron-imaging-system-RADEN

[90] V. F. Sears, Neutron scattering lengths and cross sections, Neutron News 3 (3) (1992) 26–37. doi:10.1080/10448639208218770.

[91] M. A. Bouchiat, T. R. Carver, C. M. Varnum, Nuclear polarization in He3 gas induced by optical pumping and dipolar exchange, Physical Review Letters 5 (8) (1960) 373–375. doi:10.1103/PhysRevLett.5.373.

[92] T. Okudaira *et al.*, Development and application of a 3He Neutron Spin Filter at J-PARC, Nuclear Instruments and Methods in Physics Research, Section A: Accelerators, Spectrometers, Detectors and Associated Equipment 977 (June) (2020) 164301. doi:10.1016/j.nima.2020.164301.
URL https://doi.org/10.1016/j.nima.2020.164301

[93] E. Babcock *et al.*, Hybrid spin-exchange optical pumping of [formula presented], Physical Review Letters 91 (12) (2003) 1–4. doi:10.1103/PhysRevLett.91.123003.

[94] T. Ino *et al.*, A compact SEOP 3He neutron spin filter with AFP NMR, Journal of Physics: Conference Series 340 (2012). doi:10.1088/1742-6596/340/1/012006.

[95] N. R. Newbury *et al.*, Gaseous 3He- 3He magnetic dipolar spin relaxation, Physical Review A 48 (6) (1993) 4411–4420. doi:10.1103/PhysRevA.48.4411.
URL https://link.aps.org/doi/10.1103/PhysRevA.48.4411

[96] E. Lelièvre-Berna, Mid-term report of the NMI3 neutron spin filter project, Physica B: Condensed Matter 397 (1-2) (2007) 162–167. doi:10.1016/j.physb.2007.02.089.

[97] V. I. Luschikov, Y. V. Taran, On the calculation of the neutron adiabatic spin-flipper, Nuclear Inst. and Methods in Physics Research, A 228 (1) (1984) 159–160. doi:10.1016/0168-9002(84)90025-1.

[98] S. Satoh, Development of a 2012 model for the 6Li time analyzer detector system, Physics Procedia 60 (C) (2014) 363–368. doi:10.1016/j.phpro.2014.11.049.
URL http://dx.doi.org/10.1016/j.phpro.2014.11.049

[99] R. B. Wiringa, V. G. J. Stoks, R. Schiavilla, Accurate nucleon-nucleon potential with charge-independence breaking, Phys. Rev. C 51 (1995) 38–51. doi:10.1103/PhysRevC.51.38.
URL https://link.aps.org/doi/10.1103/PhysRevC.51.38

[100] J. Carlson, V. Pandharipande, R. Wiringa, Three-nucleon interaction in 3-, 4- and -body systems, Nuclear Physics A 401 (1) (1983) 59–85. doi:https://doi.org/10.1016/0375-9474(83)90336-6.
URL https://www.sciencedirect.com/science/article/pii/0375947483903366

[101] T. O. Niinikoski, F. Udo, "Frozen spin" polarized target, Nuclear Instruments and Methods 134 (2) (1976) 219–233. doi:10.1016/0029-554X(76)90274-3.

[102] S. Ishimoto *et al.*, A spin-frozen polarized target of proton and deuteron, Japanese Journal of Applied Physics 28 (10 R) (1989) 1963–1972. doi:10.1143/JJAP.28.1963.

[103] J. Chen *et al.*, Interfacial thermal resistance: Past, present, and future, Reviews of Modern Physics 94 (1) (2022) 25002. doi:10.1103/RevModPhys.94.025002.
URL https://doi.org/10.1103/RevModPhys.94.025002

[104] T. Yamamoto, Experimental study of discrete symmetry in a compound nucleus, Ph.D. thesis (2021).